PhotoniX Life

Open Access
PhotoniX Life (2026)1:2
https://doi.org/10.3724/PXLIFE.2025-0009

Review

Deep-tissue optics: Multidisciplinary innovations and emerging frontiers—A comprehensive review

Weiran Pang[1#], Tianting Zhong[1#], Yize Gao[2#], Xiazi Huang[1,3#], Wu Yuan[4], Di Mei[4], Xingde Li[5], Kenneth K. Y. Wong[6,7], Xin Dong[6], Qiuqiang Zhan[8], Rui Pu[8], Zhenhua Hu[9], Daifa Wang[10], Di Wu[10], Changhui Li[11], Liulin He[12], Qinrong Zhang[12], Yuecheng Shen[13], Shian Zhang[13], Jiamiao Yang[14], Chunxu Ding[14], Lei Gong[15], Jinghan Zhuang[15], Qing Yang[16], Quanzhi Li[16], Liangcai Cao[17], Jiachen Wu[17], Pengcheng Li[18], Jiachi Hong[18], Tingting Yu[19], Chao Zuo[20], Haigang Ma[20], Yingying Zhou[1,21], Honglin Liu[22], Xuyu Zhang[23], Dan Zhu[19*], Valery V. Tuchin[24*], Jie Tian[9*], Cheng Ma[2*] AND Puxiang Lai[1,25*]

[1]*Department of Biomedical Engineering, the Hong Kong Polytechnic University, Hong Kong 999077, China;*
[2]*Beijing National Research Center for Information Science and Technology, Department of Electronic Engineering, Tsinghua University, Beijing 100084, China;*
[3]*Medical Engineering and Engineering Medicine Innovation Center, Hangzhou International Innovation Institute, Beihang University, Hangzhou 311115, China;*
[4]*Department of Biomedical Engineering, Chinese University of Hong Kong, Hong Kong 999077, China;*
[5]*Department of Biomedical Engineering, Johns Hopkins University, Baltimore 21211, USA;*
[6]*Department of Electrical and Electronic Engineering, the University of Hong Kong, Hong Kong 999077, China;*
[7]*Advanced Biomedical Instrumentation Centre, Hong Kong Science Park, Hong Kong 999077, China;*
[8]*Centre for Optical and Electromagnetic Research, Guangdong Engineering Research Centre of Optoelectronic Intelligent Information Perception, South China Academy of Advanced Optoelectronics, South China Normal University, Guangzhou 510006, China;*
[9]*CAS Key Laboratory of Molecular Imaging, Beijing Key Laboratory of Molecular Imaging, Institute of Automation, Chinese Academy of Sciences, Beijing 100190, China;*
[10]*Key Laboratory for Biomechanics and Mechanobiology of Ministry of Education, School of Biological Science and Medical Engineering, Beihang University, Beijing 100086, China;*
[11]*National Biomedical Imaging Center, Peking University, Beijing 100871, China;*
[12]*Department of Biomedical Engineering, City University of Hong Kong, Hong Kong 999077, China;*
[13]*State Key Laboratory of Precision Spectroscopy, East China Normal University, Shanghai 200241, China;*
[14]*School of Electronic Information and Electrical Engineering, Shanghai Jiao Tong University, Shanghai 200240, China;*
[15]*Department of Optics and Optical Engineering, University of Science and Technology of China, Hefei 230026, China;*
[16]*College of Optical Science and Engineering, Zhejiang University, Hangzhou 310027, China;*
[17]*Department of Precision Instruments, Tsinghua University, Beijing 100084, China;*
[18]*School of Biomedical Engineering, Hainan University, Haikou 570228, China;*
[19]*Wuhan National Laboratory for Optoelectronics, Huazhong University of Science and Technology, Wuhan 430074, China;*
[20]*Smart Computational Imaging Laboratory (SCILab), School of Electronic and Optical Engineering, Nanjing University of Science and Technology, Nanjing 210094, China;*
[21]*College of Professional and Continuing Education, the Hong Kong Polytechnic University, Hong Kong 999077, China;*
[22]*Key Laboratory for Quantum Optics, Shanghai Institute of Optics and Fine Mechanics, Chinese Academy of Sciences, Shanghai 201800, China;*
[23]*Aerospace Laser Technology and System Department, Shanghai Institute of Optics and Fine Mechanics, Chinese Academy of Sciences, Shanghai 201800, China;*
[24]*Institute of Physics and Science Medical Center, Saratov State University, Saratov 410012, Russian;*
[25]*Shenzhen Research Institute, the Hong Kong Polytechnic University, Shenzhen 518057, China*
** Corresponding authors (emails: dawnzh@mail.hust.edu.cn (D.Z.); tuchinvv@mail.ru (V.V.T.); tian@ieee.org (J.T.); cheng_ma@tsinghua.edu.cn (C.M.); puxiang.lai@polyu.edu.hk (P.L.))*
 # These authors contributed equally to this work

Received 14 May 2025; accepted 13 November 2025; published online 31 March 2026

Abstract Optical imaging has revolutionized biomedical research and clinical diagnostics by enabling non-invasive visualization of biological structures and dynamic processes. However, its utility in deep-tissue applications remains constrained by photon scattering, absorption, and refractive index heterogeneity. This comprehensive review systematically examines multidisciplinary innovations across physical, chemical, and computational domains to overcome these barriers. Physically, coherence-gated techniques (e.g., optical coherence tomography, multiphoton microscopy) and diffuse light

© The Author(s) 2026. This is an Open Access article distributed under the CC BY-NC-ND license (https://creativecommons.org/licenses/by-nc-nd/4.0/).

methodologies (e.g., near-infrared-II fluorescence, photoacoustic imaging) enhance resolution and depth. Chemically, tissue optical clearing agents and advanced contrast agents improve optical accessibility and specificity. Computationally, adaptive optics and artificial intelligence (AI) paradigms correct distortions and enable real-time image reconstruction. We highlight transformative clinical applications in neuroscience, oncology, and surgery, such as neural activity mapping, tumor margin delineation, and intraoperative guidance. Critical challenges—including phototoxicity, nanoparticle biocompatibility, and clinical standardization—are addressed, underscoring the need for scalable protocols and translational frameworks. Emerging trends, such as AI-driven theranostics, minimally invasive fiber-based probes, and multimodal systems, are poised to redefine precision medicine. By synthesizing state-of-the-art technologies and envisioning future innovations, this review emphasizes the convergence of optics, materials science, and computational biology to unlock new frontiers in deep-tissue imaging and therapeutic interventions.

Keywords deep-tissue optics, biomedical imaging, deep penetration, wavefront engineering, tissue clearing, artificial intelligence (AI)

1. Introduction

Light has long been a cornerstone of biomedical research and clinical practice, offering unparalleled capabilities for imaging, sensing, and therapeutic applications [1-4]. From fluorescence microscopy to laser surgery, the interaction of light with biological tissues has enabled groundbreaking advancements in understanding cellular processes, diagnosing diseases, and guiding treatments. Light-based technologies have revolutionized the biomedical field by offering a unique combination of safety, versatility, and high sensitivity. Unlike conventional clinical imaging modalities such as X-ray, computed tomography (CT), and positron emission tomography (PET), which rely on ionizing radiation with potential carcinogenic risks, optical imaging operates within biologically safe thresholds, enabling repeated and long-term monitoring without cumulative harm [3]. Furthermore, the inherent properties of light, including wavelength, phase, amplitude, and polarization, provide rich multidimensional information for biomedical investigations. For instance, multispectral imaging leverages wavelength-dependent absorption to map tissue oxygenation in real time, while polarization-sensitive techniques exploit light-tissue interactions to detect structural anisotropy in collagen or neural fibers. The exceptional sensitivity of optical systems allows detection of biomolecules at nanomolar concentrations, further enhanced by advanced contrast agents such as fluorescent dyes and targeted nanoparticles. These agents not only improve imaging contrast but also enable molecular-level specificity, as exemplified by tumor-targeted probes for early cancer diagnosis.

However, the utility of light in biomedicine is often constrained by the strong scattering and absorption of photons in biological tissues, particularly when targeting deep structures [5]. These limitations have spurred the development of deep-tissue optics, a field dedicated to extending the reach of light into deeper anatomical regions while preserving resolution and sensitivity. The topic is of paramount importance for both fundamental research and clinical applications. For example, in neuroscience, the ability to visualize and manipulate neural activity in deep brain regions is critical for understanding brain function and treating neurological disorders [6,7]. Similarly, in oncology, imaging deep-seated tumors with high precision can significantly improve early diagnosis and treatment monitoring [8].

Despite its potential, the field encounters a fundamental trade-off: achieving high spatial resolution typically requires short-wavelength light, which is heavily scattered and absorbed, whereas longer wavelengths penetrate deeper but offer lower resolution. This inherent conflict has driven the development of innovative optical technologies aimed at balancing these competing demands.

The central challenge lies in balancing the inherent trade-off between resolution and penetration depth. Short-wavelength light provides high resolution but suffers from rapid attenuation, while longer wavelengths (e.g., near-infrared (NIR)-II) penetrate deeper at the cost of reduced spatial detail. Over the past decade, multidisciplinary innovations have emerged to resolve this dilemma, integrating physical optics, computational modeling, machine learning, and biocompatible materials engineering. This review systematically explores these physical, computational, and chemical-strategies. On the physical front, we dissect methodologies that either exploit ballistic light (e.g., coherence/time gating, NIR, multiphoton nonlinear, and up-conversion imaging) or harness diffuse light (e.g., photoacoustic imaging (PAI)), leveraging light-tissue interactions, computational reconstruction, and hardware innovations to simultaneously enhance resolution and penetration depth. On the computational front, adaptive optics (AO), wavefrontengineering, transmission matrix (TM), and other relevant efforts are discussed for their applications in deep tissue. Complementing these, chemical strategies such as tissue clearing —via hemoglobin removal and refractive index (RI) matching— enhance optical accessibility by minimizing scattering and absorption, resolving limitations at their origin. Materials strategies, including targeted optical enhancers and molecular environment-sensitive dyes, have been summarized to provide enhanced signals with tunable optical properties and biocompatibility.

Clinically, these advancements have enabled breakthroughs in dynamic cellular tracking, intraoperative tumor visualization, and non-invasive brain imaging. Yet challenges persist, including phototoxicity, biocompatibility of nanomaterials, and the translation of artificial intelligence (AI) models to diverse clinical settings. Emerging frontiers—such as minimally invasive fiber-based endoscopy, multimodal systems, and AI-enhanced theranostics—promise to bridge these gaps, offering scalable solutions for precision medicine. This review not only synthesizes state-of-the-art technologies but also provides a roadmap for future innovations, emphasizing the synergy between disciplines to advance both fundamental discovery and clinical translation.

2. Fundamental principles of light-tissue interactions

2.1 Photon propagation mechanisms in biological tissue

Light propagation in biological tissues is governed by complex interactions between photons and tissue components, primarily characterized by scattering and absorption. Scattering arises from elastic collisions between photons and subcellular structures (e.g.,

membranes, organelles) and extracellular matrices (e.g., collagen fibers). Quantified by the scattering coefficient (μ_s) and anisotropy factor (g), this process randomizes photon trajectories, forming a diffuse light field in highly scattering tissues like the brain or skin. Absorption occurs when photons transfer energy to endogenous chromophores such as hemoglobin (visible range), melanin (ultraviolet (UV)-visible), and water (NIR >1,300 nm). The absorption coefficient (μ_a) determines the exponential attenuation of light intensity with depth. In addition, heterogeneous RI between different tissue components, e.g., lipid-rich membranes (RI ≈ 1.46) vs. aqueous cytoplasm (RI ≈ 1.35), induces interfacial scattering. This mismatch distorts wavefronts and reduces effective photon penetration, particularly in dense tissues like muscle or tumors.

These interactions collectively define the attenuation length (L), a critical parameter for penetration depth: $L = 1/(1/L_s+1/L_a) = 1/(\mu_s+\mu_a)$, where $L_s = 1/\mu_s$ is the scattering length, and $L_a = 1/\mu_a$ is the absorption length.

2.2 Ballistic vs. diffuse photon regimes

The propagation of light in tissues can be categorized into two regimes based on photon trajectories: ballistic photons represent a minuscule fraction (~10^{-6} at 1 mm depth) of the incident photons that travel unscattered, retaining spatiotemporal coherence [9]. These photons enable high-resolution techniques like optical coherence tomography (OCT) and multiphoton microscopy (MPM). However, ballistic photon flux decreases exponentially with depth, limiting their utility beyond 1–2 mm. The other is diffuse photons, for which the majority undergo multiple scattering events, forming a random walk pattern. While these photons penetrate deeper and carry information about deep tissue structures, their scrambled phase and directionality necessitate computational reconstruction (e.g., diffuse optical tomography) or hybrid modalities (e.g., PAI) to extract meaningful signals.

2.3 Critical parameters for imaging performance

The interplay of scattering, absorption, and RI heterogeneity imposes inherent trade-offs as exemplified: resolution-penetration dilemma, short wavelengths (e.g., 500 nm) provide high resolution but suffer from strong scattering/absorption, while long wavelengths (e.g., NIR-II from 900–1,300 nm) penetrate deeper but reduce spatial resolution; signal-to-background ratio (SBR), scattering-induced background noise necessitates strategies like time gating (OCT), nonlinear excitation (MPM), or molecular probes to enhance the contrast; transport mean free path $L^* = L_s/(1-g)$, defining the depth at which light transitions from ballistic to diffusive propagation ~1 mm in mouse brain. Beyond L^*, wavefront correction (e.g., AO) becomes essential for resolving fine structures.

3. Versatile physical modalities

3.1 Ballistic light-based techniques

3.1.1 Coherence-gated imaging: optical coherence tomography

OCT, first introduced in 1991 [10], is a non-invasive imaging technique that exploits the coherence properties of light to achieve high-resolution, depth-resolved imaging of biological tissues at the micron scale. Operating on interferometric principles, OCT splits broadband NIR light into reference and sample arms (Figure 1a). The interference pattern of backscattered light from the sample and reference mirror is analyzed to reconstruct cross-sectional images with axial resolutions of 1–15 μm, depending on the source bandwidth. OCT systems are broadly classified into time-domain OCT (TD-OCT) and Fourier-domain OCT (FD-OCT) configurations [11]. TD-OCT, the earliest form, measures the time delay of light reflections to construct an image, but it is slow due to sequential depth scans. FD-OCT comprises two main modalities: spectral-domain OCT (SD-OCT) and swept-source OCT (SS-OCT), both of which provide superior imaging speed and resolution compared to earlier technologies. In SD-OCT, a spectrometer captures the full spectrum of light reflected from biological tissues, facilitating rapid scanning and high-resolution image acquisition. In contrast, SS-OCT utilizes a wavelength-tunable laser operating in the NIR domain that sweeps across a range of wavelengths, enabling even faster imaging and enhanced tissue penetration, particularly in deeper structures. Additionally, optical coherence tomography angiography (OCTA), derived from FD-OCT, visualizes blood vessels, enhancing OCT's clinical utility [12].

Recent advancements in OCT focus on optimizing spatial resolution, penetration depth, temporal resolution, and clinical utility. High-resolution OCT systems usually employ light sources around 800 nm to balance resolution and depth [13]. While shorter wavelengths improve axial and transverse resolution, achieving cellular-level resolution at longer wavelengths (1,000–1,300 nm) is more challenging. To achieve higher resolution, ultrahigh-resolution OCT using visible light or ultra-broadband sources (Figure 1b), like femtosecond lasers and supercontinuum sources, has achieved axial resolutions between 1 and 3 μm, though at the expense of tissue penetration depth [14]. Regarding imaging depth, OCT's effective penetration is limited to about 1–3 mm due to scattering and absorption by biological tissues [13]. To examine deeper organs, miniaturized OCT catheters and endoscopes with sub-millimeter diameters have been developed. These devices incorporate flexible optical fibers for biocompatible and often disposable probes that enable imaging of internal organs (Figure 1d) [15]. Furthermore, advanced soft robotic mechanisms enhance the probes' ability to navigate complex anatomical structures, allowing deeper and more detailed intrabody imaging (Figure 1e) [16]. On the temporal resolution front, OCT has benefited from advancements in imaging speed. Commercial systems achieve A-line rates of several hundred kHz, and ultrahigh-speed SD-OCT systems have reached A-scan rates of up to 1 MHz (Figure 1f) [17]. In SS-OCT, A-line rates of up to 9.4 MHz have been achieved using customized 1,300 nm lasers [18].

OCT has been recognized as the gold standard in ophthalmology. It provides high-resolution, 3D imaging of the retina and optic nerve, enabling diagnosis and monitoring of major eye diseases like age-related macular degeneration, diabetic retinopathy, and glaucoma [19,20]. It also assists in detecting fluid accumulation, guiding surgeries, and aiding in cataract surgery planning. OCTA, which visualizes blood vessels, enhances the

assessment of conditions such as neovascularization and ischemia [21-23]. In dermatology, OCT has been used for the diagnosis and treatment monitoring of skin cancers, particularly malignant melanoma. It helps identify sub-anatomical structures of the skin, including tumor characteristics like cell aggregation, atypical clusters, and irregular vascular systems. It is also valuable for detecting basal cell carcinoma, providing high sensitivity and specificity for distinguishing between subtypes. Furthermore, polarization-sensitive OCT has been used for detecting skin fibrosis, such as in systemic sclerosis, enabling quantitative collagen measurements and assisting in disease monitoring [24,25]. OCT combined with endoscopy has become a key tool for *in-vivo* imaging, especially for superficial tissues. Endoscopic OCT can deliver light into the body, capturing reflected light to create cross-sectional images that are crucial for real-time diagnosis [26]. It has been used in detecting conditions like Barrett's esophagus, a precursor to esophageal cancer, where it helps assess tissue changes and aids in early cancer diagnosis [27-29]. OCT has also been employed in bronchoscopic imaging for lung disease detection, offering detailed images of airway walls [30,31]. In primary sclerosing cholangitis, combining OCT with endoscopic retrograde cholangiopancreatography helps differentiate benign strictures from malignant tumors, providing insights into bile duct morphology and aiding in diagnosis [32,33].

(1) Challenges

Despite these advances, OCT suffers from limited tissue penetration and resolution degradation with increased depth. The scattering and absorption of light by biological tissues, especially by molecules like hemoglobin, pigments, and water, restrict its effective penetration to about 1–2 mm in tissues like the retina [11]. Deeper structures, such as those in the brain or organs, remain difficult to image with high resolution. This limitation is especially apparent in tissues with high scattering properties like skin or muscle, where signal attenuation reduces the achievable imaging depth and resolution.

To address these challenges, several strategies are being explored to enhance OCT's clinical potential. One key approach is optimizing the OCT system's central wavelength. Different wavelengths interact differently with tissues: wavelengths around 830 nm provide a balance of low absorption and high scattering, while 1,050 nm allows for deeper penetration. Wavelengths around 1,310 nm help reduce scattering, improving imaging depth [12]. Other techniques, like modulating light scattering using spatial light modulators (SLMs) and applying multiple scattering low-coherence interferometry (MS/LCI), have extended the imaging depth (Figure 1c) [34]. Dynamic focusing methods via liquid-filled polymer lenses or gradient-index (GRIN) lenses can improve depth and lateral resolution. Beam shaping techniques, such as creating Bessel or needle beams with multiple foci, help extend the depth of focus while maintaining horizontal resolution (Figure 1g) [35].

(2) Future directions

As OCT technology evolves, particularly with advancements in depth, resolution, and speed, it is expected to expand its applications beyond traditional fields. The integration of AI and machine learning with OCT systems will improve early detection, precision diagnosis, and personalized treatment, particularly in complex and systemic diseases. In the short to medium term, OCT will continue to lead in ophthalmology and dermatology, while its applications in cardiovascular, neurovascular, and other systemic diseases will increase. OCT is likely to become an essential tool for real-time diagnostics and surgical navigation,

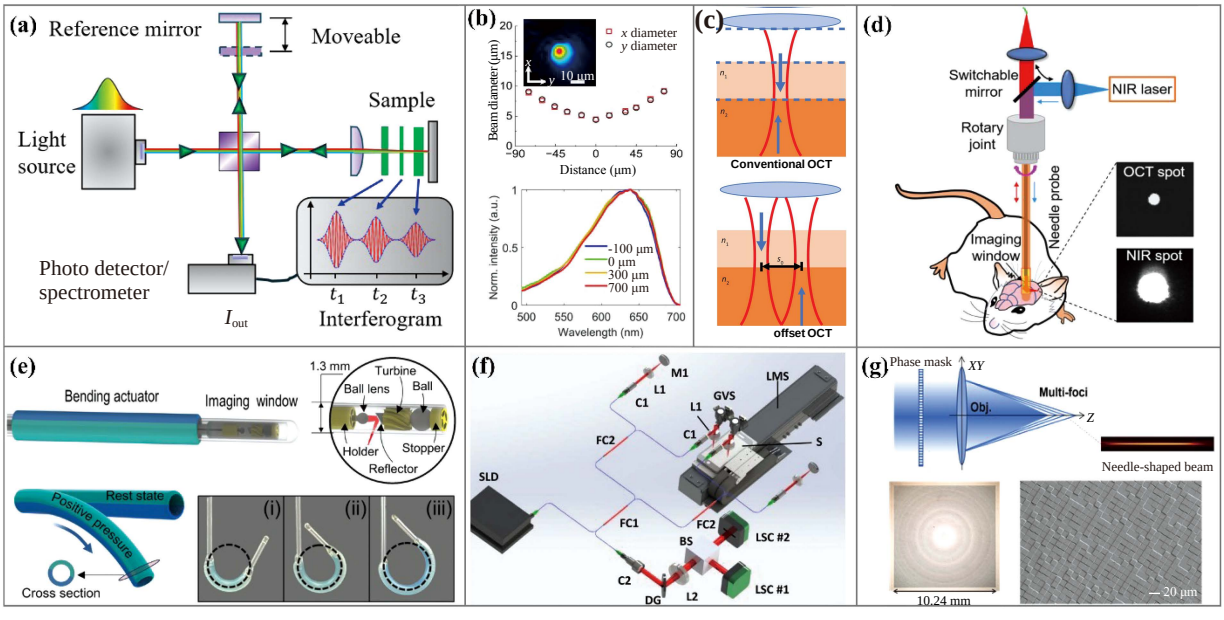


Figure 1 Principle and recent advances in OCT: resolution, depth, miniaturization, and speed. **a.** Working principles for OCT with broadband light sources; **b.** high-resolution OCT via visible light, where beam diameters are measured in the horizontal directions (top) with the back-reflected light spectra (bottom) [14]; **c.** depth-enhanced OCT leveraging the multiple-scatter photons [34]; **d.** deep-brain imaging with a theranostic OCT microneedle for fast ultrahigh-resolution [15]; **e.** pneumatic OCT endoscope that allows for bending and navigation through narrow turns [16]; **f.** ultrahigh-speed SD-OCT system operating at 1 MHz A-line rates using multiple cameras within a single spectrometer [17]; **g.** extended depth of focus in OCT via multiplexed phase patterns generating needle-shaped beams [35].

making a significant impact on a wide range of medical specialties. Over the long term, OCT's potential in heart and brain disease diagnostics will solidify its place as a transformative technology in medical imaging.

3.1.2 Multiphoton excitation microscopy

MPM is one of the most powerful tools for achieving deep biological imaging *in vivo* using ultrashort NIR lasers, with minimal photobleaching and phototoxicity. There are two methods to realize MPM [36], as illustrated in Figure 2a. One method is based on optical harmonic generation, such as second-harmonic generation (SHG) and third-harmonic generation (THG), which provide structural information of cells and tissues without the need for labeling processes. The other method relies on nonlinear multi-photon absorption to excite fluorescence signals, typically achieved through two-photon fluorescence (2PF) using a 1,000 nm ultrashort laser pulse and three-photon fluorescence (3PF) using 1,300 nm or 1,700 nm ultrashort laser pulses. Unlike traditional single-photon fluorescence (1PF), MPM utilizes nonlinear excitation that occurs only at the focal volume where photon density is sufficient for simultaneous absorption, resulting in a confined excitation range and improved resolution, depth, and contrast while minimizing out-of-focus photobleaching. Owing to the flexibility in sample structures for fluorescence imaging, which is not limited to fluorescence proteins like green fluorescent protein (GFP) and yellow fluorescent protein (YFP), 2PF and 3PF methods find extensive applications, particularly in neuroscience.

Recent technological advancements in MPM have primarily focused on enhancing penetration depth and imaging speed, which are typically constrained by the attenuation and scattering within biological tissue and scanning patterns, respectively. A representative 3D imaging outcome is depicted in Figure 2b [37]. By utilizing longer excitation wavelengths that avoid the water absorption peak, a penetration depth of 1.4 mm can be achieved with 3PF using a 1,300 nm laser [38]. Furthermore, the implementation of AO for aberration correction enables optimization of the focal point within the biomedical tissue, leading to further enhancement of the penetration depth.

Enhanced imaging speed is crucial for capturing rapid biomedical dynamics such as cell migration, intracellular signaling events, and neuronal activity. In conventional MPM, a Gaussian beam is typically used, requiring a 3D scan that involves an *x*-*y* scan using galvo mirrors and an axial scan using a motor. However, due to mechanical inertia, this 3D scan process is time-consuming. By employing free-space angular-chirp-enhanced delay (FACED) cavities [39] or spectral separation with diffraction gratings [40], the frame rate of the *x*-*y* scan can be increased to kHz. Improvements in axial scanning speed can be achieved through methods such as beam multiplexing [41], acousto-optic lens implementation [42], or converting lateral scanning to axial scanning [43]. The use of diffraction-free beams like Bessel beams (BBs) and Airy beams (ABs), which have extended beam profiles in depth, allows for obtaining a projected view of the 3D volume without the need for axial scanning, enabling high-throughput volumetric imaging. Bessel droplet beams, created by the interference of two BBs with different axial frequencies as shown in Figure 2d, exhibit periodic energy distribution and can enhance imaging speed with improved axial resolution [44]. Additionally, by minimizing the side lobes in Bessel droplet beams, imaging contrast can be enhanced through the use of alternating Bessel droplet beams [45].

MPM also provides high resolution for observing subcellular structures within cells, enabling detailed capture of biomedical

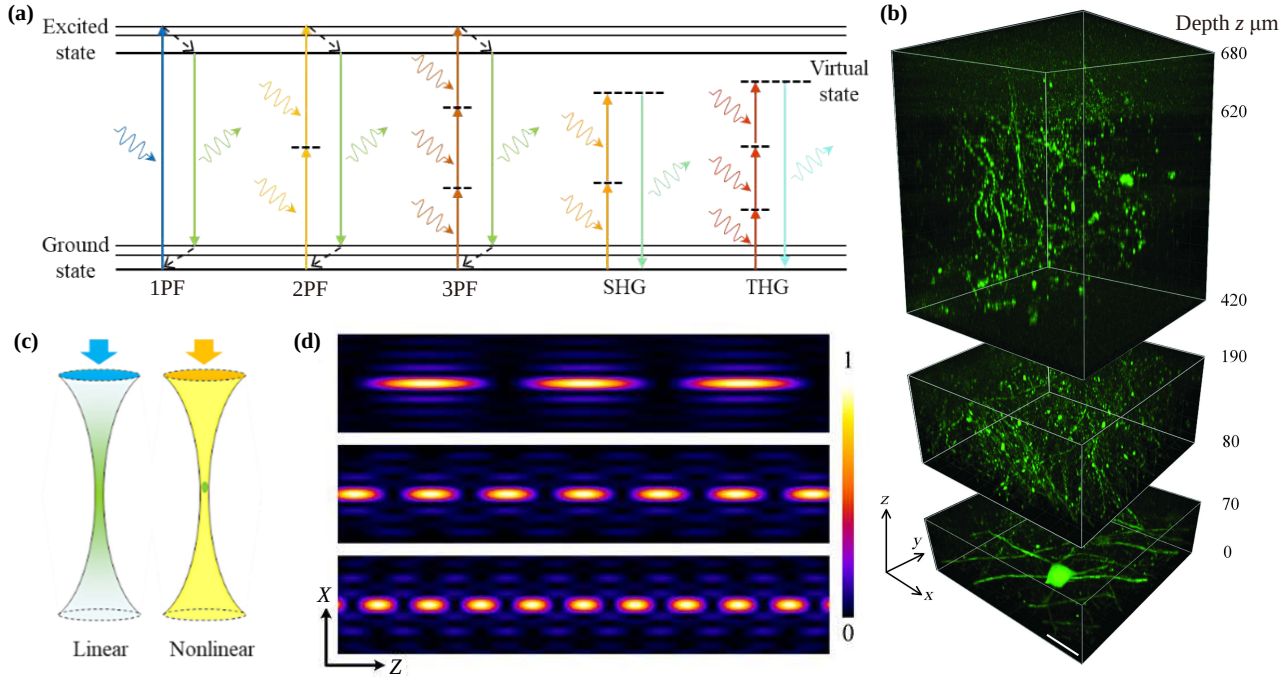


Figure 2 MPM principle and typical results. **a.** Energy diagrams comparing 1PF, 2PF, SHG, 3PF, and THG [36]; **b.** typical 2PF imaging of neurons in the mouse brain [37]; **c.** spatial confinement of signal generation with nonlinear excitation; **d.** bessel droplet beams with different beating frequencies [44].

activities. Thanks to nonlinear excitation, the diffraction limit is relaxed, leading to enhanced resolution, as depicted in Figure 2c. Further improvements in resolution can be achieved through super-resolution techniques like stimulated emission depletion (STED) microscopy [46] and structured illumination microscopy (SIM) [47], which offer enhanced resolution at the nanoscale level. Except for enhanced lateral properties, it is essential to consider the axial dimension in 3D imaging systems. As mentioned above, BBs have demonstrated significant capabilities in the axial resolution improvement, and the further development of advanced forms of BBs, such as droplet beams, will continue to be instrumental in exploring the uncharted axial regime.

Over the past decade, miniaturized MPMs have transformed *in-vivo* imaging by bringing high-resolution, deep-tissue fluorescence microscopy into freely behaving animals. Traditional bench-top MPMs provide sub-micrometer resolution and optical sectioning but are limited to head-fixed preparations. To overcome these constraints, researchers have developed lightweight, head-mounted devices—often <3 g—that integrate compact femtosecond lasers, fiber-optic beam delivery, and miniature scanning mechanisms. Key engineering advances include: fiber-based excitation: hollow-core photonic crystal fibers and dispersion-compensated designs now permit stable femtosecond pulse delivery over flexible tethers; miniaturized scanners: resonant MEMS mirrors and tunable lenses enable fast *x-y* scanning and dynamic focusing in volumes up to several hundred micrometers; integrated detection: GRIN relay lenses and on-board photodetectors maintain high numerical aperture (NA) while keeping weight minimal. These improvements have enabled real-time multi-photon calcium imaging of cortical and subcortical circuits in freely moving mice [48,49]. Applications now span sensory processing, social behaviors, and longitudinal monitoring of disease models [50,51]. Miniaturized MPMs thus represent a critical bridge between cellular-resolution optical imaging and naturalistic behavioral neuroscience.

(1) Challenges

A critical challenge in MPM lies in managing the photon budget: high laser power risks photodamage, while insufficient power compromises signal-to-noise ratio (SNR). In MPM, samples are often susceptible to laser-induced heating effects. Many MPM techniques involve exposing the sample to a strong beam of light during volume scanning, regardless of whether the focus is on the region of interest (ROI), leading to issues such as photobleaching and phototoxicity. The photon budget is challenging to reduce while ensuring detailed cell information, creating a balance between the required number of photons for high resolution and the risk of photon-induced tissue damage. To address this challenge, adaptive sampling methods are employed to selectively excite the pre-defined ROI either spatially or temporally. Strategies like using a mask or a temporally modulated source can be customized to target specific locations in the *x-y* plane, such as areas containing vasculature or neurons [52,53]. Scan durations can be adjusted during metabolic events to optimize photon efficiency in the time domain, with increased scanning time during events relative to non-event periods [54].

(2) Future directions

Future advancements in MPM will continue to prioritize improvements in resolution, penetration depth, imaging speed, contrast, and photodamage performance. These developments hold significant promise for enhancing scientific research focused on observing biomedical activities as well as applications in clinical diagnosis. Moreover, the integration of MPM with other imaging modalities such as OCT, PAI, and coherent Raman scattering imaging presents opportunities to gather information from diverse perspectives and overcome limitations of individual approaches. Additionally, leveraging the high throughput capabilities of MPM can facilitate the integration with large-scale AI networks to enhance imaging performance and uncover hidden information within the imaging data.

3.1.3 Up-conversion nonlinear microscopy

Up-conversion microscopy represents a paradigm shift in nonlinear imaging by utilizing lanthanide-doped upconversion nanoparticles (UCNPs) to convert low-energy NIR photons into higher-energy visible or NIR emissions via sequential photon absorption. Unlike conventional multiphoton processes, UCNPs exploit real intermediate energy states (e.g., Yb^{3+} sensitizers and Er^{3+}/Tm^{3+} activators), enabling efficient anti-Stokes emission under continuous-wave (CW) or low-power pulsed excitation. This offers significant advantages in excitation efficiency and photostability, thereby attracting considerable interest for deep-tissue microscopy. As illustrated in Figure 3a, the ladder-like, long-lived 4f energy states of lanthanide ions allow UCNPs to sequentially absorb the energy of long-wavelength NIR photons, undergo stepwise excited state absorption transitions, and generate short-wavelength NIR and visible emissions. This highly efficient process enables the use of low-power CW lasers to induce higher-order nonlinear emissions ($n > 3$) [55], effectively minimizing tissue damage while achieving high SBR in imaging. Moreover, as inorganic nanoprobes with multiple luminescence centers, UCNPs exhibit exceptional photostability, free from photobleaching and photoblinking, making them ideal for long-term and stable fluorescence imaging or monitoring. With advancesin sensitization strategies, more wavelengths within the NIR-I and NIR-II windows have been successfully employed for efficient up-conversion (Figure 3b), substantially reducing tissue scattering and water absorption. This process enables greater flexibility and improved selectivity in deep-tissue up-conversion imaging.

The feasibility and advantages of 2P up-conversion imaging for deep-tissue microscopy were first demonstrated by Esipova et al. [56] in 2012. UCNPs $NaYF_4$:Yb/Er (20/2%) can be excited by 980 nm lasers and emit fluorescence at 540 and 650 nm through 2P processes, making them suitable for use as a multiphoton probe. With polyanionic dendrimers modified on their surface, the stability, water-solubility, and biocompatibility of these nanoprobes have been effectively enhanced, enabling high-quality tissue labelling and imaging. In experiments, they demonstrated imaging of mouse cortical vasculature at a depth of ~400 μm using photon fluxes nearly 10^6 times lower than those typically used in traditional 2P imaging (Figure 3c) [56]. In 2020, the same group further optimized the surface modification strategy by employing the Janus-type dendrimers, achieving significantly improved labelling performance and enabling visualization of individual capillaries in the mouse brain down to a depth of ~1,000 μm with an excitation photon flux 5–6 orders of

magnitude lower than that used in conventional 2P microscopy [57]. Additionally, Chamanzar et al. [58] adopted Tm^{3+}-doped UCNPs as deep-tissue nanoprobes. By integrating them with passive micro-structured lightbulbs, the UCNPs could be implanted deep within tissues. The ability of UCNPs to generate multiple emission peaks was cleverly exploited to enable dual-functionality applications. Under 980 nm excitation, the 2P 800 nm NIR emission was used for imaging through 2 mm thick brain tissue, while the 3P and four-photon (4P) 450–475 nm blue emissions were used for optogenetic excitation of neurons. In a study by Khabir et al. [59], Er^{3+}-doped UCNPs were employed to investigate the penetration depth of solid nanoparticles in skin following treatment with various chemical enhancers. Using 2P up-conversion imaging, they found that chemical enhancers enabled UCNPs to disperse up to a depth of 500 μm in skin (Figure 3d). Additionally, the study demonstrated that polymer-coated UCNPs exhibit no toxicity to human skin.

Building upon the principles of MPM, 3P up-conversion fluorescence imaging offers enhanced optical sectioning by reducing the fluorescence emission volume and improving the SBR value. To achieve this, Liu et al. [60] designed a high-concentration Er^{3+}-singly-doped UCNP that can be effectively excited by a low-power 1,480 nm NIR-II laser and generate 3P emissions at 540 and 650 nm. In an artificial agarose phantom simulating tissue, they successfully achieved cellular imaging at a depth of 800 μm (Figure 3e). In another study, Wen et al. [61] further developed a core-shell UCNP structure consisting of a high-concentration Er^{3+}-singly-doped core and a low-concentration Er^{3+}-doped shell, enabling both 2P and 3P imaging with the excitation of 808 and 1,480 nm lasers. With these multifunctional nanoparticles, high-resolution cellular imaging was demonstrated through a 500-μm thick phantom (Figure 3f). To achieve higher contrast, resolution, and imaging speed, the high-concentration Tm^{3+}-doped UCNP with bright and fast-decay 4P 455 nm emission was used by Kostyuk et al. [62] for *in-vivo* deep-tissue imaging. In their experiment, clear single-particle fluorescence spots were observed in freshly excised spleen tissue of laboratory mice 15-minutes after intravenous injection of UCNPs, demonstrating the unique advantage of UCNP-based higher-order nonlinear processes in suppressing tissue autofluorescence.

Additionally, super-resolution imaging techniques based on UCNPs have advanced rapidly, offering significant improvements in resolution, photostability, and reduced laser intensity requirements. These include, but are not limited to, up-conversion AO

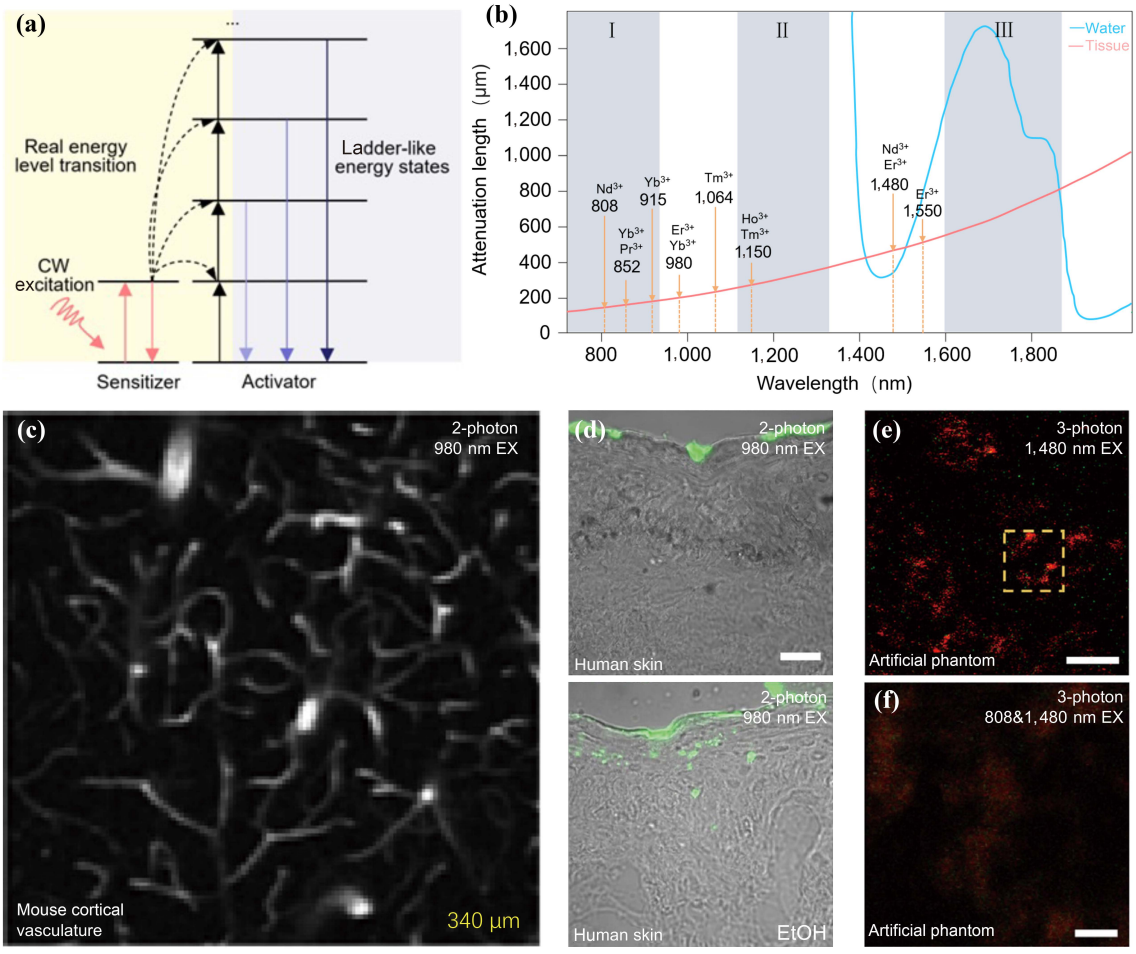


Figure 3 Deep-tissue microscopy by using up-conversion luminescence. **a.** Typical up-conversion process achieves nonlinear multiphoton emissions by sequentially absorbing multiple photons using real intermediate states of lanthanide ions [55]; **b.** selectable NIR excitation wavelengths for deep-tissue up-conversion microscopy; **c.** 2P up-conversion images of the mouse cortical microvasculature *in vivo* [56]; **d.** 2P up-conversion images of UCNPs disperse to a depth of 500 μm in skin [59]; **e–f.** 3P up-conversion images of cancer cells through phantoms [60,61].

nonlinear microscopy [63], up-conversion stimulated emission depletion (UC-STED) microscopy [64-66], surface-migration emission depletion (SMED) microscopy [67], up-conversion photon-avalanche (UC-PA) microscopy [68,69], up-conversion structured illumination microscopy (UC-SIM) [70], and others [71,72]. Moreover, the use of NIR laser sources in up-conversion super-resolution imaging effectively minimizes light scattering and preserves the integrity of the excitation point spread function (PSF) in deep tissues, which is critical for super-resolution techniques that require the use of a doughnut-shaped beam or streaked beam. For example, UC-STED combined with NIR depletion beams (e.g., 1,550 nm) has achieved 50 nm resolution in imaging dendritic spines through 93 μm of liver tissue [73].

(1) Challenges

Challenges remain in UCNP delivery, biocompatibility, quantum efficiency, excitation power requirement, and instrumentation complexity. The inherently low quantum yield of UCNPs reduces signal intensity, necessitating high excitation power, which in turn may lead to photodamage and tissue heating. Additionally, the surface chemistry of UCNPs must be carefully engineered to ensure effective delivery, cellular uptake, and minimal toxicity for *in-vivo* applications. The complexity and cost of specialized optical setups further hinder the widespread adoption of up-conversion imaging, while deep-tissue imaging resolution remains constrained due to PSF distortions and background fluorescence arising from nanoparticle aggregation.

To address these limitations, several strategies are being pursued. Engineering brighter and more efficient UCNPs, particularly through optimized core-shell structures and tailored dopant compositions, can enhance quantum yield and reduce dependence on high excitation power. Alternative excitation wavelengths, such as 808 nm or 1,480 nm, instead of 980 nm, can minimize tissue heating and absorption, thereby improving imaging contrast. Surface modifications using biocompatible coatings and targeted ligands can improve nanoparticle stability, biodistribution, and clearance, reducing potential cytotoxicity.

(2) Future directions

More efficient higher-order nonlinear excitation strategies are urgently needed to support the advancement of deep-tissue up-conversion imaging. Meanwhile, up-conversion super-resolution microscopy holds great promise for high-resolution and high-contrast imaging in deep tissue, representing a particularly promising application for techniques such as UC-STED, SMED, and UC-PA. UC-STED and SMED, which employ both Gaussian excitation beams and doughnut-shaped depletion beams in the NIR region, show great potential to overcome the light scattering issues associated with traditional STED. The ultrahigh nonlinear response of UC-PA may deliver the highest SBR value among all multiphoton imaging methods, enabling ultra-high-contrast super-resolution microscopy in deep tissue. As these methods continue to be refined, up-conversion super-resolution microscopy is poised to elevate deep-tissue imaging to new levels.

Furthermore, the development of compact and cost-effective excitation sources and detection systems will be crucial for broadening the accessibility of up-conversion imaging in biomedical research and clinical applications. Last but not least, AI-based computational approaches and deep-learning-based reconstruction algorithms can be integrated to enhance image contrast, suppress background noise, and correct PSF distortions. By integrating these technological advances, up-conversion imaging can move closer to meeting application requirements.

3.2 Diffuse light-based techniques

3.2.1 Near-infrared-II fluorescence molecular imaging

NIR-II fluorescence molecular imaging (NIR-II FMI) leverages the reduced scattering and absorption of light in the 900–1,700 nm window to achieve high-contrast imaging at depths exceeding multiple mm [74]. It is feasible to guide surgeons intraoperatively, helping with precise tumor detection, important functional tissues segmentation, and complete resection achievement [75]. By utilizing exogenous fluorophores (e.g., indocyanine green (ICG), quantum dots, or organic dyes) that can accumulate in target tissues and be excited by NIR-II light, this technique decodes scattered photons through computational reconstruction, enabling visualization of deep-seated tumors, vasculature, and nerves. Compared to traditional FMI using white light (WL) or the NIR-I spectrum, NIR-II imaging offers significantly greater penetration depth, reduced tissue scattering, and lower autofluorescence from biological tissues [76,77]. These advantages make NIR-II FMI particularly well-suited for deep-tissue biomedical imaging, providing higher resolution and improved SBR contrast.

Recently, NIR-II FMI has been applied in surgeries, showing great prospects to improve the surgical outcomes [75,78]. It is expected to detect occult lesions that are easily missed by traditional subjective parameters such as naked-eye inspection and palpation; visualize positive surgical margins to reduce the local recurrence of tumor; and visualize important organs and tissues to preserve their functions. For example, Hu et al. [75] built the first multi-spectral WL/NIR-I/NIR-II FMI system to guide surgeons during liver cancer surgery, showing comparisons of clinical outcomes with traditional NIR-I and NIR-II FMI. They found that NIR-II FMI was highly sensitive in the intraoperative detection of tiny hepatocellular carcinoma (HCC) lesions with a minimum diameter of 2 mm, which were missed by preoperative CT imaging, intraoperative ultrasound (US), and surgeons' inspection and palpation. In addition, NIR-II FMI could visualize positive margins missed by traditional NIR-I FMI. More importantly, NIR-II imaging-guided surgery showed an improved five-year survival rate by 15.1% compared to traditional surgery [78]. NIR-II FMI has also been studied in other clinical surgical treatments such as glioma [79,80], cystic renal mass [81], and lung cancer [82]. Meanwhile, the application of NIR-II FMI in the visualization of arteries, veins, and nerves also demonstrates its potential to preserve important functional tissues [80,83,84]. These classic examples of surgical navigation are summarized in Figure 4, and these pioneering efforts have paved the way for the clinical translation of NIR-II FMI platforms.

(1) Challenges

In NIR-II FMI, imaging contrast agents play a crucial role. Currently, ICG is the most widely used dye in intraoperative clinical trials of NIR-II FMI. Despite its clinical applicability, ICG presents several inherent limitations. One major drawback is its high false-positive rate (up to 10.5%) due to non-specific accumulation [85]. Additionally, ICG shows low photon

utilization efficiency at the tail end of its emission spectrum, resulting in insufficient fluorescence brightness and limited light scattering suppression, which hinder its effectiveness for deep-tissue imaging [86]. Furthermore, as a non-specific fluorophore, ICG lacks antigen-targeting ability, which can interfere with tumor detection. The weak fluorescence signal and non-specific characteristics may cause small tumor lesions to either lack detectable fluorescence signals or be masked by background fluorescence, reducing diagnostic sensitivity and increasing the false-negative rate [82,87]. Moreover, tumor heterogeneity further complicates imaging accuracy. Variations in molecular expression across different tumor regions can lead to uneven staining intensity, increasing the risk of false-negative results [88]. These limitations underscore the need for more advanced contrast agents with improved specificity, higher brightness, and better deep-tissue imaging performance.

(2) Future directions

To address the above-mentioned limitations, targeted probes (e.g., antibody-conjugated dyes) and environment-responsive agents (e.g., pH-/enzyme-activatable fluorophores) are under development [89,90]. Besides, fluorescent dyes with an emission peak in the NIR-II region and good biocompatibility can be more applicable to clinical applications of the NIR-II fluorescence imaging [91]. Meanwhile, due to the inherent scattering and absorption of light in tissue, optimization of existing imaging algorithms and equipment is key to future development. In terms of imaging algorithms, the introduction of deep learning and AI technologies has provided novel strategies for suppressing background signals. Image enhancement algorithms based on convolutional neural networks (CNNs) and generative adversarial networks (GANs) have been shown to effectively suppress stray light and enhance the contrast of target signals [92-94]. Time-resolved fluorescence imaging algorithms, by analyzing fluorescence lifetimes, can distinguish between short-lifetime background-signals and long-lifetime target fluorescence signals, thereby effectively reducing background interference [95]. Future integration with PAI and OCT could enable multimodal intraoperative platforms, combining structural, functional, and molecular data for precision surgery [96]. Last but not least, conducting more clinical trials to demonstrate the efficacy of NIR-II FMI is of crucial importance for facilitating clinical translation.

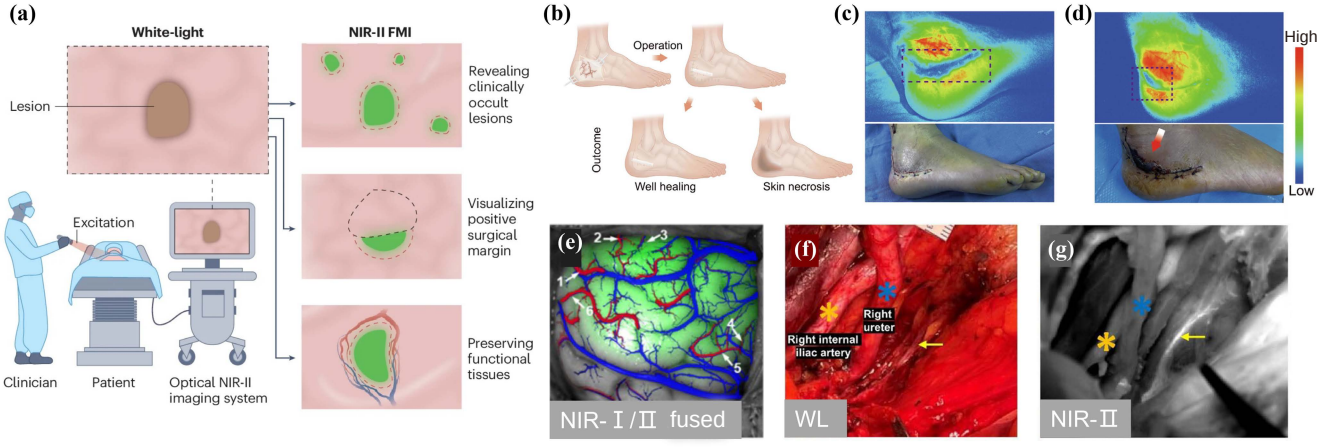


Figure 4 Clinical applications of NIR-II FMI in surgical guidance. **a.** Schematic overview of NIR-II FMI intraoperative scenarios, highlighting tumor detection, margin delineation, and functional tissue preservation [97]; **b.** schematic of open reduction and internal fixation of calcaneal fracture; **c–d.** postoperative bright-field and corresponding NIR-II images of the surgical incision, taken immediately and five days after the procedure, respectively [83]. The red arrow denotes the necrotic region. **e.** Multi-spectral FMI for simultaneously visualizing glioma (green, NIR-I, 700–900 nm), arteries (red, NIR-IIb, 1,500–1,700 nm), and veins (blue, NIR-IIa, 1,300–1,400 nm) [80]; **f–g.** intraoperative identification of pelvic autonomic nerves (yellow arrows) using NIR-II FMI [84]. WL: white light imaging.

3.2.2 Functional near-infrared spectroscopy

Functional NIR spectroscopy (fNIRS) is a dynamic brain imaging technology that has garnered widespread attention for brain function imaging, which benefits from its unique capabilities for monitoring hemodynamic changes in biological tissues by measuring wavelength-dependent absorption of hemoglobin under NIR light (700–1,000 nm). Oxygenated (HbO) and deoxygenated hemoglobin (Hb) exhibit distinct absorption spectra, allowing fNIRS to map cortical activity, muscle oxygenation, and tumor metabolism. Typically, fNIRS systems employ high-density source-detector arrays (>100 channels): the sources emit NIR light onto the scalp, and the detectors capture the scattered and absorbed light signals. Analyzing these light intensity changes allows the estimation of hemoglobin levels in cortical regions, providing insights into dynamic brain functional activity [98].

The recent development of hardware and software has significantly improved the usability, imaging quality, and analytical flexibility of fNIRS. Modern systems can be categorized into CW, frequency-domain (FD), and time-domain (TD) [98]. CW systems illuminate tissues with a constant-intensity light source and detect scattered light in transmission or reflection mode. FD systems modulate light sources at the hundred-MHz level, offering potential to better separate and resolve tissue absorption and scattering contributions compared to CW systems. TD systems use ultrashort pulsed lasers at the picosecond or femtosecond scale to illuminate tissues, with the emitted light recorded as TOF curves via single-photon counting. These curves

contain temporal information, which provides more depth-related information. Note that single-photon detection and picosecond-level time-resolved gating technologies present greater challenges in terms of system complexity and cost.

The number of fNIRS measurement channels has also seen a significant increase. Early systems with limited channels (4–10) could only detect brain activity in small, localized regions. In recent years, high-channel systems (NirScan, HuiChuang, China) with over 100 channels have enabled full-head monitoring of brain function, allowing researchers to systematically investigate the dynamic changes and connectivity of functional networks across the entire cerebral cortex [99]. Additionally, to meet the demands of movement scenarios, fNIRS systems have been improved in terms of miniaturization, extended battery life, and wireless data transmission, enhancing their portability or wearability [100].

To gain deeper insights into brain function mechanisms, fNIRS is commonly used to collect data during resting-state or task-state conditions. From a signal analysis perspective, biomarkers based on time and frequency domains are extracted and utilized for analysis. These features reflect the brain's activity patterns during task stimulation, such as activation amplitude and low-frequency oscillation patterns in cerebral blood flow [101]. To further investigate the collaboration among multiple brain regions, functional connectivity indices and the topological properties of different channels or brain regions can be mapped onto a brain network graph, providing a representation of inter-regional interactions. In the context of task activation response analysis, generalized linear models (GLM) are well-suited for analyzing task data in general scenarios. By constructing a design matrix, task-evoked signals can be separated from baseline signals, enhancing the robustness of evaluating brain region responses to specific stimuli. For more complex tasks, such as group tasks or cooperative behavior studies, wavelet coherence-based hyper scanning analysis offers greater adaptability [102].

In both clinical and non-clinical settings, fNIRS is widely applicable due to its dynamic and quantitative brain imaging capabilities, its resistance to electromagnetic interference, and its adaptability to various movements and natural environments. By analyzing changes in hemoglobin concentration, fNIRS enables the calculation of brain activation patterns and network indicators, providing robust quantitative support for assessing brain function disorders [98]. In neurodegenerative diseases such as Alzheimer's and Parkinson's, fNIRS facilitates early disease screening, treatment planning, and efficacy evaluation by detecting functional changes in the brain. In the field of mental health, it is employed for the auxiliary diagnosis of conditions such as depression, bipolar disorder, anxiety, and schizophrenia, as well as for monitoring medication effects. Due to its non-invasive and patient-friendly nature, pediatricians utilize fNIRS to explore neonatal brain development patterns [103] and assess brain function in children with attention deficit hyperactivity disorder or autism, assisting in the formulation of rehabilitation treatment plans. Additionally, in stroke patients, fNIRS is used to observe neural plasticity and brain reorganization following central nervous system damage, providing real-time evaluations of rehabilitation progress [104].

In other non-clinical settings, fNIRS is widely used in studying brain activity during both resting states and task performance. It has been applied to explore cortical activity during motor tasks, investigate frontal lobe cognitive functions in memory, attention, and calculation tasks, and monitor complex, multi-region brain cooperation involved in natural/social behaviors and driving. Additionally, fNIRS enables the study of interpersonal brain dynamics through hyper-scanning, which examines neural synchronization between multiple individuals during collaborative tasks [105]. Beyond cognitive and behavioral research, fNIRS has also been integrated into brain-computer interfaces (BCIs), where neuronal activity is converted into identifiable signals. When combined with BCI algorithms, this technology allows users to control external devices or receive sensory feedback through visual or auditory cues, expanding its applications in neurorehabilitation and assistive technologies.

Challenges and future directions: despite its potential, several critical challenges remain for fNIRS. In terms of imaging, the scattering of photons in brain tissue limits the spatial resolution and the ability to image deeper brain regions, with current imaging primarily focused on the cerebral cortex. Future advancements, such as higher-sensitivity detection technologies, novel imaging modes, and tomographic reconstruction algorithms integrated with advanced AI strategies, hold great promise for overcoming these physical limitations. Regarding the enhancement of signal usability, brain signals are subject to various interferences from motion artifacts, system physiological noise (e.g., due to vascular diastolic pressure, respiratory waves, heartbeats, and superficial cortical blood flow changes), and other factors [106]. Common methods for motion artifact correction in fNIRS include principal component analysis, wavelet filtering, and spline interpolation. But current algorithms have limited performance in separating these interferences. There is a pressing need for the development of more efficient and intelligent fNIRS processing and analysis tools [107]. In clinical applications, large-scale multi-center fNIRS trials are necessary to validate mature applications and cases, establish industry standards, and confirm their reliability and validity, while also facilitating expert consensus and clinical guidelines. Moreover, the current use of multimodal data (e.g., functional magnetic resonance imaging (fMRI), electroencephalogram (EEG), magnetoencephalogram (MEG)) is still in the exploratory phase. Methods and standards for simultaneous data collection and analysis remain underdeveloped, limiting the comparability of cross-study results and hindering the integration of multimodal data. In the future, the identification of novel fNIRS biomarkers, the development of task-specific analysis frameworks, and the integration of intelligent analysis methods will provide innovative solutions for analyzing data with more complex patterns. By continuously addressing these challenges, fNIRS will offer a more comprehensive and unique perspective on analyzing neural activity in complex brain regions. It will play an increasingly important and irreplaceable role in applications such as social and cognitive neuroscience, personalized clinical diagnostics, rehabilitation interventions, and BCIs.

3.2.3 Photoacoustic imaging

PAI combines optical excitation with ultrasonic detection to overcome the pure resolution dilemma of pure optical imaging

techniques in the diffusive regime. Short-pulsed NIR light absorbed by chromophores (e.g., hemoglobin, melanin, or exogenous agents) induces transient thermoelastic expansion, generating ultrasound waves (PA signals). These signals are received by one or an array of ultrasound transducers (USTs) positioned outside the tissue sample and reconstructed into images that reflect the spatial profiles of optical absorption contrast. Although the photoacoustic (PA) effect has been reported for more than one hundred years, PAI for tissue imaging started gaining significant attention in the late 1990s, and its targets range from sub-cellular organelles to human organs. Over almost 3 decades, PAI has emerged as one of the most transformative biomedical imaging technologies, encompassing advanced imaging methods, specialized contrast agents, and molecular probes, with diverse applications spanning fundamental life sciences and clinical diagnostics [108-111]. PAI generally reveals the optical absorption characteristics of the targets. There are intrinsic optical chromophores in living tissue, including hemoglobin, lipids, melanin, and water. Based on their unique absorption spectra, PAI can distinguish between different types of tissue. For instance, since hemoglobin molecules are highly concentrated in blood, PAI excels at non-invasive imaging of blood vessels and quantifying oxygen saturation (SO_2) by analyzing the distinct optical absorption of oxygenated and deoxygenated hemoglobin, a critical functional metric. Similarly, by tuning the wavelength of the laser source, spectroscopic PAI effectively monitors specific molecular tracers.

Based on the strategies to form images, PAI can be categorized into two major modalities: PA computed tomography (PACT) and PA microscopy (PAM). PACT acquires signals at various locations and reconstructs images using algorithms such as delay-and-sum, filtered back-projection, iterative model-based reconstruction, time-reversal, fast Fourier transform, and approaches based on neural networks. In contrast, PAM records local PA values (point or line) and directly stitches them to form 2D or 3D images, similar to the operation of the OCT. The lateral resolution of PAM is determined either acoustically or optically, leading to two subtypes: acoustic resolution PAM (AR-PAM) and optical resolution PAM (OR-PAM). PAM often operates by raster scanning a single UST, while PACT employs an ultrasound array with hundreds or even thousands of USTs. Generally, PACT is suited for mesoscopic and macroscopic imaging, while PAM operates in the microscopic to mesoscopic range. Similar to US imaging, both reconstruction-based and scanning-based image formation methods can be employed for endoscopy when the PA imaging probe is miniaturized. Since high-frequency US is heavily attenuated in the air, most PAI requires acoustic coupling, like water or US gel. An exception is PA remote sensing (PARS), which provides optical-resolution imaging in a non-contact manner, but with very limited imaging depth.

In recent years, PAI systems have undergone substantial advancements. For PACT, the number of array elements has increased to over a thousand, and the spatial dimension has expanded from 2D to 3D. Meanwhile, imaging speed has improved significantly, advancing from sub-hertz for 2D imaging to real-time 3D imaging. For PAM, innovations in laser sources and scanning mechanisms have greatly enhanced imaging speed. Additionally, the development of advanced USTs, including optically interrogated sensors [112,113] and transparent piezoelectric materials [114,115], continues to drive novel system designs and applications. Beyond hardware advancements, sophisticated image reconstruction algorithms, such as GPU-accelerated methods and deep-learning-based reconstructions, are being actively explored. In addition to system development, recent years have also witnessed significant progress in PA contrast agents and molecular tracers, which will be introduced in detail in Sect. 4.2.

For life science studies, with progress in both PAI system development and powerful molecular tracers, more and more research activities are being conducted to study both biological and pathological processes in live animal models. One major achievement is that state-of-the-art PAI systems now enable the study of *in-vivo* dynamic processes, including brain activity mapping [110], neurovascular coupling [116], cancer metastasis [117], tracer perfusion in organs [118], and heartbeat monitoring [119]. The translational study of PAI has made significant achievements. Researchers continue to explore the vast clinical value of PAI in detecting and monitoring therapy for different cancers [120], such as breast cancer, ovarian cancer, and thyroid cancer, by providing invaluable information on vascular structure and SO_2 levels. At the same time, PAI has demonstrated superiority in peripheral vascular imaging [121], fostering the non-invasive diagnosis of skin diseases (such as melanoma and psoriasis), peripheral artery diseases, and diabetic foot. Another breakthrough is PA brain imaging. Researchers have successfully imaged the adult brain that underwent craniectomy and acquired functional information consistent with fMRI [122]. At the same time, researchers are actively advancing hardware and algorithms to address the challenges posed by the human skull [123,124]. Besides clinical achievements, important milestones have also been achieved in commercialization. Several commercial PAI products have received regulatory approval for clinical use in Europe, the United States, and China.

Challenges and future directions: several key challenges remain before PAI can achieve widespread adoption, especially as a well-recognized clinical imaging modality.

One of the foremost challenges is identifying a clear clinical breakthrough. While PAI has demonstrated potential across a variety of diseases, it has yet to establish a definitive role in altering current diagnostic or treatment protocols. In the future, increasing both the variety of diseases studied and the scale of clinical trials is crucial for establishing PAI as a credible alternative or complement to existing diagnostic modalities. Larger, multi-center trials are essential for generating robust comparisons with current clinical practices.

In the pre-clinical and life sciences domains, the development of robust PA molecular tracers remains a critical bottleneck. The field is hindered by a shortage of diverse and potent tracers, particularly genetically encoded chromoproteins. Beyond traditional nanoparticles and dyes, there is growing interest in photoswitchable PA contrast agents and molecular tracers, which offer a promising solution to enhance the SNR. Breakthroughs in transgenic PA proteins—particularly functional ones—with tailored optical absorption properties are poised to significantly advance the application of PAI in life sciences.

The diversity of system designs and operational protocols can

also confuse end-users and complicate standardization efforts. Moreover, the high cost of advanced PAI systems—especially real-time PACT systems equipped with hundreds or thousands of sensing elements—further limits accessibility and adoption. In the future, advances in US sensors and detection technology, along with the development of compact, cost-effective pulsed light sources, are key to broader implementation. Concurrently, the commercialization of standardized, user-friendly PAI products will enhance accessibility and usability in both research and clinical settings.

In conclusion, PAI holds immense potential to revolutionize biomedical research and clinical practice. With rapid technological advancements and ongoing efforts to address current limitations, the field is poised to deliver impactful innovations and affordable solutions in the coming years.

3.3 Adaptive and computational optics

3.3.1 Adaptive optics

The highest spatial resolution of an imaging system is achieved with the tightest PSF, formed when all light rays converge to the same point in phase to maximize constructive interference (Figure 5a(i)). However, achieving this diffraction-limited imaging performance is practically difficult. This is because both system imperfections and sample heterogeneity can distort the wavefront, introducing optical aberrations (Figure 5a(ii)) that reduce the signal and degrade imaging resolution. Moreover, as imaging depth increases, aberrations often become more severe, making high-resolution, deep-tissue imaging a challenging task. AO [125-127] is a family of technologies that actively measure and correct aberrations. Originally developed to correct atmospheric aberrations in astronomical imaging [128], AO is now widely applied in microscopy and ophthalmology. In conventional AO implementations, if the aberration can be measured or determined, it can be corrected using a corrective device such as a deformable mirror (DM) or an SLM (Figure 5a(iii)). Aberrations can be determined by various methods, which can be broadly classified into direct and indirect wavefront sensing techniques.

In direct wavefront sensing, wavefront distortions are directly measured using a wavefront sensor such as a Shack-Hartmann (SH) sensor. An SH sensor consists of a lenslet array that segments and focuses the incoming wavefront, and a camera that captures the resulting foci pattern (Figure 5b). Local wavefront slopes are calculated from the focal displacements, and the entire wavefront can be reconstructed by assuming wavefront continuity [129]. In biological imaging, direct wavefront sensing requires a "guide star": a light-emitting source (e.g., back-scattered excitation, fluorescence, harmonic generation, etc.) within the sample. The guide star's emitted wavefront accumulates aberrations as it propagates to the wavefront sensor, where it is measured. Direct wavefront sensing measures aberrations with a single camera exposure, making it fast and well-suited for imaging biological samples with rapidly varying aberrations, either spatially or temporally. It has been applied for high-resolution imaging of the highly heterogeneous zebrafish brain [130] and developing embryos [131]. However, direct wavefront sensing is usually limited to transparent samples or opaque samples at shallow depths. This limitation arises because direct wavefront sensing depends on well-defined foci patterns for accurate aberration measurement. Scattering experienced by the light emitted from a guide star deep in the tissue degrades the foci pattern quality and affects measurement accuracy. To mitigate the effects of scattering, NIR guide stars have been employed, enabling direct wavefront sensing at depths of 700 [132] and 800 μm [133] in the living mouse brain; the latter work allowed proper visualization of fine dendritic structures at a depth of 770 μm (Figure 5c).

Wavefront aberrations can also be measured indirectly, based on acquired images without the need for a wavefront sensor. In zonal indirect wavefront sensing, the light beam at the objective lens back pupil is considered a summation of beamlets. When focused and propagating through an aberrating sample, each beamlet and its corresponding sub-wavefront picks up its local gradient, resulting in a displacement at the focal plane (Figure 5d). Similar to direct wavefront sensing, local wavefront slopes can be calculated from image displacements. This concept has been implemented in several ways: by sequentially illuminating each beamlet using pupil segmentation [134], by scanning each beamlet around the reference focus formed by full-pupil illumination [135], and by measuring multiple beamlets in parallel using frequency multiplexing [136,137]. Once the phase gradients are known, the relative phase offsets required for the final wavefront can be either calculated [129] or experimentally determined by finding values that maximize constructive interference [134]. Zonal indirect wavefront sensing is image-based, making it suitable for imaging opaque, scattering tissues at depths. In living mouse brain imaging applications, the pupil segmentation approach enabled diffraction-limited 2PF microscopic imaging at 450 μm [138] and high-resolution Bessel-focus 2PF volumetric imaging [139]. When applied with 3PF microscopy, frequency multiplexing AO enabled *in-vivo* synapse-resolving imaging of cortical and hippocampal neurons in the mouse brain, as well as high-resolution *in-vivo* imaging of neurons in the mouse spinal cord at depths [137] (Figure 5e).

Modal indirect wavefront sensing is another image-based AO technique. In modal AO, the wavefront is treated as a superposition of fundamental modes, for example, Zernike polynomials. The principle of modal AO is that an image achieves its highest quality only when aberrations are fully compensated. Using an adaptive device (e.g., a DM or an SLM), known aberrations defined in terms of modes can be introduced and sequentially optimized until the selected image quality metric is maximized. Modal AO can be readily implemented across various imaging modalities, provided an appropriate image metric is chosen for the specific modality [140-144]. Notably, when combined with 3PF microscopy, modal AO enabled near-diffraction-limited imaging of cortical spines and (sub)cortical dendrites at depths of up to 1.4 mm in the mouse brain *in vivo* [140] (Figure 5f). Compared with direct wavefront sensing, indirect wavefront sensing approaches, whether zonal or modal, do not require a wavefront sensor and only need a corrective device, making these AO techniques easier to implement.

Apart from the aforementioned conventional AO methods, other strategies have been developed. One approach is based on focus sensing [145-147], which determines the wavefront at the focal plane instead of the Fourier plane. This technique can correct both low-frequency aberrations as well as high-frequency

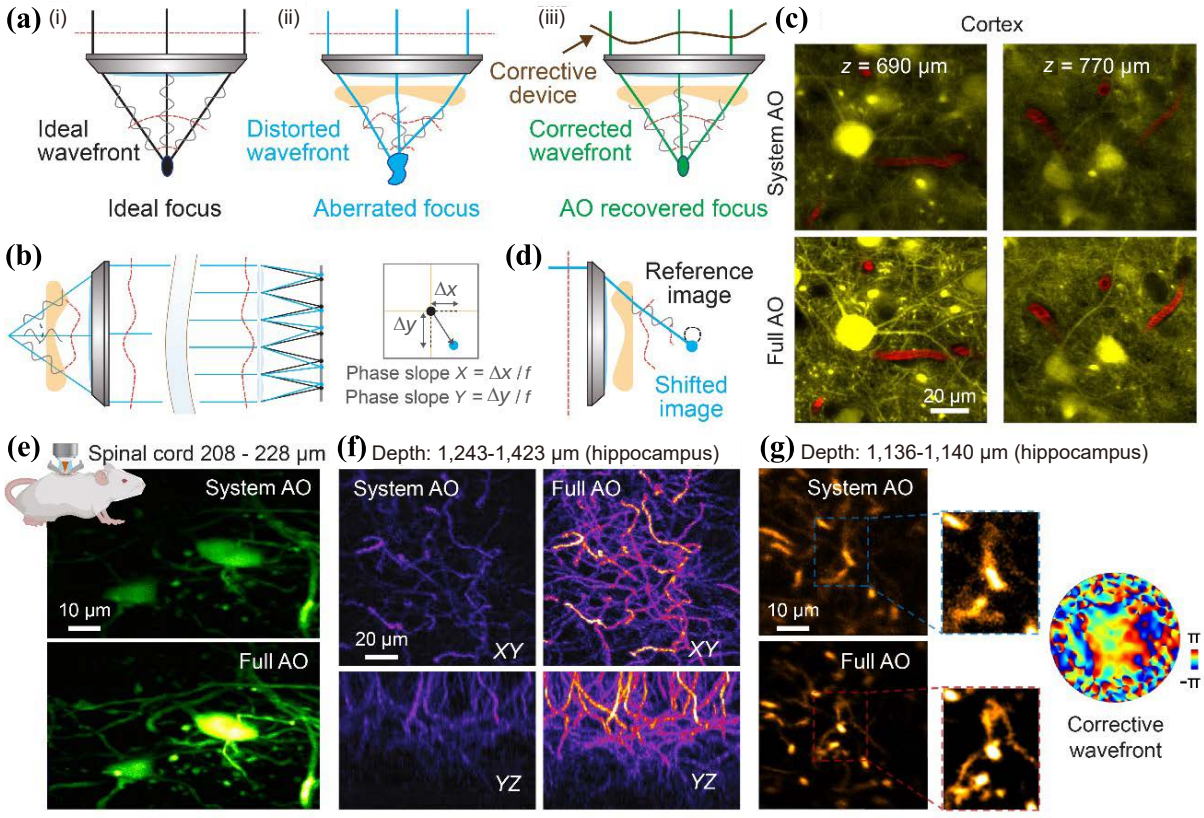


Figure 5 AO concepts, implementations, and applications in deep-tissue imaging. **a.** The effects of aberration on focus formation and improvements achieved through AO correction; **b.** principle of direct wavefront sensing [126]; **c.** 2PF imaging of the mouse cortex with direct wavefront sensing based AO [133]; **d.** concept of indirect zonal wavefront sensing; **e.** 3PF imaging of the mouse spinal cord using frequency-multiplexing-based indirect zonal AO [137]; **f.** 3PF imaging of mouse hippocampal dendrites using modal AO [140]; **g.** 3PF imaging of mouse hippocampal neurons using focus sensing AO [145].

scattering, making focus sensing AO particularly useful for deep-tissue imaging with MPM [145-148] (Figure 5g). Another AO strategy involves phase retrieval and phase diversity techniques [126,149-151], which computationally derive the phase information of the wavefront using intensity measurements of objects. Recently, computational or digital AO [152] techniques, especially those based on machine learning [153,154], have emerged as promising alternatives to hardware-based AO approaches. A recent study introduced a self-supervised machine learning AO algorithm [155], which can jointly estimate wavefront aberrations and recover 3D structural information from a single aberrated image stack. Initially demonstrated in widefield microscopy for *in-vivo* mouse brain imaging at shallow depths, this approach was later modified and applied to 2PF microscopy for deeper brain investigations of neuronal structures and functions [156].

(1) Challenges

By correcting sample- or system-induced aberrations, AO can restore the desired resolution, which is critical for accurately interpreting biological structures and functions. Despite its potential, AO remains a specialized technique inaccessible to many laboratories. The primary barriers are its high cost and the complexity of implementation, which often require specialized expertise and custom-built systems. These challenges limit the widespread adoption of AO in biological and biomedical research, particularly in smaller or less-resourced facilities. To fully realize the potential of AO, it is crucial to simplify its implementation, reduce costs, and develop user-friendly solutions that can be easily integrated into standard imaging workflows.

(2) Future directions

To enhance the impact of AO in biological and biomedical studies, next-generation techniques are expected to be both accessible and cost-effective. Furthermore, expanding the capabilities of AO will be crucial for broadening its applications. This includes achieving real-time aberration correction, enabling high-resolution imaging across larger fields of view, and ensuring reliable performance under weak signal conditions. Advances in computational approaches, such as machine-learning-based and digital AO methods, could play a pivotal role in overcoming these challenges. Looking ahead, the integration of AO into commercial imaging systems as a standard feature rather than a standalone module will mark an important milestone. Ensuring imaging systems consistently provide high-resolution or super-resolution images could make AO a standard microscopy tool, driving discoveries and potentially supporting medical applications.

3.3.2 Wavefront engineering

1) Optical phase conjugation

If tissue sample thickness is further increased, light will become completely diffusive, yielding seemingly random speckle patterns

that can no longer be processed by AO. To enable precise controlling (e.g., focusing) of scattered light, wavefront engineering of various parameters, such as amplitude, spatial, temporal, spectral, and polarization characteristics, has been proposed [157]. This capability shows great potential to revolutionize biophotonics by enabling deep-tissue optical imaging, manipulation, and therapy [158]. Among the different wavefront engineering approaches, optical phase conjugation (OPC) that leverages the time-reversal symmetry of wave equations has been shown to be promising.

OPC addresses the challenges of scattering by reversing the scattering process. This principle is based on time-reversal symmetry, as illustrated in Figure 6 [159]. It indicates that the propagation of light through a scattering medium (Figure 6a) can be reversed by generating a phase-conjugate wave that retraces the path of the scattered light (Figure 6b). This reversal effectively "undoes" the distortions caused by scattering, allowing the light to refocus at its source. Unlike other wavefront shaping (WFS) techniques, which often require iterative steps or complex retrieval methods, OPC enables information acquisition in a single measurement. Due to the dynamic nature of scattering in biological tissues, it presents a promising solution for controlling scattered light *in vivo*.

The concept of using OPC to correct image distortion was initially introduced in AO to correct for atmospheric aberrations in astronomy. It was later employed in the 1970s to mitigate image degradation caused by mode crosstalk in multimode fibers. In 2008, OPC was first applied to refocus scattered light after it passed through a sample of chicken breast tissue [160]. Early implementations relied on photorefractive materials [161-163], but the efficiency was limited. Although this method allowed for the control of a large number of modes and quick responses, it was not suitable for practical biological applications [161]. In 2010, Cui et al. [164] developed a digital OPC system that utilized high-performance cameras and SLMs, overcoming these efficiency limitations. This breakthrough enabled deep focusing (on the order of centimeters) within biological tissues [159], significantly advancing its potential for biophotonic applications.

Optical scattering is generally regarded as a deterministic process, but dynamic scattering in living tissues presents a significant challenge for wavefront engineering. A key issue is speckle decorrelation, which occurs due to factors such as blood flow, typically on time scales ranging from milliseconds to sub-milliseconds. Since high-contrast focusing relies on interference between multiple spatial modes, the ability to control these modes before speckle decorrelation becomes critical for optimal WFS performance [165]. Therefore, the average mode time—the time needed to manipulate a single effective spatial mode—serves as an important metric [166]. In general, a shorter average mode time enables the manipulation of more spatial modes before speckle decorrelates, leading to a sharper focus with a higher peak-to-background ratio (PBR). Currently, the mismatch between the rapid speckle decorrelation in live tissue and the relatively longer average mode time of WFS techniques presents a major bottleneck, limiting their practical use *in vivo*.

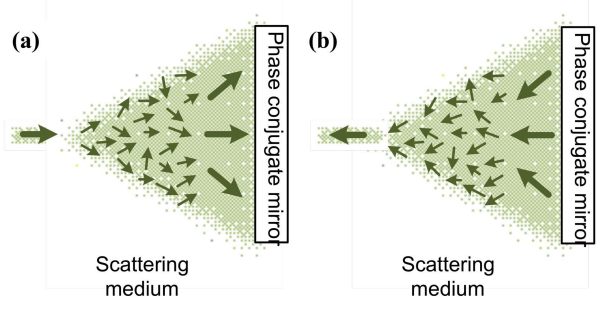


Figure 6 Illustration of the operating principle of OPC to counteract optical scattering [159]. **a.** Forward scattering process; **b.** phase-conjugated light retracing its original path.

Other WFS techniques typically have an average mode time on the order of microseconds, which means they can control only a few hundred independent modes within a 1 ms time frame. In contrast, systems based on OPC can achieve average mode times in the nanosecond range. Table 1 provides an overview of some representative high-speed OPC systems. For example, Wang et al. [167] developed an optical system using a high-resolution digital micromirror device (DMD, 1,920 pixel × 1,080 pixel) with a system runtime of 7.1 ms and an average mode time of 340 ns, enabling optical focusing through the back of a living mouse. In addition, high-speed SLMs based on nematic and ferroelectric liquid crystals have been employed, yielding average mode times of 220 ns [168] and 56 ns [169], respectively. Furthermore, OPC systems can be combined with ultrasonic guide stars for focusing light deep inside biological tissues. Using an SLM based on ferroelectric liquid crystals and a double-exposure wavefront measurement scheme, an average mode time as low as 92 ns was reported [169]. This was further reduced by implementing a quaternary phase encoding mask, which enabled a single-exposure wavefront measurement scheme, achieving an average mode time of just 29 ns [170]. This system demonstrated light focusing inside a live adult zebrafish with an optical thickness of approximately 40, highlighting the potential for future *in-vivo* applications.

Challenges and future directions: despite these advancements, the application of OPC for *in-vivo* imaging has seen limited progress, especially in the past few years. Beyond the challenges posed by dynamic scattering in living tissues, which affects the speed of system control, another significant obstacle is the guide stars used for focusing [171]. While various guide star types have been proposed, focused US remains the only non-invasive, freely addressable option compatible with OPC systems. However, its low modulation efficiency results in poor SNR in measurements. Additionally, the large size of the focused US spot leads to a broad

Table 1 Representative phase conjugation systems with a short average mode time

References	Resolution	Average mode time (ns)	Guide star
Ref. [167]	1,920×1,080	3.4×10^2	No
Ref. [168]	256×256	2.2×10^2	No
Ref. [169]	512×512	56	No
Ref. [169]	512×512	92	Yes
Ref. [170]	1,920×1,080	29	Yes

focal point, degrading focusing performance and rendering it nearly impractical. Although some studies have investigated statistical or iterative methods to improve focus quality, these approaches inevitably introduce substantial delays, making them unsuitable for real-time *in-vivo* applications. Therefore, to make OPC truly viable for biophotonics, it is crucial not only to enhance system speed but also to identify an appropriate guide star that is non-invasive, high-contrast, freely addressable, and capable of producing a small focal spot.

2) Iterative wavefront shaping

Iterative WFS (iWFS) shows another promising path to achieve wavefront engineering of diffused light. By optimizing the incident beam's wavefront, iWFS can redirect scattered photons to a common focal point within the tissue, creating a highly concentrated, focused spot [172]. First demonstrated by Vellekoop in 2007 [173], iWFS is one of the simplest forms of wavefront engineering, requiring no complex or unstable interference measurements. The method relies on light modulation, iterative algorithms, and feedback. As shown in Figure 7a, using feedback from the target focal point, the algorithm iteratively adjusts the wavefront modulation to correct the scattering paths, ultimately achieving high-contrast focusing deep within tissue.

The scattering distortions in deep tissue are highly complex, necessitating correction of over 10^6 optical modes—substantially more than is required in AO systems [158]. Moreover, within a millisecond, scattering channels in living tissue become incoherent. Therefore, to be effective, iWFS must handle large numbers of modulation modes and fast modulation rates, and exhibit both strong global search capabilities and rapid convergence speeds [174]. Light modulation of iWFS includes phase, amplitude, and polarization control, typically implemented with SLMs, such as liquid crystal spatial light modulators (LC-SLM) and DMDs [175]. LC-SLMs, though widely used, suffer from limited response speeds despite their high pixel count. DMDs offer advantages in modulation rate and mode number but suffer from low efficiency and reduced resolution due to binary modulation. Researchers have explored methods to improve modulation resolution, such as encoding methods that combine adjacent control pixels (Figure 7b).

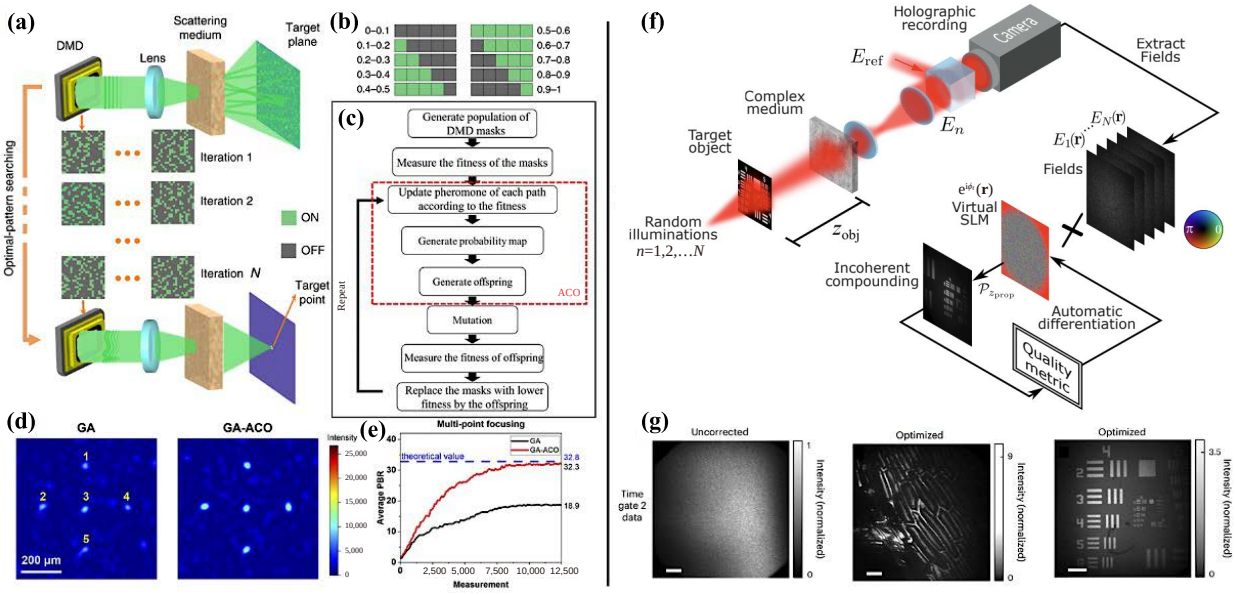


Figure 7 Iterative WFS. **a.** Flow of iWFS; **b.** encoding method of the digital micromirror device [174]; **c.** flow of an advanced optimization algorithm; **d.** experimental results of multi-point focusing; **e.** contrast of focus growth during the optimization [176]; **f.** image-guided iWFS; **g.** imaging results before and after image-guided iWFS [177].

As shown in Figure 7c, iterative algorithms often leverage intelligent optimization techniques inspired by natural phenomena [178], including genetic algorithms (GA), particle swarm optimization (PSO), and simulated annealing (SAA). These algorithms have evolved significantly [176], with newer strategies like dynamic mutation algorithms (DMA) and gradient-assisted shaping further improving the contrast and speed of deep tissue focusing (Figure 7d, e). The advent of AI has also contributed, with neural networks now accelerating iterative optimization. For example, neural networks can be trained on small datasets to predict the initial wavefront, guiding the iterative process, speeding convergence, and reducing the risk of local optima [179].

The iWFS process relies on feedback loop control, with unique feedback guiding the iteration. Early implementations could not provide feedback from within deep tissue, making non-invasive feedback a critical research challenge [180]. Current approaches often exploit interactions between light and materials or other signals, including fluorescence markers, photo-switchable proteins, magnetic particles, microbubbles, ultrasound, and Raman scattering. A promising recent development, image-guided iWFS (Figure 7f, g), uses iterative phase optimization to maximize image quality metrics, recovering high-contrast, diffraction-limited images from low-contrast speckle patterns, even when the target lies outside the FOV of memory effects [177].

(1) Challenges

While iWFS has shown significant promise in mitigating deep

tissue scattering, practical implementation remains a challenge. A key limitation is the trade-off between speed and the number of optical modes. Increasing the mode number often slows the process, and while some modes may be sacrificed to save time, this compromises resolution and exacerbates the rapid decoherence of biological tissue. Furthermore, focusing through tissue using iWFS does not directly lead to imaging. It often requires scanning within a limited FOV, resulting in suboptimal imaging depth and coverage. US-guided techniques have been proposed to overcome this limitation, but their larger feedback area diminishes resolution and contrast compared to optical methods. Recent model-based approaches [181], which use RI models of scattering media to compute focusing strategies, require significant prior knowledge and are not yet widely applicable.

(2) Future directions

Future advancements in multi-degree-of-freedom light modulation [182], new modulators and materials, and data-driven learning [183] could significantly enhance iWFS. Modulators capable of simultaneously controlling multiple degrees of freedom will allow for finer resolution and greater modulation mode numbers. Additionally, replacing traditional scattering models with deep neural networks, trained on large datasets, could provide more robust compensation for scattering aberrations, improving iWFS performance. Despite ongoing challenges, neural networks are increasingly recognized as a valuable tool, with the potential to drive a technological revolution in iWFS. Looking ahead, the evolution of iWFS is poised to advance deep tissue imaging. Addressing dynamic scattering could enable minimally invasive endoscopy using multimode fibers [184], potentially replacing current coarse glass fiber bundles used in medical applications. These fibers, with core diameters of only a few hundred micrometers, can transmit thousands of optical modes, unlocking new possibilities in endoscopic imaging. Moreover, while deep tissue imaging remains a focal point, the potential applications of iWFS extend far beyond this. For example, higher-bandwidth holographic technologies [185]—offering larger areas and broader FOV—stand to benefit significantly from the advancements in iWFS.

3) Transmission/reflection matrix

If light is injected through a diffraction-limited point (an input mode) on a disordered medium, it spreads into multiple modes and yields a complex speckle pattern at the output surface. The multiple scattering can commonly be seen as a linear and deterministic process [186]. Thus, the scattered optical field will be a linear combination of the medium's responses to each input mode. This linear superposition allows light propagation in such disordered media to be described using TM, which is shown in Figure 8a and reads

$$E_m^{\text{out}} = \sum_n t_{mn} E_n^{\text{in}}, \tag{1}$$

where E_n^{in} represents the n-th mode of the input field, E_m^{out} is the m-th mode of the output field, and t_{mn} denotes the component of the TM connecting the two modes. Similarly, the relationship between the incident field and the reflected field by the scattering medium can be described with a reflection matrix (RM). It is well-known that multiple scattering scrambles not only the wavefront of light but also its polarization states. In this case, vector TM enables the capture of the polarization behavior through the scattering media [187]. Since any polarization state can be a linear combination of two orthogonal polarization bases, the vector TM can be written as

$$\begin{bmatrix} E_m^{X(\text{out})} \\ E_m^{Y(\text{out})} \end{bmatrix} = \sum_n \begin{bmatrix} t_{mn}^{XV} & t_{mn}^{xH} \\ t_{mn}^{YV} & t_{mn}^{YH} \end{bmatrix} \begin{bmatrix} E_n^{V(\text{in})} \\ E_m^{H(\text{in})} \end{bmatrix}, \tag{2}$$

where the superscript X, Y, V, and H represent two orthogonal polarization states of the input and output field, respectively. Once the TM is calibrated or known, matrix operations enable precise control of the light field through the medium.

Experimental measurement of the TM through a scattering medium is usually performed using an interferometric method where an SLM modulates the incident light in a programmable manner [188-190]. However, these methods are invasive as they require access to both sides of the scattering media. Non-invasive methods are highly desired in deep tissue optics. In these cases, the calibration of TM relies on guide stars that provide feedback in the target positions. For instance, acoustic guide stars generated by the PA effect are effective tools as they leverage the relatively low scattering of ultrasound in optically scattering samples [191]. Fluorescence markers are another commonly used guide stars because fluorescence-based feedback signals can be easily separated from the excitation wavelength [192]. Recently, neural networks have been useful in TM calibration, which could help improve the robustness to environmental variations with intensity-only detections [193].

The TM method is powerful for shaping arbitrary output fields through a static scattering medium, for example, optical focusing or projection [188,194-196], as shown in Figure 8b. Notably, the coupling between multiple degrees of freedom of light in multiple scattering allows the use of TM for dynamic projections of vectorial images (Figure 8c) [197,198]. In addition, the TM/RM methods also play a useful role in optical imaging through or inside scattering media where computational reconstruction of the images of objects from the output speckle fields is required [199,200]. For example, a speckle imaging technique based on the RM can reconstruct the high-resolution images diffused twice by a multimode fiber (MMF) (Figure 8d) [201]. In particular, WFS facilitates the use of an MMF as an ultra-thin endo-microscope for deep tissue imaging *in vivo*. In this application, the imaging performance is highly sensitive to the bending of the fiber and the environmental disturbances, and thus, repeated TM calibration is usually required. For imaging dynamic scenes, a spatial-frequency tracking adaptive beacon light-field encoding method was recently developed (Figure 8e) [202], where a set of pre-calibrated TMs is adopted to ensure fast imaging through MMFs under various operating conditions.

Challenges and future directions: Despite its promise in wavefront engineering, TM methods also have some limitations that should be addressed for deep-tissue imaging. For instance, the number of measurements for TM calibration is typically proportional to the product of the number of input modes and output modes, making the calibration process highly time-consuming and computationally demanding, especially at high resolutions. This restricts the applicability of this method in dynamic imaging scenarios, such as deep tissue imaging in live

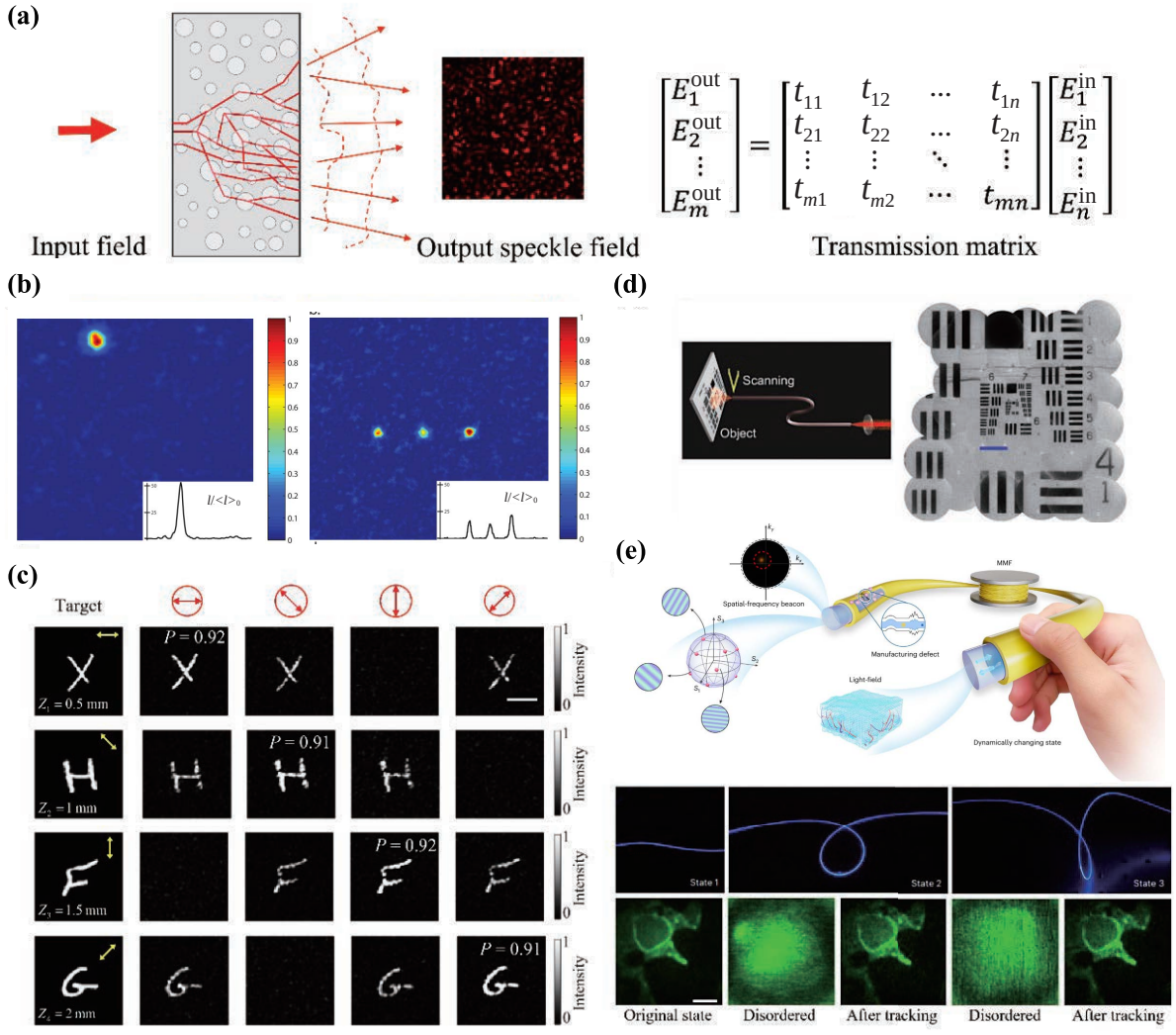


Figure 8 TM methods for wavefront engineering through scattering media. **a.** TM mathematically describes the relationship between the input and output fields through disordered media; **b.** optical focusing through scattering media [188]; **c.** vectorial images projection through an MMF via a vector TM [198], scale bar: 15 μm; **d.** imaging through an MMF leveraging TM [201], scale bar: 100 μm; **e.** single-fiber endoscopic imaging via the spatial-frequency tracking adaptive beacon light-field encoding method [202].

animals. Compressive sampling provides a potential solution by reducing the number of measurements. Additionally, the sensitivity of TM/RM to environmental perturbations, such as temperature change and mechanical vibrations, limits its applications in real-world settings. Existing approaches to mitigate this problem either require frequent calibration or necessitate pre-calibration, and both are only effective for small perturbations. AO algorithms or machine learning models may help to further address this issue.

3.3.3 Other methodologies

1) Minimally invasive fiber-based probes

The growing demand for *in-vivo* imaging continues to challenge existing technologies, particularly non-invasive techniques, which often suffer from insufficient resolution and limited imaging depth in fragile areas such as internal cavities or deep brain regions. These limitations make it difficult to observe fine microstructures with high precision. While invasive imaging methods offer better performance in biomedical applications, they come at the cost of significant harm to the subjects, necessitating alternative approaches. Moreover, challenges related to imaging depth, information capacity, imaging modalities, and mechanical scanning further restrict the effectiveness of current techniques. As a promising solution, MMFs have emerged as a novel endoscopic imaging technology, gaining increasing attention in the field due to their unique advantages [203]. With diameters of only around 50–200 μm, MMFs can support thousands of independent transmission modes, enabling high-resolution imaging and the acquisition of multimodal information. Additionally, their high flexibility allows them to navigate complex or confined environments, such as blood vessels, narrow cavities, or the interiors of precision instruments, making them particularly well-suited for minimally invasive deep-tissue imaging.

The different modes of light within the fiber interfere with each other during propagation. The unregulated input light field, after transmission through the multimode fiber, results in a disordered optical speckle pattern. Although these speckles are difficult to interpret, they still contain all the information about the input

light field. By measuring the transmission characteristics of the fiber, it is possible to recover the output light field. With the continuous development of WFS techniques, precise control, focusing, and scanning of light through MMFs have become achievable, enabling various imaging applications. Commonly used techniques include OPC, TM, and speckle correlation methods. As shown in Figure 9, in this model, both the input and output light fields are represented in matrix form as X and Y, respectively, with the influence of the multimode fiber, denoted as T, being assumed to be linear, i.e., $Y = T \cdot X$. The TM is measured by sending an incident wave to each basis vector in X. With knowledge of the TM, the target output field can be obtained by controlling the input field. In 2010, Popoff et al. [199] pioneered the use of computed TM to achieve light focusing through scattering media. In 2011, Čižmár et al. [204] applied this method to MMFs, successfully manipulating colloidal microparticles. Following this, researchers have implemented techniques to focus light with multiple wavelengths [205] and pulsed lasers [206], laying the foundation for nonlinear imaging techniques.

In the field of endoscopy, MMF imaging technology has rapidly advanced due to its unique advantages. Extensive studies have been conducted on improving imaging resolution, speed, image contrast, and system stability. Researchers have expanded the imaging capabilities of MMFs, achieving techniques such as confocal, far-field, and 3D imaging. Moreover, nonlinear imaging modalities have been successfully integrated into MMF imaging systems, such as single-fiber stimulated Raman scattering (SRS) imaging, 2PF imaging, and coherent anti-Stokes Raman scattering (CARS) imaging.

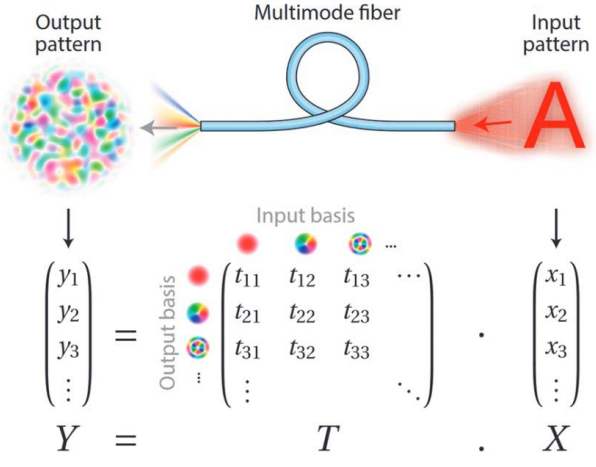


Figure 9 The transmission matrix model for MMFs [207]. X and Y are the vectors of complex coefficients describing the input field and output field, respectively, in a suitable basis. In this illustration, the input and output bases consist of the fiber modes.

In the development of system performance, mechanically moving the sample to acquire signals at different depths has limitations in practical applications for certain sparse tissue samples. In contrast, digital focusing [208] provides a more flexible approach to achieve focus at different depths of the sample. For other deep tissues or cellular samples, signal mixing at different depths can lead to a degradation in resolution and contrast. Digital pinhole techniques allow digital filtering of the signals, achieving 1.5 μm lateral resolution and 12.7 μm axial resolution [209] (Figure 10a). By measuring the round-trip TM and employing depth gating, it is possible to reconstruct images of different depths from a single RM, enabling 3D confocal reflection imaging [210] (Figure 10b). Imaging speed is a fundamental parameter that significantly influences the performance and applicability of optical systems. In 2022, Liu et al. [211] proposed a high-speed all-fiber imaging model using mode dispersion in long MMFs to convert 2D spatial information into 1D temporal information. With neural networks for image reconstruction, they achieved a frame rate of 15.4 million frames per second (Figure 10c).

Despite rapid technological advances, the bending and twisting of fibers, which leads to deterioration of the TM, limits the widespread application of fiber endoscopes. Researchers have proposed compensation methods for MMFs under dynamic deformation. By setting virtual beacons [212] or real guide stars [213], it is possible to track and predict the bending state of the fibers for compensation. However, in practical imaging scenarios, it is not always feasible to implement such beacons. Additionally, by adding reflectors or special metasurfaces to the fiber's distal facets [214], the disturbed TM can be computed, but the tracking speed is frequently insufficient to meet the requirements of imaging applications. In 2023, Wen et al. [202] developed a spatial-frequency tracking adaptive beacon light-field-encoded (STABLE) method. By detecting the single-pixel intensity at the fiber's proximal end, they achieved millisecond-level tracking speed for the fiber's bending status (Figure 10d).

To further expand the applications of MMF imaging, researchers have incorporated various advanced imaging functions and modalities into fiber imaging, significantly expanding the range of information dimensions captured by MMFs. In 2021, Leite et al. [215] proposed an MMF-based far-field endoscope that achieves observing distant objects with a working distance ranging from 20 to 400 mm. Based on this, time-of-flight (TOF) 3D imaging through MMFs has been developed. A TOF light detection and ranging (LIDAR) technique-based MMF system realized a depth resolution of 2.5 mm [216] (Figure 10e). By integrating nonlinear imaging, the MMF system achieved label-free imaging and provided chemical composition information. In 2017, Gusachenko et al. [217] achieved SRS imaging using a single MMF, obtaining Raman shift spectra of polystyrene microspheres and bacterial samples. In 2019, Trägårdh et al. [218] precisely controlled dual-wavelength pulsed lasers to achieve MMF-based CARS imaging (Figure 10f). In 2020, Turcotte et al. [219] demonstrated 2PF imaging with an axially extended focus through an MMF. In 2021, Cifuentes et al. [220] achieved polarization-resolved SHG MMF imaging, demonstrating the identification of collagen and myosin.

The rapid advancements of the above technology have established MMFs as effective microprobes, facilitating the integration of MMF imaging with various advanced techniques used for deep tissue imaging, including MPM and AO. Due to their minimal invasiveness, MMFs can be seamlessly inserted into or positioned adjacent to biological tissues, enabling high-resolution imaging of the internal microstructures within tissues.

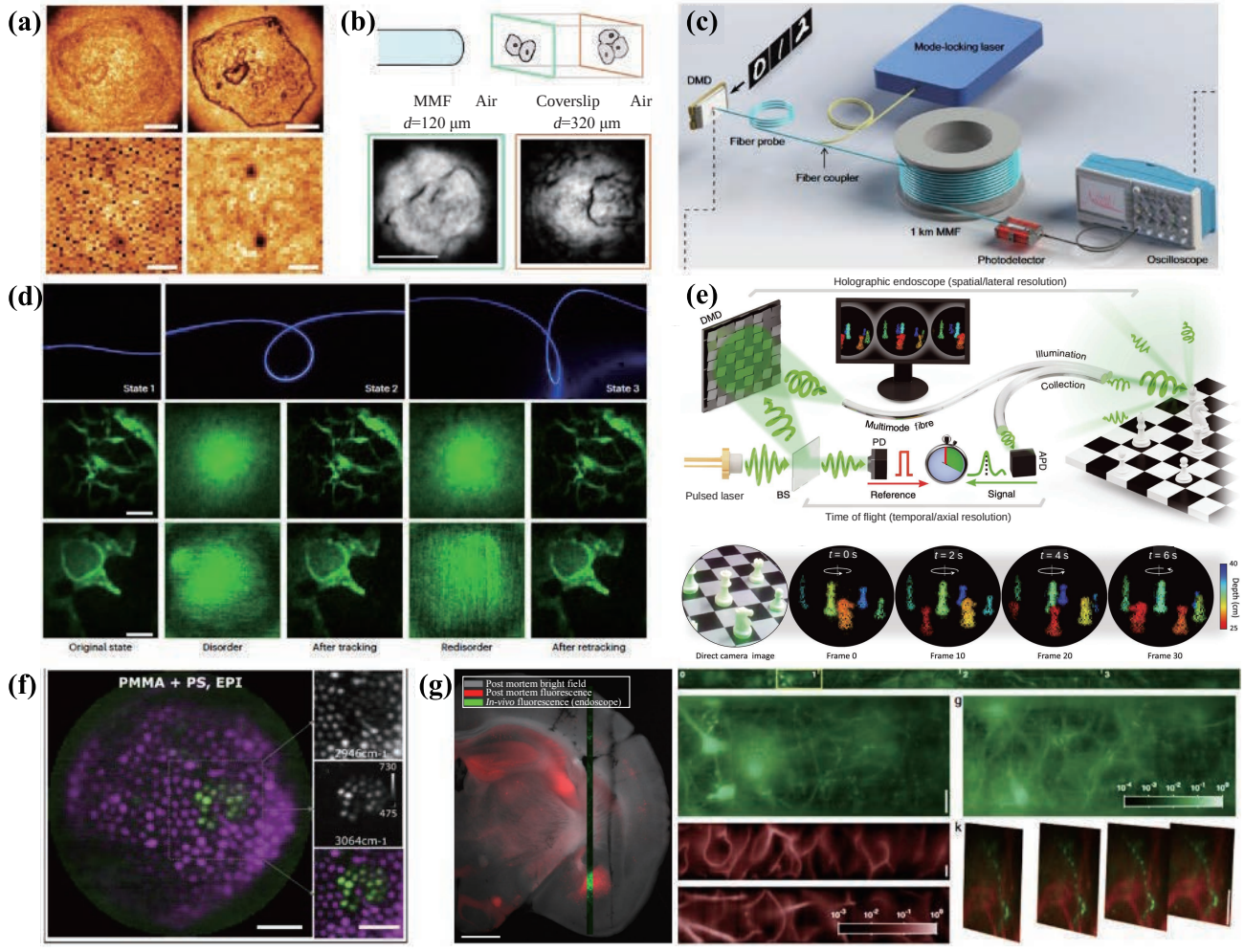


Figure 10 Advanced MMF imaging techniques and typical applications. **a.** Epithelial cell and 1μm polystyrene beads imaged with conventional method and digital confocal method [209]; **b.** confocal images of buccal epithelial cells deposited on the front and back surfaces of the coverslip [210]; **c.** the schematic of all-fiber high-speed image detection system [211]; **d.** the state change and imaging recovery under STABLE endoscopy [202]; **e.** the schematic of endoscopic LIDAR based on MMF and typical depth resolved images obtained with the system [216]; **f.** CARS images from a sample with both 2.5 μm diameter PMMA beads and 2 μm diameter PS beads [218]; **g.** record of endoscope progression throughout the whole-brain depth [221].

For instance, by inserting an MMF into the brain, it becomes possible to observe neuronal and dendritic activity, as well as the dynamic changes in blood flow within deep brain regions *in vivo* [221] (Figure 10g). Furthermore, when coupled with digital focusing techniques [222], the focal plane can be dynamically adjusted, allowing for the capture of fine structural details at various depths within the tissue. This capability not only enhances the depth of observation but also minimizes physical interference with the sample, offering a powerful tool for real-time, minimally invasive imaging in complex biological systems.

Challenges and future directions: In actual biomedical research and clinics, in addition to the susceptibility of MMPs to external perturbations discussed above, the existing imaging technologies are difficult to meet the needs of some applications in terms of imaging performance and image quality, such as excessively small field of view (FOV), difficulty in distinguishing signals from different depths, and insufficient axial resolution for 3D imaging. Limited by the diameter, NA, and working distance of a single fiber, the FOV is typically on the order of a hundred microns. The resolution and FOV of the imaging system are inherently a trade-off and must be balanced according to the specific requirements of the application. Increasing the working distance can expand the FOV, as in 3D far-field imaging, but this results in a decrease in both lateral and axial resolution, significantly reducing signal collection efficiency and affecting image SNR. In terms of imaging speed, the refresh rate of existing WFS devices (e.g., DMD refresh rate around 22 kHz) limits the acquisition time, with the time required to capture a single image growing as the number of pixels in the image increases. Combining deep learning [211] or compressive sensing [223] can improve imaging speed, but there are still limitations regarding imaging quality and sample types. Moreover, other dimensions of optical information are also crucial for comprehensive imaging analysis. Current technologies have achieved fluorescence and PA dual-modal imaging with a single fiber [224], as well as multimodal imaging combining reflection, fluorescence, and phase [225]. Further investigation is required to explore strategies for extracting broader modal information through fiber-based systems, thereby enhancing imaging capabilities to accommodate a wider spectrum of application requirements.

2) Digital holography

As discussed, biological tissues are inherently scattering media, which hinders the penetration of light and distorts the optical field. This scattering leads to blurred images and loss of depth information, making it challenging to visualize structures deep within the tissue. Since the holographic reconstruction is sensitive to the wavefront, digital holography is attractive for wavefront measurement and compensation rather than directly extracting target information from the scattered light. Applying digital holography to deep-tissue imaging offers a non-invasive and label-free method for visualizing 3D tissue structures. By capturing the phase information of light scattered within tissue, this technique yields morphological details and precise RI measurements. These data are valuable for analyzing cellular dynamics and potentially detecting disease markers, even in deeper tissue layers where traditional optical microscopy struggles due to scattering limitations. Advanced algorithms reconstruct the 3D image from the captured hologram, allowing researchers to study tissue structures with greater depth and detail than standard imaging techniques. To make holographic technology applicable to perturbed light, the imaging system is mainly improved in the following aspects: illumination and detection, optical path, multimodal integration, and algorithms, as shown in Figure 11.

In terms of illumination and detection, time/coherence-gated digital holography allows for the suppression of multiple scattered photons by leveraging the coherence properties of light to selectively capture only those photons that have traveled a specific optical path length [226]. However, this implementation cannot reject non-scattered aberrated lights, so wavefront aberration correction is often required [227]. Polarization imaging is another kind of scattering light suppression method that selectively detects specific polarization states. Chen et al. [228] combined in-line holography with polarization multiplexing and achieved single-shot complex field imaging through a diffuser. Ushenko et al. [229] proposed a holographic polarimetry method for layer-by-layer reconstruction of complex amplitude distributions and polarization maps within diffuse biological tissue. Li et al. [230] proposed a holography-based dual-polarization computational WFS method for imaging objects at variant depths behind dynamic turbid media.

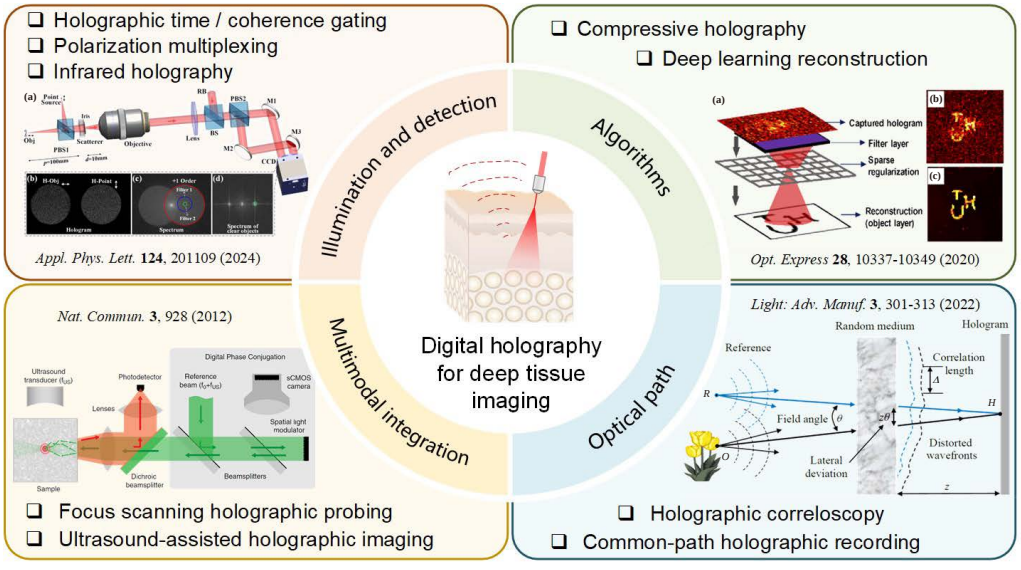


Figure 11 Technical category of digital holography for deep-tissue imaging [227,230-232].

Compared to visible light, short-wave infrared light with wavelengths between 760 and 1,500 nm can penetrate deeper into human tissues, reaching depths of approximately 5 mm to 10 mm. It can directly affect blood vessels, lymphatic vessels, nerve endings, and subcutaneous tissues. Lu et al. [233] proposed quantitative phase imaging of cells through turbid media based on infrared digital holographic microscopy. The wavefront distortion caused by scattering can also be compensated for by merging with other technical solutions. For instance, by combining ultrasound modulation and digital phase conjugation through phase-shifting holography, a deep-tissue focal fluorescence image can be collected and measured [232]. Holographic technology is also used to assist dynamic adaptive wavefront compensation to achieve 2PF imaging [147].

In addition to suppressing the scattered light, "bad" light can be converted into "good" light by configuring the optical path. Holographic correloscopy utilizes the second-order or fourth-order spatial field correlations to realize 3D imaging through a diffuser [234]. The image is reconstructed by analyzing spatial intensity correlations within the speckle field generated from light scattered through a medium with turbulent phase variations [235]. Another optical path configuration, called common-path holographic recording, has common distortions of the reference and object waves, which cancel each other through interference [227]. Ohta et al. [236] proposed a technique for 3D imaging through a highly heterogeneous double-composite random medium by common-path phase-shift digital holography, and experimentally demonstrated its capability to overcome the limitations of traditional digital holography methods.

From an image processing perspective, the ballistic photons carry a signal, while the scattered light is noise. Zhang et al. [231] utilize proposed noise suppression for ballistic photons based on

compressive in-line holographic imaging through an inhomogeneous medium. Recently, deep learning methods have been introduced into holographic scattering imaging. Liao et al. [237] proposed a deep learning based method to make the off-axis hologram immune to the speckle noise introduced by the scattering medium.

3) Speckle contrast/correlation imaging

When coherent light illuminates biological tissue, the backscattering light forms a speckle pattern. Built upon statistical analysis of these speckle patterns, laser speckle contrast imaging (LSCI) has emerged as a label-free, non-invasive, wide-field optical imaging technique for quantifying the speed of the moving particles. This can be utilized to visualize microcirculation and map blood flow speed with high spatiotemporal resolution. The versatility of LSCI has driven its widespread adoption across basic research, preclinical studies, and intraoperative practice, including applications in neurosurgery, dermatology, ophthalmology, and cardiovascular studies [238-243].

In LSCI, the intensity recorded at each pixel of the photodetector is the superposition of the amplitude of multiple speckle fields due to the integration effect of the photodetector during the limited exposure time. The speckle contrast K is defined as the ratio of the standard deviation of the integrated intensity to its mean value [244]. It is characterized by the temporal autocorrelation function $g_2(\tau)$ of the temporal intensity and linked to the temporal autocorrelation function $g_1^n(\tau) = \exp[-(\tau/\tau_c)^n]$ of the electric field through the Siegert relation [245]. The measured K relies on several factors, including scattering regime, particle motion type, ergodicity, light polarization, exposure time, speckle size, statistical uncertainty, and instrument noise:

$$\begin{aligned} K^2 = {} & \frac{2}{T}\beta\int_0^T\left(1-\frac{\tau}{T}\right)\left\{\rho^2\left[(1-d)\left|g_1{}^{n=1}(\tau)\right|\right.\right. \\ & \left.+d\left|g_1{}^{n=X}(\tau)\right|\right]^2+(1-\rho)^2\Big\}\mathrm{d}\tau \\ & +\frac{2}{T}\beta\int_0^T\left(1-\frac{\tau}{T}\right)\left\{2\rho(1-\rho)\left[(1-d)\left|g_1{}^{n=1}(\tau)\right|\right.\right. \\ & \left.\left.+d\left|g_1{}^{n=X}(\tau)\right|\right]\right\}\mathrm{d}\tau+C, \end{aligned} \tag{3}$$

where T is the exposure time, ρ denotes the dynamic scattering component, and β is the coherence loss. C is the offset caused by noise, X and d depend on the type of dynamics.

Many efforts have been made on physical models, imaging methods, and image processing strategies for improving the quantitative interpretation of speckle-based blood flow speed [246]. The scattering field in the presence of a static scattering medium is a superposition of static and dynamic scattering fields. Since the static scattering field is non-ergodic, the integrated intensity at the photodetector also fails to meet ergodicity. The underestimation of blood flow caused by non-ergodicity is addressed by modeling the dynamic scattering proportion through spatial and temporal contrast analysis or multi-exposure speckle imaging [247-249]. The photodetector noise hides the actual signal of intensity fluctuation in the fast flow regions, where the corresponding speckle contrast is as small as the noise. Noise correction on speckle contrast can improve the sensitivity and linear response range of speed measurements [250,251]. In practical applications, the local contrast calculated from a finite statistical sample does not equal the ensemble contrast. Due to the heterogeneity of biological tissues, expanding the spatial window to make the local contrast approach the global contrast is impractical. The quantitative relationship between statistical sample size and speckle contrast is derived to correct the biased estimation [252,253]. To further address this issue in slow flow regimes, the auto-inverse covariance is developed for unbiased estimation of the blood flow speed and demonstrates the reduction of statistical noise [254]. When the number of sampling frames used for the calculation of speckle contrast is limited, statistical noise can overwhelm the flow-induced signal and cause inaccurate blood flow measurements. This issue is particularly prominent in real-time blood flow monitoring applications that require measurement of rapidly changing blood flow. Various denoising algorithms were developed to improve the SNR of LSCI for accurate blood flow mapping [255-257]. Motion can cause misalignment of consecutive speckle images, introducing errors into LSCI measurements. Non-rigid motion estimation and image registration method are proposed to address the artifacts due to the movements, such as respiration, heartbeat, or peristalsis [258,259]. Heterogeneous regression analysis combined with dual-wavelength imaging addresses motion artifacts caused by inter-frame misalignment and intra-frame blurring in LSCI [260,261].

Additional advancements have transitioned LSCI from primarily qualitative methods to quantitative approaches and improved their temporal and spatial resolution [262-265]. Dynamic light scattering imaging (DLSI) provided the optimal scattering models for LSCI by measuring speckle intensity temporal autocorrelation, enabling a quantitative understanding of the scattering dynamics across a wide field [266]. DLSI requires a high-speed camera (up to 20,000 fps) to accurately capture dynamics in smaller vessels and parenchyma. With the aid of an elliptical aperture that elongates the speckle pattern, rolling shutter speckle imaging (RSSI) achieves single-shot imaging of cerebral blood flow for the temporal decorrelation of dynamic speckle fields with a consumer-grade rolling shutter CMOS sensor [267]. There is a trade-off between spatial resolution and temporal sampling, as the elongated speckle patterns reduce spatial detail. Wide-field intensity fluctuation imaging measures the temporal autocorrelation function of the light intensity over a quasi-wide field based on a two-pulse modulation within a single exposure using standard cameras with limited frame rates [268]. Precise pulse modulation control and synchronization can be challenging to implement in biological settings. Transmissive-detected LSCI (TR-LSCI) was designed to monitor blood flow in thick tissues using NIR light [269]. Dual-exposure temporal laser speckle imaging resolved the issue of overestimating background flow velocity in transmission laser speckle imaging and enabled simultaneous angiography and blood flow velocity measurement at the microvascular level [270].

Challenges and future directions: the major limitation is that LSCI provides relative values rather than absolute speed of blood flow due to the difficulty in determining the PSF of LSCI in biological tissues. One solution is to calibrate measured metrics

with known speed through controlled phantoms. Another one is incorporating with other optical techniques, such as OCT, which was demonstrated to have the ability to measure the absolute blood flow speed [271-273]. Another limitation of LSCI is the shallow penetration depth, which limits the ability to image deeper vascular structures. To improve its penetration depth, several strategies have been performed through the idea of diffuse correlation spectroscopy, where the light that is refracted in areas farther from the penetration zone reaches deeper tissues [274-279]. LSCI holds significant potential for a wide range of clinical and research applications. The development of portable LSCI devices is anticipated to extend their application in point-of-care diagnostics, particularly for monitoring wound healing, skin conditions, and retinal blood flow in outpatient settings. In addition, the integration of LSCI with multimodal imaging systems could facilitate a more comprehensive assessment of structure and function at multiple scales and parameters, which would be particularly valuable in neurology and oncology.

4. Chemical and material innovations

4.1 Tissue optical clearing

The development of the aforementioned series of optical technologies no doubt enhances the application capabilities of optical imaging in deep tissues, providing important tools for deep-tissue observation, and can be used very effectively in combination with chemical agents [280]. The emergence of tissue optical clearing (TOC) techniques has provided an innovative way for deep-tissue imaging by altering the intrinsic optical properties of tissues with chemicals to render them "transparent" to light, which can fundamentally overcome the strong scattering limitations. As is known, scattering of light within tissues is a result of the RI mismatch between the low RI, water-rich components, like interstitial fluid and cytoplasm, and the high RI components rich in lipids and proteins, such as the cell membrane, myelin sheaths, and myofibrils. Current TOC techniques often improve RI matching by entailing the interaction and exchange of endogenous tissue constituents with exogenouschemical agents, so-called optical clearing agents (OCAs).

The history of TOC can be traced back to 1914 when Spalteholz first used the organic solvents to clear *ex-vivo* large tissues. Until around the 1990s, when photonics technologies were already well developed, and Tuchin et al. pioneered the *in-vivo* applications of TOC. In the past decades, a variety of TOC techniques have substantially emerged to facilitate deep tissue imaging [281-283]. The TOC methods can be broadly classified into hydrophobic (solvent-based) and hydrophilic (aqueous-based) methods in terms of the nature of their final RI matching OCAs [284]. This is usually done in conjunction with processes such as dehydration, decalcification, delipidation, or hyperhydration, aiming to create a homogeneous RI, as well as decolorization for pigment-rich tissues to reduce tissue absorption. Typically, hydrophobic TOC methods initiate with a dehydration phase to eliminate tissue water, followed by solvent immersion for lipid extraction and RI matching, while hydrophilic methods employ aqueous solutions for permeabilization and RI matching.

Numerous TOC methods, such as the 3DISCO, CUBIC, CLARITY, and various derived protocols, have been successfully combined with light sheet microscopy to achieve 3D mapping and profiling of whole organs and whole bodies *in vitro* [281]. For instance, the recently reported SOLID, a hydrophobic method that not only minimizes tissue distortion but also delivers outstanding clearing capabilities, establishing a reliable and robust pipeline for comprehensive whole-brain mapping [285]. Additionally, specific methods have been tailored for particular imaging modalities. For instance, SeeDB2 has been developed for super-resolution imaging deep inside tissues, while rDISCO is designed for Raman dye imaging in millimeter-thick samples [281]. The broad applications of *ex-vivo* TOC span diverse organisms from mammals to sauropods, from terrestrial to aquatic creatures, and from vertebrates to mollusks, shedding light on the study of neuroscience, development, tumor metastasis, as well as many interesting events in life sciences (Figure 12).

In response to the need for *in-vivo* imaging in thick tissues, TOC methods have been developed to mitigate the inherent risks and side effects associated with traditional surgical window-based observation techniques. Different from the *ex-vivo* methods, methods for *in-vivo* applications need to take safety as the first consideration. Existing *in-vivo* TOC methods mainly employ RI matching strategies through temporary and reversible exchange between OCA and tissue water, tissue dehydration, and collagen dissociation. The OCAs utilized are mainly the high-concentration of biocompatible sugars, sugar-alcohols, or CT/MRI contrast agents, assisted by the physical, chemical, or biological penetration enhancers, while for the hard tissues, such as skull, an EDTA decalcification process was generally included before RI matching.

For skin, the biggest organ of the body, different formulas of OCAs have been crafted to render the dorsal, ear, and footpad skin transparent, providing a TOC window for imaging blood vessels and cellular structures, including cancer cells [286]. Not only does this enhance the visualization of dermal vasculature and blood flow with higher resolution through LSCI and OCT, but it also enables intravital fluorescence confocal (IVFC) microscopy, LSCM, and FLIM to detect and image fluorescent cells at greater depths with increased signal intensity [282,287]. In the quest for *in-vivo* brain imaging, Zhu's group introduced the innovative concept of a skull optical clearing window (SOCW) without the need for invasive craniotomy. A series of advancements have been reported in recent years [281], such as SOCW for imaging of the brain cortex at synaptic resolution, USOCA for switchable imaging, VNSOCA for NIR-II imaging, as well as the through-intact-skull (TIS) chronic window [288] for imaging in awake animals. A typical application of the TIS window is the combination with RUSH3D for cortex-wide monitoring of immune cell dynamics with single-cell resolution following traumatic brain injury (TBI), which is challenging for intertwined reasons [289]. Besides, Wu et al. [290] have recently developed an intervertebral clearing window using Iodixanol, a clinically utilized CT-contrast agent, applied to the ligamentum flavum, achieving long-term imaging of the mouse spinal cord for simultaneous visualization of various structures, such as axons, myelin, microglia, blood vessels, collagen, and lipids. The concept of using CT and MRI contrast agents as OCAs leads us to multimodal imaging technologies for future clinical applications. This was first demonstrated in an *in-vivo* cancer model by

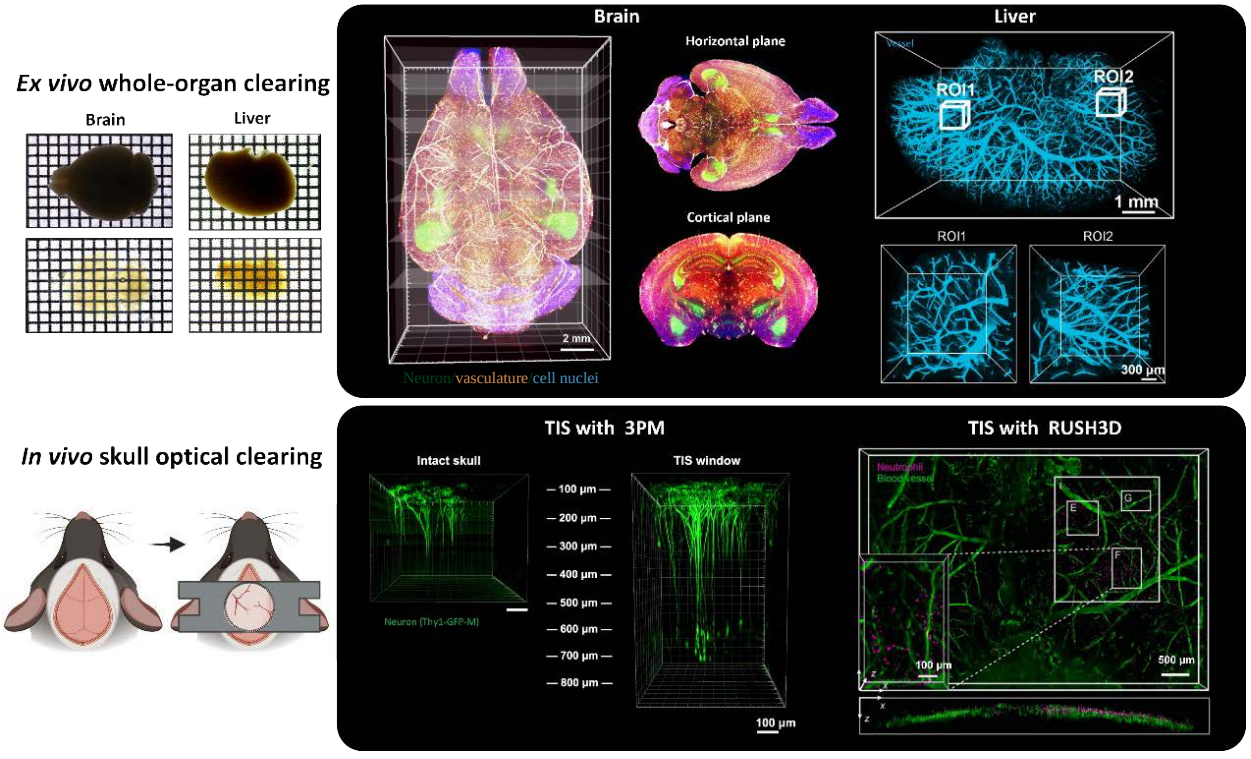


Figure 12 Tissue clearing for deep tissue imaging for applications from *ex vivo* to *in vivo*. The top panel shows the *ex-vivo* clearing for imaging [285], the bottom panel shows the *in-vivo* SOCW for 3P microscopy and RUSH3D [289].

intravenous injection of the MRI contrast agent gadobutrol for simultaneous contrast-enhanced tumor imaging with MRI and red fluorescent protein fluorescence [291].

Notably, a recent work [286] reported a strong confirmation of another counterintuitive strategy for RI matching by using the absorbing molecules, which was proposed in 2004 by Tuchin et al. [282] and proved on hemoglobin and whole blood. However, it is usually neglected because the absorption enhances the attenuation of the light in tissue [292]. It is well known that the RI can be represented as a real part and an imaginary part, the former of which is associated with dispersion and the latter with absorption. So that strongly absorbing molecules dissolved in water can significantly change the real part of the RI of an aqueous medium at the wavelengths close to the edge of the absorption band. This phenomenon is described by the Kramers-Kronig relations and allows effective RI matching to be achieved to obtain optical transparency in living animals [282,286], providing a new perspective for TOC.

It is important to note that TOC using unique OCAs such as glycerol, transparent in a wide range of wavelengths from deep ultraviolet to infrared, allows opening temporary windows of transparency of tissues in various areas of the spectrum [293] for the implementation of diagnostics or therapeutic effects and can be used in today's medicine, for example, to improve the quality of PUVA therapy.

(1) Challenges

Despite the significant strides made in this field, there are still some limitations that need to be addressed. As a chemical means for deep tissue imaging, TOC inevitably employs various chemical agents that need to be effectively delivered into tissues. However, *in-vivo* applications, like human skin, are currently challenged by the thicker and more resilient nature of human skin, particularly the significant barrier function of the stratum corneum. In the case of large-volume tissues, such as the brains of non-human primates and humans, the uneven distribution of OCAs can result in incomplete clearing of deeper tissues. This also necessitates extended incubation periods to attain the necessary level of transparency, which is quite time-consuming. Despite the availability of objectives with extended working distances and high NAs, the image quality across intact samples can still suffer from degradation. Moreover, the complex TOC process, which involves selecting appropriate OCAs, devising a step-by-step protocol, and managing parameters with precision, is largely dependent on the technicians' expertise and predominantly manual in operation. This would place a considerable burden on human resources when tasked with the herculean task of clearing a vast array of tissue samples.

(2) Future directions

To address these challenges, on one hand, future research endeavors might persist in the quest for and development of non-toxic, faster-acting OCAs that can be compatible with a more extensive array of tissues, notably encompassing human tissues. It is also necessary to adapt well-known, but so far little used, methods for the delivery of OCA, clinical methods of drug delivery, such as intravascular injection, injection directly into an organ, oral, pulmonary, vaginal, or rectal OCA administration. On the other hand, for the large samples, the integration of TOC and mechanical slicing is emerging as a trend to ensure uniform imaging quality throughout the intact samples at the organ or body scale, as demonstrated by techniques like the mELAST with

MEGAtome [294]. Similar technology should work for UV excitation as well [282]. Furthermore, automating the TOC processes could substantially alleviate manual labor and boost efficiency, rendering it practical for managing extensive studies and clinical diagnostics. Additionally, as animal testing is phased out, the use of new approach methodologies—such as organoids and organs-on-a-chip—will be promoted, and the TOC should play an important role in the 3D visualization of these human-relevant micro-tissues to replace animals in drug-discovery and biomedical research pipelines [295].

The application of TOC extends well beyond the frontiers of basic life science research, with significant potential clinical implications. For instance, the development of high-efficiency, safe, and niche-targeting *in-vivo* TOC methods tailored for different human skin or mucosal types is of paramount importance for specific clinical applications such as pediatric injections, dermatoscopy, bronchoscopy, colonoscopy, angiography, and many others, in the interests of cancer and diabetes mellitus diagnosis. A new era is now opening in the optimization of phototherapeutic interventions using TOC for both cancer therapy [282] and the suppression of deep-seated pathogens [296]. The potential of *ex-vivo* TOC techniques to revolutionize clinical pathological diagnosis is also noteworthy, with the promise of transitioning from 2D to 3D pathology for more precise diagnoses combined with advanced imaging techniques [297]. The rapidly advancing AI technology is also expected to aid the applications of TOC, particularly in processing and analyzing the massive image data, and in the determination of optimal protocolsfor cutting-edge life science research and clinical practices.

4.2 Contrast agents and molecular probes

Contrast agents and molecular probes play a pivotal role in enhancing imaging quality and specificity in deep-tissue optical imaging, especially in fluorescence imaging, PAI, and up-conversion imaging. Those probes typically aim to optimize the optical properties of probes. In fluorescence imaging, materials are engineered to maximize fluorescence quantum yield, stability, and brightness, enabling precise and sensitive detection of biological targets. PAI utilizes probes specifically designed to enhance optical absorption and generate stronger acoustic signals, significantly improving image contrast and enabling deeper tissue penetration. Up-conversion imaging leverages materials capable of converting low-energy NIR excitation into higher-energy visible emissions through nonlinear processes, significantly reducing background autofluorescence and improving imaging clarity.

These enhanced probes expand the applicability and effectiveness of optical imaging techniques across diverse biomedical fields. Fluorescence imaging excels in cellular-level studies, molecular targeting, and intraoperative navigation, providing high-resolution visualization with strong molecular specificity. In clinical use, ICG, an FDA-approved fluorophore, is one of the most commonly used fluorescent probes in NIR-II FMI. Although primarily utilized as an NIR-I dye without inherent tumor-targeting capabilities [97], its emission tail extends into the NIR-II spectrum, making it viable for deeper imaging [298]. Clinical trials utilizing ICG-based targeted probes have demonstrated significant potential for intraoperative tumor navigation, despite limitations such as relatively high false-positive rates (up to 10.5%) due to non-specific accumulation. We summarized all the clinical trials and their fluorescent probes used in NIR-II FMI recently in Table 2, which indicates that NIR-II FMI holds great promise of achieving precise surgery, aiding in tumor resection while preserving functional tissues, and improving the outcomes of clinical treatment. Challenges such as limited fluorescence brightness, low photon utilization efficiency, and heterogeneity in molecular expression levels further underline the need for improved targeting strategies and optimized molecular design.

Table 2 Clinical applications of NIR-II FMI[a)]

Type	Article	Fluorescent probe	Antigen	Imaging target
ClinT	Hu et al. [75]	ICG	–	HCC
ClinT	Zhang et al. [299]	IgG-IRDye800CW	–	HCC
ClinT	Cao et al. [81]	ICG	–	Cystic renal mass
ClinT	Shi et al. [79]	ICG	–	Glioma
ClinT	Mi et al. [82]	ICG	–	Lung cancer
ClinT	Cao et al. [80]	ICG	–	Blood vessels of the brain & glioma
ClinT	Fan et al. [83]	ICG	–	Blood vessels of the foot and ankle
ClinT	Mi et al. [300]	ICG	–	Blood vessels of a giant mediastinal tumor
ClinT	Wu et al. [301]	ICG	–	Blood vessels in microsurgeries
ClinT	Qu et al. [84]	ICG	–	Pelvic autonomic nerves
TissA	Guo et al. [302]	antiCD24-IRDye800CW	CD24	Colorectal cancer
TissA	Guo et al. [303]	2D5-IRDye800CW	CEACAM5	Colorectal cancer
TissA	Tian et al. [304]	$Ab^{B7\text{-}H3}$-800CW	B7-H3	Prostate cancer
TissA	Zeng et al. [305]	B7H3-IRDye800CW	B7-H3	Osteosarcoma
TissA	Wang et al. [89]	$SeCF_3$-IRD800	HDAC6	HCC
TissA	Shen et al. [306]	ICG	–	Glioma
TissA	Xiao et al. [307]	ICG	–	Glioma

(*Continued*)

Type	Article	Fluorescent probe	Antigen	Imaging target
TissA	Xiao et al. [308]	ICG	–	Glioma
TissA	Zhao et al. [309]	mAb-ICG	MCT4	Glioma
TissA	Li et al. [310]	scFv-IRDye800CW	EGFR	Lung cancer
TissA	Chen et al. [88]	TROP2	ICG-SG	Breast cancer
TissA	Keizers et al. [311]	Cetuximab-IRDye800CW	EGFR	PSCC & HNSCC

Notes: ClinT: clinical trial. TissA: tissue analysis. THCC: hepatocellular carcinoma. PSCC: penile squamous cell carcinoma. HNSCC: head and neck squamous cell carcinoma.

Except in FMI, ICG [312] also serves as an efficient PA agent due to its strong absorption properties, facilitating imaging of deep-tissue structures like tumor vasculature. Another FDA-approved dye, methylene blue [313], is also commonly employed in the clinic. In addition, other PA contrast agents and molecular tracers' innovations expand their applications in both preclinical research and clinical diagnostics. Novel nanomaterials, such as nanoparticles, semiconducting polymers, and carbon nanostructures, have been developed to provide enhanced signals with tunable optical properties and biocompatibility. Novel dyes with enhanced capabilities, such as activatable or environment-sensitive dyes [110,314], are being developed to offer higher specificity, improved SNR, and the ability to visualize dynamic biological processes. Meanwhile, novel transgenic proteins with high absorption in the NIR regime are being widely screened, withmany promising candidates identified for future optimization.

Notably, activatable probes, which respond to specific biomolecular cues like enzymatic activity or redox conditions, have emerged as powerful molecular tracers for functional imaging of neural activities and diseases such as cancer and inflammation. Hybrid agents combining diagnostic and therapeutic functions, often referred to as theranostic agents, have also gained attention for their ability to integrate real-time monitoring with treatment. Advances in molecular engineering have enabled the development of targeted tracers that bind to specific biomarkers with high precision, facilitating the detection of early-stage pathologies and providing insights into dynamic biological processes at the molecular and cellular levels. Similar to photoswitchable fluorophores in optical super-resolution microscopy, switchable PA tracers—whether synthesized molecules or transgenic proteins—have demonstrated superior advantages in extracting extremely weak PA signals and have shown notable progress in recent studies [315,316]. These developments have significantly broadened the potential of PA imaging, enabling it to transition from a structural imaging modality to a versatile platform for molecular and functional imaging.

Up-conversion imaging is uniquely suited for applications requiring minimal background interference and superior penetration depth, including deep-tissue neuroscience imaging and super-resolution microscopy. UCNPs have emerged as promising candidates for deep-tissue imaging due to their unique capability to convert NIR excitation into visible emission through multi-photon processes. Advances in nanoparticle surface modification—particularly employing dendrimers and Janus-type dendrimers—have substantially improved UCNP stability, biocompatibility, and labeling performance, enabling imaging depths exceeding 1 mm in brain tissues. The development of up-conversion imaging relies heavily on innovations in UCNPs, which are mainly detailed in Sect. 3.1.3. Furthermore, UCNP-based super-resolution imaging methods, such as UC-STED and UC-SIM, offer substantial advantages, including enhanced resolution, photostability, and reduced excitation intensity requirements, significantly expanding their applicability in biological studies.

Collectively, these advanced material strategies significantly enhance the sensitivity, resolution, and depth capabilities of optical imaging modalities, driving their importance and potential impact in biomedical research and clinical diagnostics.

5. Artificial intelligence-driven strategies

With the rapid advancement of technology, AI has been applied across various fields, leading to significant progress in AI-empowered optical imaging. Optical imaging techniques rely on the interaction of light with biological tissues, extracting crucial information about tissue optical properties, such as the scattering coefficient, absorption coefficient, and chromophore concentrations reconstruct images of tissue structure and function [317]. However, deep-tissue imaging remains a major challenge due to the complex, non-linear nature of photon scattering and the ill-posed inverse problem arising from diffusive photon migration. Traditional computational and mathematical algorithms have been developed to reconstruct parameters and identify anomalies of various geometrical (cracks, cavities, inclusions) and physical (optical, acoustic, elastic) properties. Yet, these classical methods often rely on strong linearization assumptions or require perfectly known boundary conditions, which are rarely achievable in real-world scenarios. To overcome these limitations, AI-driven approaches, particularly generative AI, deep learning, and neural networks, are being employed to enhance computational efficiency in deep-tissue imaging [318]. By leveraging neural networks to perform multiple, arbitrarily-selected transformations, AI models can learn complex mappings between diffuse light signals and underlying tissue properties, effectively bypassing the need for explicit light transport modeling (Figure 13). This AI-driven paradigm not only improves imaging accuracy and depth but also expands the potential of optical imaging in biomedical and clinical applications.

In the last five years, substantial progress has been witnessed in applying AI technology to optical imaging with diffuse light [319]. These advancements focus on improving image resolution, reducing noise, and enhancing the ability to extract quantitative tissue properties from diffuse light data. Deep learning, especially CNNs, has been proven to be effective in improving image reconstruction, reducing noise, and boosting resolution in optical

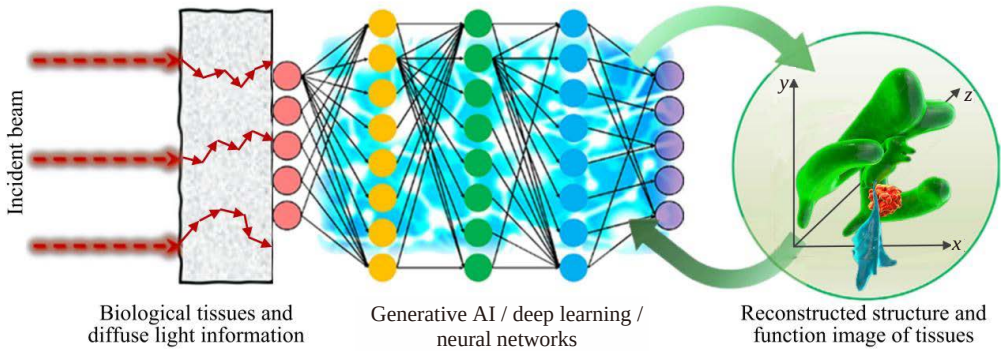


Figure 13 AI for optical imaging with diffuse light. Information from quantitative images with diffuse light is fused to extract multivariate biophysical features of tissues, which are fed into a fully connected neural network.

imaging [320]. Through training on large datasets, deep learning models learn to map scattered light data to underlying tissue properties, such as tumors and blood vessels. This results in images with better clarity and accuracy compared to conventional methods. Moreover, generative AI models like GANs further improve this by generating high-resolution images from lower-resolution data [321]. The generator network creates synthetic images, while the discriminator evaluates their realism, ultimately generating images that closely resemble true tissue structures, even from noisy data. In addition, hybrid models integrate the data-driven strengths of deep learning with the physics of light propagation in tissues to enhance the overall performance of optical imaging [322]. These models enhance image reconstruction by leveraging both known light scattering principles and data-driven learning, improving the accuracy and robustness of optical imaging systems and capturing fine tissue details that would otherwise be difficult to detect. Another breakthrough lies in the integration of deep learning into real-time imaging systems [323]. Traditionally, bio-optical imaging with diffuse light required offline processing, which limited its use in dynamic, time-sensitive clinical settings. Now, learning models can process and reconstruct images in real-time, enabling continuous monitoring of processes like brain activity during surgery, tissue oxygenation during cancer treatment, or providing surgeons with immediate feedback for intraoperative guidance.

(1) Challenges

Despite the advances made in integrating AI into optical imaging with diffuse light, several limitations remain [324]. One principal limitation is the need for large, high-quality datasets for learning models. The performance of these models hinges largely on the quality of the data, and the acquisition of sufficient labeled data can be both time-consuming and costly. Additionally, learning models may struggle to generalize across diverse tissue types, leading to reduced performance when applied to new data. Another challenge is the interpretability of AI models. Learning models, especially CNNs and GANs, are often considered "black boxes", making it difficult to understand how they make decisions. In biomedical imaging, clinicians must trust the output but also understand how the model arrived at its conclusions. This lack of transparency can hinder the adoption of AI-based systems in clinical practice, where interpretability is critical for patient safety and clinician trust. The computational requirement of deep learning also poses barriers to clinical use. Training models require substantial computational resources, and real-time processing still demands powerful platforms. While cloud computing and specialized hardware are addressing some of these concerns, the computational needs may not always be feasible in resource-limited settings.

(2) Future directions

Several strategies are emerging to address the above-mentioned challenges [324,325]. One promising approach is the use of synthetic data and data augmentation techniques, which can increase the diversity and volume of training datasets. By generating synthetic data that mimics real-world conditions, AI models can be trained on a wider variety of tissue types, improving their robustness. There is also growing interest in developing explainable AI models that provide insights into the decision-making process, thereby helping clinicians better understand the model's outputs and fostering trust in its use. Another promising direction is the integration of edge computing and cloud-based solutions to address the computational demands of real-time deep tissue optical imaging. Offloading tasks to the cloud or edge devices can accelerate image reconstruction and render these technologies more accessible for imaging applications. These solutions could also facilitate the creation of portable, easy-to-use devices, extending the reach of deep tissue optical imaging to point-of-care settings.

Looking ahead, the synergy between AI technology and optical imaging with diffuse light is poised to drive transformative changes in biomedical diagnostics and treatment [326]. In the short term, we can anticipate improvements in integrating AI models into existing optical imaging systems like NIR-II imaging, PAI, and other imaging with diffuse light, enhancing their accuracy and resolution for clinical applications. In the medium term, hybrid imaging systems combining optical imaging with other modalities like MRI, CT, or ultrasound are expected to become more prevalent. These systems will leverage AI technology to provide more comprehensive and detailed images of tissues, improving diagnostic capabilities. In the long term, AI-driven optical imaging may play a critical role in personalized medicine. Real-time monitoring of tissue properties and responses to treatment could enable highly individualized therapeutic strategies, particularly in oncology and chronic disease management. In conclusion, the AI technology has significantly enhanced the capabilities of biomedical optical imaging with diffuse light, overcoming traditional limitations related to image quality and reconstruction.

6. Discussion and perspectives

In Table 3, we summarize the key aspects of the technologies discussed in this review. Clearly, state-of-the-art technologies have made significant advancements in various areas of deep-tissue optical imaging, leading to promising clinical and biological applications. For example, OCT has become a standard tool in ophthalmology and intravascular imaging. At greater depths, the power of coherence gating enables OCT to image through highly scattering media, such as the *in-vivo* brain [327] and human skin [328]. Multiphoton imaging has become a widely used standard tool in neuroscience, allowing for dynamic, 3D visualization of cellular-level structures and functions at depths beyond 1 mm [329]. Meanwhile, imaging with diffuse light has seen a recent surge in clinical applications, particularly where centimeter-deep penetration is critical for intraoperative tumor delineation, non-invasive functional imaging of the human cortex [330], and tumor diagnosis and screening in superficial organs [120].

However, further improving imaging depth and quality is becoming an increasingly difficult challenge, making it essential to understand the limitations of the current technologies. In biological tissues, the typical length scale for the scattering mean free path in the NIR range is approximately 0.1 mm, corresponding to a scattering coefficient of $\mu_s = 10\ \mathrm{mm}^{-1}$, which is the inverse of the scattering length L_s. At a depth of 1 mm, photons are scattered on average 10 times. The probability that a photon remains unscattered can be estimated as $e^{-\mu_s z}$ (where z = 1 mm), yielding roughly 45 parts per million (ppm). As the ballistic component of light decays exponentially with increasing depth, it becomes negligible beyond 1 mm, effectively limiting the penetration depth of ballistic imaging to the millimeter range. Light penetration is also affected by absorption, characterized by the absorption coefficient μ_a, which is the inverse of the absorption length L_a. The total attenuation results from both scattering and absorption, with the total attenuation coefficient given by $\mu = \mu_s + \mu_a$. The corresponding attenuation length is expressed as:

$$L = \left(\frac{1}{L_s} + \frac{1}{L_a}\right)^{-1}. \tag{4}$$

In many biological tissues, such as the mouse brain, the attenuation length increases monotonically between 650 nm and 1,350 nm, reaching a maximum around 1,700 nm [331]. This wavelength dependence explains why techniques such as 3P absorption fluorescence imaging and NIR-II imaging provide high-contrast, high-resolution imaging in deep tissues.

In the optically diffusive regime, techniques like FMI and fNIRS leverage scattered light for imaging at depths of millimeters to a few centimeters, without the need for wavefront manipulation. These methods are valued for their simplicity and robustness, leading to their clinical adoption. When using diffuse light for imaging, the penetration depth is significantly influenced by the effective attenuation coefficient derived from light transport theory:

$$\mu_{\mathrm{eff}} = \sqrt{3\mu_a(\mu_a + \mu'_s)}, \tag{5}$$

where $\mu'_s = \mu_s(1-g)$ is the reduced scattering coefficient. Accordingly, the wavelength range from 650 nm to 1,100 nm offers superior penetration depth, while imaging at a wavelength above 1,200 nm may provide higher resolution at the expense of reduced light penetration and sensitivity for FMI [332]. In general, biological tissues exhibit the best "optical window" for deep penetration, roughly between 650–1,350 nm, where both absorption (e.g., by blood hemoglobin and water) and scattering are relatively low. In this window, absorption by hemoglobin drops off in the red/NIR, and water absorption remains low, while scattering also decreases with longer wavelength. It should be noted that definitions of the optical spectral windows can vary; some sources define the NIR-II window as 900 nm to 1,880 nm [333], while others consider the ranges 1,230 nm to 1,330 nm [332], or 1,000 nm to 3,000 nm [334] as the NIR-II window.

Despite deep penetration, diffuse light imaging techniques face resolution challenges. The theoretical resolution limit scales with penetration depth (D) as $D/5$ [335]. Additionally, acquiring 2D intensity maps integrates light along the depth direction, reducing lateral resolution and eliminating depth resolution. Short exposure times required for video-rate operation, coupled with low concentrations of targeted agents (sub-nmol/L to sub-μmol/L), pose challenges for sensitivity and accuracy [332]. Nevertheless, diffuse light imaging is gaining increasing popularity due to its ease of use and inherent safety. Recent applications in intraoperative and brain imaging have shown promising results, further highlighting its potential in clinical settings.

PAI, which includes acoustic-resolution PAM and PACT, is a powerful modality that also utilizes diffuse light for deep-tissue imaging. In PAI, image contrast is provided by tissue absorption of scattered light, while image resolution is determined by ultrasound diffraction, yielding relatively high resolution on the order of $D/200$, as defined by ultrasound attenuation [108]. Although the light-to-sound conversion in PAI is lossy, its sensitivity to fluorescent molecular probes is comparable to that of fluorescence imaging [336]. Key advantages of PAI include its inherent compatibility with clinical US imaging, high sensitivity to optical molecular probes and blood oxygenation, high resolution at deeper depths, and speckle-free image formation. However, several challenges hinder its broader clinical application, including limited penetration in comparison to ultrasound imaging, the need for ultrasound coupling, difficulties in spectral unmixing and quantitative analysis, and image artifacts due to suboptimal signal detection and reconstruction. These challenges are being addressed through the development of advanced imaging hardware, tailored molecular probes, and novel reconstruction algorithms, aiming to fully realize the clinical potential of PAI.

Evidently, the limit of deep-tissue optical imaging is determined by light absorption and scattering. Beyond a few millimeters, the ballistic component of light is extinguished, setting the limit for all optical imaging technologies that rely on ballistic photons. Beyond a few centimeters, even the scattered component of light becomes negligibly small, which sets a hard limit to diffuse light imaging. In the diffusive regime, the resolution achievable degrades with depth, with a record set by PAI of about 1/200 of the penetration depth. This means that at a depth of 1 centimeter, the resolution limit is on the order of 50 micrometers at best, and a diffraction-limited resolution voxel contains at least a few hundred cells.

Apart from those, adaptive and computational optics have become more popular in the biomedical field. As light propagates deeper into tissue, its wavefront coherence degrades due to scattering and aberrations, making high-resolution focusing increasingly challenging. AO provides a practical solution by correcting these wavefront distortions, thereby restoring image clarity at depth. For example, with the advancement of real-time wavefront correction, AO-OCT is capable of imaging individual photoreceptors in the living human eye using purely intrinsic tissue contrast [337,338]. However, AO is fundamentally limited by the increase of wavefront distortion with imaging depth. As light penetrates deeper, it undergoes more scattering events and traverses RI inhomogeneities, causing cumulative wavefront aberrations that grow in magnitude and complexity; thicker tissue thus produces significantly more aberration and speckle, degrading image quality [339]. AO can only compensate these aberrations by applying an equal-and-opposite phase correction—it cannot actually reduce or eliminate the underlying scattering processes, so photons that are scattered out of the collection path remain lost. Moreover, the corrective wavefront pattern required becomes increasingly intricate with depth, reflecting higher-spatial-frequency distortions: effectively, the number of degrees of freedom needed to correct the wavefront (the number of aberration "modes") rises with each additional scattering layer. At such depths, one also encounters diminishing temporal stability: the tissue's micro-movements (e.g., blood flow) cause the wavefront to fluctuate faster [161], and the speckle decorrelation time shortens—dropping from the order of milliseconds at ~1 mm depth to <1 ms beyond ~2–3 mm *in vivo* [340]. This means any AO correction must be applied extremely quickly before the wavefront changes. Another consequence of multiple scattering is a shrinking isoplanatic patch—the region over which a given AO correction remains valid. Deeper in the tissue, aberrations vary so rapidly across space that an optimized correction at one location only improves a small surrounding region (on the order of tens of micrometers laterally at sub-millimeter depths in the mouse cortex [339], and as low as a few microns in very turbid tissue like the skull [341]). In general, the isoplanatic patch size decreases with greater imaging depth and with higher-order corrections (more modes) applied, and is typically much smaller in the lateral plane than along the axial direction [38]. A useful quantitative benchmark is the transport mean free path,

$$L^* = \frac{L_s}{1-g}, \tag{6}$$

where g is the anisotropy factor, which is typically in the range of 0.85 to 0.98 for many tissue types in the NIR range. In essence, L^* is the characteristic depth beyond which light propagation becomes diffusive, for biological tissues, L^* is roughly an order of magnitude larger than L_s (on the order of ~1 mm in the mouse brain for NIR wavelengths). At imaging depths exceeding L^*, nearly all photons have been multiply scattered and have lost memory of their original paths, so conventional AO can no longer maintain a diffraction-limited focus. Theoretically, one could attempt to correct aberrations even in this regime by measuring and inverting the full scattering phase distortion (e.g., via time-reversed WFS), but this would entail an extraordinarily large number of correction modes and ultrafast updates, which is very challenging and is the focus of optical WFS. Consequently, AO is very effective for improving imaging in mouse brain tissue up to a depth of a few hundred microns (compensating lower-order aberrations and forward scattering), and with advanced techniques (such as 3P excitation with indirect wavefront sensing and motion gating) it has been extended to ~1.4 mm *in vivo* [38], approaching the transport mean free path limit. Beyond this ~1–2 mm regime, however, AO yields rapidly diminishing returns, marking a theoretical and practical barrier where alternativestrategies are required to further improve deep imaging.

Beyond the diffusion limit, where ballistic photons are largely extinguished, scattered light can still be harnessed for imaging. WFS holds a distinctive role by actively manipulating the phase of incident light to achieve constructive interference and focusing within highly scattering media. WFS enables optical focusing deep inside diffusive biological tissue by engineering the input wavefront so that scattered light interferes constructively at a target point. Through techniques like OPC (time-reversed wavefront playback), iterative feedback optimization, or transmission-matrix inversion, one can determine the phase pattern that refocuses multiply scattered photons into a tight spot. These methods use the scattered light itself to form a focus, yielding a high PBR—the intensity of the focus peak relative to the speckle background. In ideal static media, PBR can reach hundreds or more (proportional to the number of controlled modes), whereas in practice, tissue motion noise and partial wavefront control often limit PBR to lower values [342]. The speckled background follows Rayleigh statistics (exponential intensity distribution), so a high PBR is crucial for the focus to stand out above random intensity graininess. A key requirement for focusing inside tissue (*in vivo*) is a guide star at the intended focus to provide feedback or a phase reference [343,344]. Various guide stars have been explored; for example, an attractive noninvasive approach is to use an ultrasound-defined guide star [345]. Factors including complexity of the setup, need for an effective guide star, and fast tissue decorrelation have so far made *in-vivo* WFS a technical *tour de force*. Recent breakthroughs have illuminated the *in-vivo* application of WFS technologies. For example, transcranial 2P imaging in mice has been enhanced with multi-patch wavefront corrections switched at 40 kHz, enabling the simultaneous imaging of multiple neurons [346].

To resume the optically-defined image resolution in the diffusive regime, techniques such as fiberscopes, tissue clearing, and biosafety contrast agents can be applied. Fiberscopes can help deliver high-quality images from deeper layers of tissue or from body cavities, at the expense of minimal invasiveness and a limited FOV. With these emerging technologies, the ability to perform deep-tissue imaging with optically defined resolution opens up new possibilities for studying organ-wide structures and biodistributions, deep-tissue intravital imaging, and real-time monitoring during microsurgeries. Tissue clearing decreases the turbidity of biological tissue by removing substances such as lipids to reduce refractive-index inhomogeneities. Both *ex-vivo* and, more recently, *in-vivo* tissues can be rendered transparent, allowing light penetration to unprecedented depths with optically-defined resolution [286,347]. Additionally, novel imaging probes, such as those used in up-conversion imaging, NIR-II

Table 3 The key aspects of summary in deep-tissue optical technologies

Technique		Principle	Resolution	Penetration depth	Imaging efficiency	Maturity	Applications	Challenges	Future advancements
Ballistic light imaging	OCT	Interferometry	1–3 μm axial resolution (visible light or ultra-broadband sources) [15]	1–3 mm (limited by scattering) [14]	High speed (SS-OCT: up to 9.4 MHz A-line rate) [18]	Clinical	Mainly ophthalmology and dermatology; increasingly used in cardiovascular, neurovascular	Limited penetration depth due to tissue scattering	AI integration; anatomical minimally invasive imaging
	MPM	Two-photon/three-photon absorption	Achieves nanoscale super-resolution with STED/SIM [46,47]	~1.4 mm (with 3PF) [38]	Moderate speed (achieves kHz-level frame rates via FACED cavity or grating spectral separation [39,40]	Preclinical/clinical	3D neuronal imaging [37]; cell migration tracking [44]; super-resolution [46,47]	Balancing photon-induced tissue damage and photon budget; signal attenuation due to deep-layer scattering	Combined with AI tools; multimodal integration (e.g., OCT/PAI)
	Up-conversion	Anti-Stokes luminescence	Nanoscale (super-resolution: 50–172 nm [73,348]); limited by PSF distortion in deep tissue [70]	2P up-conversion: up to 2 mm in thick tissue[58]; 3P/4P up-conversion: 800 μm in phantom [60]	Slow (scanning-based); faster with super-resolution (UC-PA) [68,69]	Tissue experiments/preclinical	Deep-tissue vasculature mapping [56,57]; optogenetics [58]; skin penetration studies [59]	Low quantum yield; nanoparticle delivery and biocompatibility issues; deep-layer PSF distortion	Higher-order nonlinear excitation (4-photon/5-photon); super-resolution microscopy
Diffuse light imaging	NIR-II imaging	NIR-II light (1,000–1,700 nm) excites fluorescent probes	micron-scale resolution: ~50μm [75]	Centimeters imaging depth; Up to ~3 mm depth with micron-scale resolution [75]	Real-time intraoperative imaging [75]; slow for 3D FMT [349]	Clinical	Tumor resection guidance [75]; vascular/nerve visualization [80,84]; 3D tomography [349]	Non-specific probes (e.g., ICG); tumor heterogeneity; lack of 3D data	Fluorescence molecular tomography (FMT); depth-resolved localization
	fNIRS	Measures HbO/HbR absorption changes	Spatial resolution limited by photon scattering	Limited to 1–2 cm due to high scattering, deeper with diffuse correlation spectroscopy [275,278,279]	Real-time (10–100 Hz) [99]; limited by motion artifacts [106]	Clinical	Brain functional mapping [101]; neurodegenerative disease monitoring [104]; BCI [105]	Low spatial resolution; motion/physiological noise; data fusion standardization	Leverage AI algorithms; large-scale multi-center trials; combine multimodal imaging
	PAI	Photoacoustic (PA) effect	Microscopic (OR-PAM: 1–10 μm [116]); mesoscopic (AR-PAM: 10–100 μm [350]); macroscopic (PACT: 100–500 μm [122])	Several cm (clinical PACT); limited by light penetration and ultrasound detection [121]	Real-time 3D PACT (10–50 fps) [122]; OR-PAM slower due to raster scanning	Preclinical/clinical	Vascular imaging [116]; cancer diagnostics [314]; neurovascular coupling [116]	Identified clinical breakthrough needed; development of robust PA molecular tracers; high system costs and lack of standardization	Robust PA molecular tracers; cost-effective PA system
AO	AO	Actively measure and correct aberrations	Near-diffraction limit [140]	With MPM: 1.4 mm (cortical dendrites) [140] standalone AO: ~800 μm (limited by guide stars) [133]	Real-time correction possible but complex	Preclinical/clinical	Neuroscience (dendrites, spinal cord imaging) [137,140]	High cost and system complexity; speed requirement for dynamic samples; dependency on guide stars and scattering interference	Low-cost integrated AO modules; AI-driven real-time correction; multimodal imaging
Wavefront engineering	OPC	Time-reversal symmetry	Limited by guide star size [171]	Centimeter-scale (through living mouse tissue) [167]	Ultrafast ~340 ns [167]	Tissue experiments	Deep focusing with ultrasound guide stars [169,170]; dynamic scattering control	Speckle decorrelation (ms timescale); low SNR of ultrasound guide stars	High-efficiency guide stars; AI-enhanced dynamic compensation

(*Continued*)

Technique		Principle	Resolution	Penetration depth	Imaging efficiency	Maturity	Applications	Challenges	Future advancements
Other methodologies	iWFS	Feedback-driven iterative optimization	Micron-scale (limited by mode number vs. speed trade-off) [174]	Millimeter to centimeter-scale [173]	Slow (requires ~10^6 modes; limited by algorithm convergence) [174]	Tissue experiments	Endoscopic imaging [184]; multi-point focusing; neural activity monitoring	Speed-mode number trade-off; dynamic scattering; non-invasive feedback	AI-accelerated algorithms; multi-DOF modulators
	TM/RM	Linear matrix model for inverse wavefront calculation	Sub-micron (depends on TM calibration accuracy) [201]	Millimeter-scale (demonstrated in phantoms/static media) [201]	Slow (hours for TM calibration; 10^6×10^6 modes) [188-190]	Phantom/static tissue experiments	Multimode fiber imaging [201]; vectorial light control [197,198]; scattering media imaging [199]	Time-consuming TM calibration; sensitivity to environmental noise	Compressive sampling for faster calibration; machine learning for robustness
	Fiber-based probe: MMFs	Multimode fiber with WFS for minimally invasive high-resolution imaging	Lateral: 1.5 μm; Axial: 12.7 μm (digital focusing) [209]	Deep brain regions via flexible insertion (e.g., neuronal imaging) [221]	High-speed (15.4 million fps with neural networks) [211]	Preclinical	Endoscopy; 3D imaging; SRS/CARS [217,218]	Small field of view (FOV) ~100 μm; dynamic bending degrades transmission matrix; low axial resolution	AI-accelerated image reconstruction; multimodal data fusion; minimally invasive clinical navigation
	Digital holography	Captures the phase information of scattered light	Subcellular (phase-sensitive; limited by scattering correction) [228,233]	Near millimeter-scale (0.5 mm maximum thickness through milk) [233]	Moderate (real-time phase-shifting holography [236]; slow for iterative corrections [227])	Static tissue experiments	3D tissue morphology [233]; wavefront correction [230]; fluorescence imaging [147,232]	Wavefront distortion from static/dynamic scattering; limited depth *in vivo*	Multimodal integration; deep learning for noise suppression
	Speckle contrast imaging	Analyzes speckle contrast to map blood flow	Micron-scale (limited by speckle size and motion artifacts) [252,253,267]	~1–2 mm (improved to ~5 mm with NIR and diffuse correlation) [269]	Real-time (RSSI: single-shot [267]; DLSI: 20,000 fps [266])	Preclinical/clinical	Blood flow [246]; intraoperative monitoring [238-243]; wound healing [260,261]	Shallow penetration; relative flow speed; motion artifacts	Absolute flow calibration; portable devices for point-of-care
Chemical and material innovations	TOC	Reduces scattering via refractive index (RI) matching using optical clearing agents (OCAs)	Enables super-resolution imaging (e.g., SeeDB2 for deep tissues) and single-cell resolution *in vivo* (e.g., RUSH3D for immune cell dynamics) [281,289]	*Ex vivo*: whole organs (e.g., SOLID for whole-brain mapping) [285]. In vivo: brain cortex, spinal cord, and skin [290]	Time-consuming (hours to weeks) due to OCA diffusion	Tissue experiments	Whole-brain mapping [285]; tumor tracking [291]; skin vasculature imaging [286]	*In-vivo* OCA delivery; manual protocols requiring expertise; image degradation in large samples	Non-toxic/fast OCAs for clinical use; integration with AI/automation; phototherapy optimization
	Contrast agents and molecular probes	Maximize fluorescence quantum yield; enhance optical absorption; convert low-energy NIR excitation into higher-energy visible emissions	From nanoscale (MPM, UC imaging) to micron-scale (NIR-II Imaging, PACT)	1 mm to Several cm	Moderate speed in high resolution; real time in relatively low resolution	Cell/tissue/preclinical/clinical	Tumor navigation [96]; precise surgery [75]; tumor vasculature visualization [300] [80]; real-time monitoring with treatment [315]	Limited fluorescence brightness, low photon utilization efficiency, and heterogeneity in molecular expression; biosafety	Robust molecular tracers; more safety; precise tracking of specific functions
AI-driven strategies	Generative AI	Neural networks (CNNs, GANs) learn mappings	Enhanced resolution via super-resolution GANs [321]	Depth-agnostic (depends on coupled optical techniques, e.g., NIR-II, PAI) [326]	Real-time processing with edge/cloud computing [323]; training computationally intensive [324]	Phantom/static tissue experiments	Tumor detection [320]; real-time brain activity monitoring [323]; hybrid imaging [322]	Data scarcity/quality; black-box interpretability; computational cost	Synthetic data augmentation; explainable AI; hybrid physics-DL models

fluorescence imaging, and PA imaging, are crucial for advancing next-generation deep tissue imaging technologies.

AI offers unprecedented capabilities in solving complex nonlinear problems and accelerating signal processing and computation. For instance, AI can leverage extensive datasets to incorporate complex prior information, enabling more accurate image reconstruction in challenging conditions such as high noise, limited sampling, or restricted frequency passbands. However, caution is necessary to avoid the risk of hallucinations in AI-generated outputs, which should always be validated against ground truth—something that is particularly challenging to obtain in deep-tissue imaging. Nevertheless, there is no doubt that, when applied correctly, AI will greatly benefit nearly all deep-tissue imaging technologies discussed in this review.

7. Summary

Deep-tissue optics (especially for imaging) stands at the forefront of biomedical innovation, bridging the gap between microscopic resolution and macroscopic penetration depth. This review synthesizes cutting-edge advancements across three pivotal domains: physical modalities, chemical strategies, and computational paradigms.

Physical modalities such as OCT and MPM have revolutionized high-resolution imaging, enabling cellular-level visualization *in vivo*. Meanwhile, diffuse light techniques like NIR-II fluorescence and PAI leverage scattered photons for centimeter-depth structural and functional mapping. Chemical innovations, including TOC agents and molecular probes, address scattering and absorption at their source, rendering tissues transparent and enhancing contrast. Computational breakthroughs—AO, wavefront engineering, and AI-driven reconstruction—correct aberrations, suppress noise, and decode complex photon-tissue interactions in real time.

Clinically, these technologies are transforming diagnostics and interventions. OCT remains the gold standard in ophthalmology and dermatology, while NIR-II fluorescence guides precision tumor resection. AO enables synapse-level brain imaging, and PAI provides functional insights into tumor metabolism. Yet challenges persist: limited penetration beyond the transport mean free path, phototoxicity risks, and the need for biocompatible nanomaterials.

The future lies in multimodal integration (e.g., OCT-PAI hybrids), AI-enhanced theranostics, and minimally invasive probes such as MMFs. Emerging paradigms like digital holography and iWFS promise to overcome dynamic scattering barriers. Collaborative efforts across optics, materials science, and computational biology will drive scalable solutions for clinical translation, ultimately advancing precision medicine and unlocking uncharted biological phenomena.

In conclusion, this review not only maps the current landscape of deep-tissue optics but also charts a roadmap for next-generation technologies poised to redefine biomedical imaging and therapeutic interventions.

Authors' contributions Wu Yuan, Di Mei, and Xingde Li offered insights on coherence/time gating techniques. Kenneth K. Y. Wong and Xin Dong provided expertise on multiphoton technics (MPM). Qiuqiang Zhan and Rui Pu contributed knowledge on up-conversion imaging. Zhenhua Hu and Jie Tian focused on NIR-II FMI. Daifa Wang and Di Wu shared their expertise on fNIRS. Cheng Ma and Changhui Li discussed PAI. Qinrong Zhang and Liulin He provided insights on AO. Yuecheng Shen and Shian Zhang explored OPC. Jiamiao Yang and Chunxu Ding contributed to the understanding of iWFS. Lei Gong and Jinghan Zhuang focused on TM techniques. Qing Yang and Quanzhi Li discussed fiber-based probe technologies. Liangcai Cao and Jiachen Wu provided insights on digital holography. Pengcheng Li and Jiachi Hong explored speckle correlation imaging. Dan Zhu, Valery V. Tuchin, and Tingting Yu provided insights on tissue clearing methodologies. Chao Zuo and Cheng Ma contributed insights into AI-derived optical imaging. Weiran Pang, Tianting Zhong, Xiazi Huang, Yingying Zhou, Honglin Liu, and Xuyu Zhang contributed to the preparation of introduction and summary. Yize Gao and Cheng Ma contributed to the preparation of discussion and perspectives section. Weiran Pang, Tianting Zhong, Yize Gao, Xiazi Huang, and Puxiang Lai coordinated the organization of writings and the consolidation of the whole manuscript. Cheng Ma and Puxiang Lai supervised the whole process of manuscript preparation. All authors reviewed the initial draft and provided feedback for revisions.

Compliance and ethics The author(s) declare that they have no conflict of interest.

Funding This work was supported by the National Natural Science Foundation of China (NSFC) (81930048, 82330061, 62335008, 62405096, 12474318, 62375096, 61860206009, 32361133552, 82361138569, 62275121, 12204239, 62405096, T2293750, T2293751), the Science, Technology, and Innovation Commission (STIC) of Shenzhen Municipality (SGDX20220530111005039), the Innovation and Technology Fund (ITF) of Hong Kong SAR (ITS/252/23), Research Grants Council of the Hong Kong Special Administrative Region Government (15217721, 15125724, HKU 17212824, HKU 17210522, HKU C7074-21G, HKU R7003-21, and HKU 17205321), Shenzhen Science Technology and Innovation Commission (SGDX20220530111403022, JCYJ20220818100202005), Guangdong Basic and Applied Basic Research Foundation (2019BT02X105, 2023B1515040018, 2023A1515110427, 2025A1515011201), the National Key Research and Development Program of China (2023YFC2411700), the Russian Science Foundation (24-44-00082), the Major Science and Technology Special Program of Jiangsu Province (BG2024025), China Postdoctoral Science Foundation (2024M750977), and Postdoctoral Fellowship Program of CPSF (GZB20240234).

References

1. Ntziachristos V, Ripoll J, Wang LV, Weissleder R. Looking and listening to light: The evolution of whole-body photonic imaging. Nat Biotechnol. 2005; 23: 313–20.
2. Yun SH, Kwok SJJ. Light in diagnosis, therapy and surgery. Nat Biomed Eng. 2017; 1: 8.
3. Litvinova KS, Rafailov IE, Dunaev AV, Sokolovski SG, Rafailov EU. Non-invasive biomedical research and diagnostics enabled by innovative compact lasers. Prog Quantum Electron. 2017; 56: 1–14.
4. Ran C, Pu K. Molecularly generated light and its biomedical applications. Angew Chem Int Ed. 2024; 63: e202314468.
5. Lai PX, Zhao Q, Zhou YY, Cheng SF, Woo CM, Li HH, et al. Deep-tissue optics: Technological development and applications. Chin J Lasers. 2024; 51(1): 0107003.
6. Huang SH, Irawati N, Chien YF, Lin JY, Tsai YH, Wang PY, et al. Optical volumetric brain imaging: Speed, depth, and resolution enhancement. J Phys D: Appl Phys. 2021; 54: 323002.
7. Zhou ZC, Gordon-Fennell A, Piantadosi SC, Ji N, Smith SL, Bruchas MR, et al. Deep-brain optical recording of neural dynamics during behavior. Neuron. 2023; 111: 3716–38.
8. Andreou C, Weissleder R, Kircher MF. Multiplexed imaging in oncology. Nat Biomed Eng. 2022; 6: 527–40.
9. Wang LV, Wu HI. Biomedical optics, principles and imaging. Hoboken: John Wiley & Sons; 2007.
10. Huang D, Swanson EA, Lin CP, Schuman JS, Stinson WG, Chang W, et al. Optical coherence tomography. Science. 1991; 254: 1178–81.
11. Drexler W, Fujimoto JG. Optical coherence tomography: Technology and applications. Berlin, Heidelberg: Springer; 2008.
12. Spaide RF, Fujimoto JG, Waheed NK, Sadda SR, Staurenghi G. Optical coherence tomography angiography. Prog Retin Eye Res. 2018; 64: 1–55.
13. Ge X, Chen S, Chen S, Liu L. High resolution optical coherence tomography. J Lightwave Technol. 2021; 39: 3824–35.
14. Xu C, Zhang T, Abbasi SA, Liu P, Yan BP, Ng SHC, et al. Ultrathin visible-light OCT endomicroscopy for *in vivo* ultrahigh-resolution neuroimaging in deep brain. APL Photonics. 2024; 9: 110804.
15. Yuan W, Chen D, Sarabia-Estrada R, Guerrero-Cázares H, Li D, Quiñones-Hinojosa A, et al. Theranostic OCT microneedle for fast ultrahigh-resolution deep-brain imaging and efficient laser ablation *in vivo*. Sci Adv. 2020; 6:

eaaz9664.
16. Zhang T, Yuan S, Xu C, Liu P, Chang HC, Ng SHC, et al. PneumaOCT: Pneumatic optical coherence tomography endoscopy for targeted distortion-free imaging in tortuous and narrow internal lumens. Sci Adv. 2024; 10: eadp3145.
17. Seong D, Jeon D, Wijesinghe RE, Park K, Kim H, Lee E, et al. Ultrahigh-speed spectral-domain optical coherence tomography up to 1-MHz a-scan rate using space–time-division multiplexing. IEEE Trans Instrum Meas. 2021; 70: 1–8.
18. Kim TS, Joo J, Shin I, Shin P, Kang WJ, Vakoc BJ, et al. 9.4 MHz A-line rate optical coherence tomography at 1300 nm using a wavelength-swept laser based on stretched-pulse active mode-locking. Sci Rep. 2020; 10: 9328.
19. Hee MR, Izatt JA, Swanson EA, Huang D, Schuman JS, Lin CP, et al. Optical coherence tomography of the human retina. Arch Ophthalmol. 1995; 113: 325.
20. Gora M, Karnowski K, Szkulmowski M, Kaluzny BJ, Huber R, Kowalczyk A, et al. Ultra high-speed swept source OCT imaging of the anterior segment of human eye at 200 kHz with adjustable imaging range. Opt Express. 2009; 17: 14880.
21. Bouma BE, de Boer JF, Huang D, Jang IK, Yonetsu T, Leggett CL, et al., Optical coherence tomography. Nat Rev Method Prime. 2022; 2: 79.
22. Tsokolas G, Tsaousis KT, Diakonis VF, Matsou A, Tyradellis S. Optical coherence tomography angiography in neurodegenerative diseases: A review. Eye Brain. 2020; 12: 73–87.
23. You QS, Guo Y, Wang J, Wei X, Camino A, Zang P, et al. Detection of clinically unsuspected retinal neovascularization with wide-field optical coherence tomography angiography. Retina. 2020; 40: 891–7.
24. Saxer CE, de Boer JF, Park BH, Zhao Y, Chen Z, Nelson JS. High-speed fiber–based polarization-sensitive optical coherence tomography of *in vivo* human skin. Opt Lett. 2000; 25: 1355.
25. Zhao Y, Chen Z, Saxer C, Xiang S, de Boer JF, Nelson JS. Phase-resolved optical coherence tomography and optical Doppler tomography for imaging blood flow in human skin with fast scanning speed and high velocity sensitivity. Opt Lett. 2000; 25: 114–6.
26. Tsai TH, Ahsen OO, Lee HC, Liang K, Figueiredo M, Tao YK, et al. Endoscopic optical coherence angiography enables 3-dimensional visualization of subsurface microvasculature. Gastroenterology. 2014; 147: 1219–21.
27. Bouma BE, Tearney GJ, Compton CC, Nishioka NS. High-resolution imaging of the human esophagus and stomach *in vivo* using optical coherence tomography. Gastrointest Endosc. 2000; 51: 467–74.
28. Nguyen TH, Thrift AP, George R, Rosen DG, El-Serag HB, Ketwaroo GA. Prevalence and predictors of missed dysplasia on index Barrett's esophagus diagnosing endoscopy in a veteran population. Clin Gastroenterol Hepatol. 2022; 20: e876–89.
29. Evans JA, Poneros JM, Bouma BE, Bressner J, Halpern EF, Shishkov M, et al. Optical coherence tomography to identify intramucosal carcinoma and high-grade dysplasia in Barrett's esophagus. Clin Gastroenterol Hepatol. 2006; 4: 38–43.
30. Chen Y, Ding M, Guan WJ, Wang W, Luo WZ, Zhong CH, et al. Validation of human small airway measurements using endobronchial optical coherence tomography. Respir Med. 2015; 109: 1446–53.
31. Coxson HO, Quiney B, Sin DD, Xing L, McWilliams AM, Mayo JR, et al. Airway wall thickness assessed using computed tomography and optical coherence tomography. Am J Respir Crit Care Med. 2008; 177: 1201–6.
32. Testoni PA, Mariani A, Mangiavillano B, Albarello L, Arcidiacono PG, Masci E, et al. Main pancreatic duct, common bile duct and sphincter of Oddi structure visualized by optical coherence tomography: An *ex vivo* study compared with histology. Dig Liver Dis. 2006; 38: 409–14.
33. Corral JE, Mousa OY, Krishna M, Levink IJM, Pursell KR, Afsh M, et al. Volumetric laser endomicroscopy in the biliary and pancreatic ducts: A feasibility study with histological correlation. Endoscopy. 2018; 50: 1089–94.
34. Untracht GR, Chen M, Wijesinghe P, Mas J, Yura HT, Marti D, et al. Spatially offset optical coherence tomography: Leveraging multiple scattering for high-contrast imaging at depth in turbid media. Sci Adv. 2023; 9: eadh5435.
35. Zhao J, Winetraub Y, Du L, Van Vleck A, Ichimura K, Huang C, et al. Flexible method for generating needle-shaped beams and its application in optical coherence tomography. Optica. 2022; 9: 859.
36. Xu C, Nedergaard M, Fowell DJ, Friedl P, Ji N. Multiphoton fluorescence microscopy for *in vivo* imaging. Cell. 2024; 187: 4458–87.
37. He H, Tang H, Zhou M, Lai H, Qiao T, Ren YX, et al. Deep-tissue two-photon microscopy with a frequency-doubled all-fiber mode-locked laser at 937 nm. Adv Photon Nexus. 2022; 1: 026001.
38. Streich L, Boffi JC, Wang L, Alhalaseh K, Barbieri M, Rehm R, et al. High-resolution structural and functional deep brain imaging using adaptive optics three-photon microscopy. Nat Methods. 2021; 18: 1253–8.
39. Wu J, Liang Y, Chen S, Hsu CL, Chavarha M, Evans SW, et al. Kilohertz two-photon fluorescence microscopy imaging of neural activity *in vivo*. Nat Methods. 2020; 17: 287–90.
40. Karpf S, Riche CT, Di Carlo D, Goel A, Zeiger WA, Suresh A, et al. Spectro-temporal encoded multiphoton microscopy and fluorescence lifetime imaging at kilohertz frame-rates. Nat Commun. 2020; 11: 2062.
41. Platisa J, Ye X, Ahrens AM, Liu C, Chen IA, Davison IG, et al. High-speed low-light *in vivo* two-photon voltage imaging of large neuronal populations. Nat Methods. 2023; 20: 1095–103.
42. Griffiths VA, Valera AM, Lau JY, Roš H, Younts TJ, Marin B, et al. Real-time 3D movement correction for two-photon imaging in behaving animals. Nat Methods. 2020; 17: 741–8.
43. Chakraborty T, Chen B, Daetwyler S, Chang BJ, Vanderpoorten O, Sapoznik E, et al. Converting lateral scanning into axial focusing to speed up three-dimensional microscopy. Light Sci Appl. 2020; 9: 165.
44. He H, Dong X, Ren YX, Lai CSW, Tsia KK, Wong KKY. Tomographic-encoded multiphoton microscopy. ACS Photonics. 2022; 9: 3291–301.
45. Chen W, Ge X, Zhang Q, Natan RG, Fan JL, Scanziani M, et al. High-throughput volumetric mapping of synaptic transmission. Nat Methods. 2024; 21: 1298–305.
46. Bredfeldt JE, Oracz J, Kiszka KA, Moosmayer T, Weber M, Sahl SJ, et al. Bleaching protection and axial sectioning in fluorescence nanoscopy through two-photon activation at 515 nm. Nat Commun. 2024; 15: 7472.
47. Chen X, Zhong S, Hou Y, Cao R, Wang W, Li D, et al. Superresolution structured illumination microscopy reconstruction algorithms: A review. Light Sci Appl. 2023; 12: 172.
48. Zong WJ, Wu RL, Li ML, Hu YH, Li YJ, Li JH, et al. Fast high-resolution miniature two-photon microscopy for brain imaging in freely behaving mice. Nat Methods, 2017; 14: 713–9.
49. Zhao C, Chen S, Zhang L, Zhang D, Wu R, Hu Y, et al. Miniature three-photon microscopy maximized for scattered fluorescence collection. Nat Methods. 2023; 20: 617–22.
50. Zhang ZX, Liu SJ, Mattison B, Muir J, Spurr N, Kim CK, et al. High-speed neural imaging with multiplexed miniature two-photon microscopy (M-MINI2P). BioRxiv. 2025; 5: 101221.
51. Chen K, Tian Z, Kong L. Advances of optical miniscopes for *in vivo* imaging of neural activity in freely moving animals. Front Neurosci. 2022; 16: 994079.
52. Li B, Wu C, Wang M, Charan K, Xu C. An adaptive excitation source for high-speed multiphoton microscopy. Nat Methods. 2020; 17: 163–6.
53. Li YY, Guo S, Mattison B, Hu JJ, Man KNM, Tang WJ. High-speed two-photon microscopy with adaptive line-excitation. Optica. 2024; 11: 1138–45.
54. Mahecic D, Stepp WL, Zhang C, Griffié J, Weigert M, Manley S. Event-driven acquisition for content-enriched microscopy. Nat Methods. 2022; 19: 1262–7.
55. Xu CT, Zhan Q, Liu H, Somesfalean G, Qian J, He S, et al. Upconverting nanoparticles for pre-clinical diffuse optical imaging, microscopy and sensing: Current trends and future challenges. Laser Photonics Rev. 2013; 7: 663–97.
56. Esipova TV, Ye X, Collins JE, Sakadžić S, Mandeville ET, Murray CB, et al. Dendritic upconverting nanoparticles enable *in vivo* multiphoton microscopy with low-power continuous wave sources. Proc Natl Acad Sci USA. 2012; 109: 20826–31.
57. Plunkett S, El Khatib M, Şencan İ, Porter JE, Kumar ATN, Collins JE, et al. *In vivo* deep-tissue microscopy with UCNP/Janus-dendrimers as imaging probes: Resolution at depth and feasibility of ratiometric sensing. Nanoscale. 2020; 12: 2657–72.
58. Chamanzar M, Garfield DJ, Iafrati J, Chan EM, Sohal V, Cohen BE, et al. Upconverting nanoparticle micro-lightbulbs designed for deep tissue optical stimulation and imaging. Biomed Opt Express. 2018; 9: 4359–71.
59. Khabir Z, Guller AE, Rozova VS, Liang L, Lai YJ, Goldys EM, et al. Tracing upconversion nanoparticle penetration in human skin. Colloids Surf B Biointerfaces. 2019; 184: 110480.
60. Liu J, Wu R, Li N, Zhang X, Zhan Q, He S. Deep, high contrast microscopic cell imaging using three-photon luminescence of β-($NaYF_4$:Er^{3+}/$NaYF_4$) nanoprobe excited by 1480-nm CW laser of only 15-mW. Biomed Opt Express. 2015; 6: 1857–66.
61. Wen X, Wang B, Wu R, Li N, He S, Zhan Q. Designed Er^{3+}-singly doped $NaYF_4$ with double excitation bands for simultaneous deep macroscopic and microscopic upconverting bioimaging. Biomed Opt Express. 2016; 7: 2174–85.
62. Kostyuk AB, Vorotnov AD, Ivanov AV, Volovetskiy AB, Kruglov AV, Sencha LM, et al. Resolution and contrast enhancement of laser-scanning multiphoton microscopy using thulium-doped upconversion nanoparticles. Nano Res. 2019; 12: 2933–40.
63. Yao J, Yu Z, Gao Y, Wang B, Wang Z, Zhong T, et al. Deep-penetrating and high-resolution continuous-wave nonlinear microscopy based on homologous dual-emission upconversion adaptive optics. Nano Lett. 2025; 25: 5485–92.
64. Liu Y, Lu Y, Yang X, Zheng X, Wen S, Wang F, et al. Amplified stimulated emission in upconversion nanoparticles for super-resolution nanoscopy. Nature. 2017; 543: 229–33.
65. Zhan Q, Liu H, Wang B, Wu Q, Pu R, Zhou C, et al. Achieving high-efficiency emission depletion nanoscopy by employing cross relaxation in upconversion nanoparticles. Nat Commun. 2017; 8: 1058.
66. Wu R, Zhan Q, Liu H, Wen X, Wang B, He S. Optical depletion mechanism of upconverting luminescence and its potential for multi-photon STED-like microscopy. Opt Express. 2015; 23: 32401–12.
67. Pu R, Zhan Q, Peng X, Liu S, Guo X, Liang L, et al. Super-resolution micro-

scopy enabled by high-efficiency surface-migration emission depletion. Nat Commun. 2022; 13: 6636.
68. Liang Y, Zhu Z, Qiao S, Guo X, Pu R, Tang H, et al. Migrating photon avalanche in different emitters at the nanoscale enables 46th-order optical nonlinearity. Nat Nanotechnol. 2022; 17: 524–30.
69. Lee C, Xu EZ, Liu Y, Teitelboim A, Yao K, Fernandez-Bravo A, et al. Giant nonlinear optical responses from photon-avalanching nanoparticles. Nature. 2021; 589: 230–5.
70. Liu B, Chen C, Di X, Liao J, Wen S, Su QP, et al. Upconversion nonlinear structured illumination microscopy. Nano Lett. 2020; 20: 4775–81.
71. Wang B, Zhan Q, Zhao Y, Wu R, Liu J, He S. Visible-to-visible four-photon ultrahigh resolution microscopic imaging with 730-nm diode laser excited nanocrystals. Opt Express. 2016; 24: A302–11.
72. Guo X, Pu R, Zhu Z, Qiao S, Liang Y, Huang B, et al. Achieving low-power single-wavelength-pair nanoscopy with NIR-II continuous-wave laser for multichromatic probes. Nat Commun. 2022; 13: 2843.
73. Chen C, Wang F, Wen S, Su QP, Wu MCL, Liu Y, et al. Multi-photon near-infrared emission saturation nanoscopy using upconversion nanoparticles. Nat Commun. 2018; 9: 3290.
74. James ML, Gambhir SS. A molecular imaging primer: Modalities, imaging agents, and applications. Physiol Rev. 2012; 92: 897–965.
75. Hu Z, Fang C, Li B, Zhang Z, Cao C, Cai M, et al. First-in-human liver-tumour surgery guided by multispectral fluorescence imaging in the visible and near-infrared-I/II windows. Nat Biomed Eng. 2020; 4: 259–71.
76. Hong G, Antaris AL, Dai H. Near-infrared fluorophores for biomedical imaging. Nat Biomed Eng. 2017; 1: 10.
77. Antaris AL, Chen H, Cheng K, Sun Y, Hong G, Qu C, et al. A small-molecule dye for NIR-II imaging. Nature Mater. 2016; 15: 235–42.
78. Zhang Z, Fang C, He K, Tian J. NIR-II fluorescence image-guided surgery prolongs the relapse-free survival of hepatocellular carcinoma patients. HPB. 2024; 26: 963–6.
79. Shi X, Zhang Z, Zhang Z, Cao C, Cheng Z, Hu Z, et al. Near-infrared window II fluorescence image-guided surgery of high-grade gliomas prolongs the progression-free survival of patients. IEEE Trans Biomed Eng. 2022; 69: 1889–900.
80. Cao C, Jin Z, Shi X, Zhang Z, Xiao A, Yang J, et al. First clinical investigation of near-infrared window IIa/IIb fluorescence imaging for precise surgical resection of gliomas. IEEE Trans Biomed Eng. 2022; 69: 2404–13.
81. Cao C, Deng S, Wang B, Shi X, Ge L, Qiu M, et al. Intraoperative near-infrared II window fluorescence imaging-assisted nephron-sparing surgery for complete resection of cystic renal masses. Clinical & Translational Med. 2021; 11: e604.
82. Mi J, Li C, Yang F, Shi X, Zhang Z, Guo L, et al. Comparative study of indocyanine green fluorescence imaging in lung cancer with near-infrared-I/II windows. Ann Surg Oncol. 2024; 31: 2451–60.
83. Fan X, Yang J, Ni H, Xia Q, Liu X, Wu T, et al. Initial experience of NIR-II fluorescence imaging-guided surgery in foot and ankle surgery. Engineering. 2024; 40: 19–27.
84. Qu Q, Nie H, Hou S, Wang F, He K, Deng P, et al. Visualisation of pelvic autonomic nerves using NIR-II fluorescence imaging. Eur J Nucl Med Mol Imaging. 2022; 49: 4752–4.
85. Wakabayashi T, Cacciaguerra AB, Abe Y, Dalla Bona E, Nicolini D, Mocchegiani F, et al. Indocyanine green fluorescence navigation in liver surgery: A systematic review on dose and timing of administration. Ann Surg. 2022; 275: 1025–34.
86. He S, Song J, Qu J, Cheng Z. Crucial breakthrough of second near-infrared biological window fluorophores: Design and synthesis toward multimodal imaging and theranostics. Chem Soc Rev. 2018; 47: 4258–78.
87. Zhang Z, He K, Chi C, Hu Z, Tian J. Intraoperative fluorescence molecular imaging accelerates the coming of precision surgery in China. Eur J Nucl Med Mol Imag. 2022; 49: 2531–43.
88. Chen W, Zhang Y, Zhang L, Luo X, Yang X, Zhu Y, et al. Intraoperative evaluation of tumor margins using a TROP2 near-infrared imaging probe to enable human breast-conserving surgery. Sci Transl Med. 2024; 16: eado2461.
89. Wang B, Tang C, Lin E, Jia X, Xie G, Li P, et al. NIR-II fluorescence-guided liver cancer surgery by a small molecular HDAC6 targeting probe. EBioMedicine. 2023; 98: 104880.
90. Zhong Y, Ma Z, Wang F, Wang X, Yang Y, Liu Y, et al. *In vivo* molecular imaging for immunotherapy using ultra-bright near-infrared-IIb rare-earth nanoparticles. Nat Biotechnol. 2019; 37: 1322–31.
91. Chan MH, Chang YC. Recent advances in near-infrared I/II persistent luminescent nanoparticles for biosensing and bioimaging in cancer analysis. Anal Bioanal Chem. 2024; 416: 3887–905.
92. Ma Z, Wang F, Wang W, Zhong Y, Dai H. Deep learning for *in vivo* near-infrared imaging. Proc Natl Acad Sci USA. 2021; 118: e2021446118.
93. Fu L, Lu B, Tian J, Hu Z. PSSGAN: Towards spectrum shift based perceptual quality enhancement for fluorescence imaging. Comput Med Imag Graph. 2023; 107: 102216.
94. Yu X, Tian J, Hu Z. Universal NIR-II fluorescence image enhancement via covariance weighted attention network. Multimed Syst. 2024; 30: 335.
95. Feng R, Li G, Ko CN, Zhang Z, Wan JB, Zhang QW. Long-lived second near-infrared luminescent probes: An emerging role in time-resolved luminescence bioimaging and biosensing. Small Struct. 2023; 4: 2370005.
96. Zeng Z, Ouyang J, Sun L, Zeng C, Zeng F, Wu S. Activatable nanocomposite probe for preoperative location and intraoperative navigation for orthotopic hepatic tumor resection via MSOT and aggregation-induced near-IR-I/II fluorescence imaging. Anal Chem. 2020; 92: 9257–64.
97. Zhang Z, Du Y, Shi X, Wang K, Qu Q, Liang Q, et al. NIR-II light in clinical oncology: Opportunities and challenges. Nat Rev Clin Oncol. 2024; 21: 449–67.
98. Ferrari M, Quaresima V. A brief review on the history of human functional near-infrared spectroscopy (fNIRS) development and fields of application. NeuroImage. 2012; 63: 921–35.
99. Eggebrecht AT, Ferradal SL, Robichaux-Viehoever A, Hassanpour MS, Dehghani H, Snyder AZ, et al. Mapping distributed brain function and networks with diffuse optical tomography. Nature Photon. 2014; 8: 448–54.
100. Vidal-Rosas EE, von Lühmann A, Pinti P, Cooper RJ. Wearable, high-density fNIRS and diffuse optical tomography technologies: A perspective. Neurophotonics. 2023; 10: 023513.
101. Huo C, Xu G, Li Z, Lv Z, Liu Q, Li W, et al. Limb linkage rehabilitation training-related changes in cortical activation and effective connectivity after stroke: A functional near-infrared spectroscopy study. Sci Rep. 2019; 9: 6226.
102. Cui X, Bryant DM, Reiss AL. NIRS-based hyperscanning reveals increased interpersonal coherence in superior frontal cortex during cooperation. NeuroImage. 2012; 59: 2430–7.
103. Wu YJ, Hou X, Peng C, Yu W, Oppenheim GM, Thierry G, et al. Rapid learning of a phonemic discrimination in the first hours of life. Nat Hum Behav. 2022; 6: 1169–79.
104. Huo C, Xu G, Xie H, Chen T, Shao G, Wang J, et al. Functional near-infrared spectroscopy in non-invasive neuromodulation. Neural Regen Res. 2024; 19: 1517–22.
105. Yang J, Zhang H, Ni J, De Dreu CKW, Ma Y. Within-group synchronization in the prefrontal cortex associates with intergroup conflict. Nat Neurosci. 2020; 23: 754–60.
106. Gao Y, Rogers D, von Lühmann A, Ortega-Martinez A, Boas DA, Yücel MA. Short-separation regression incorporated diffuse optical tomography image reconstruction modeling for high-density functional near-infrared spectroscopy. Neurophotonics. 2023; 10: 025007.
107. Scholkmann F, Kleiser S, Metz AJ, Zimmermann R, Mata Pavia J, Wolf U, et al. A review on continuous wave functional near-infrared spectroscopy and imaging instrumentation and methodology. NeuroImage. 2014; 85: 6–27.
108. Wang LV, Hu S. Photoacoustic tomography: *In vivo* imaging from organelles to organs. Science. 2012; 335: 1458–62.
109. Taruttis A, Ntziachristos V. Advances in real-time multispectral optoacoustic imaging and its applications. Nature Photon. 2015; 9: 219–27.
110. Pang W, Zhu B, Li H, Zhou Y, Woo CM, Huang X, et al. Direct monitoring of whole-brain electrodynamics via high-spatiotemporal-resolution photoacoustics with voltage-sensitive dye. Laser Photonics Rev. 2024; 18: 2400165.
111. Zhou Y, Huang X, Li J, Zhu T, Pang W, Chow L, et al. Small animal *in situ* drug delivery effects via transdermal microneedles array versus intravenous injection: A pilot observation based on photoacoustic tomography. Pharmaceutics. 2022; 14: 2689.
112. Liang Y, Fu W, Li Q, Chen X, Sun H, Wang L, et al. Optical-resolution functional gastrointestinal photoacoustic endoscopy based on optical heterodyne detection of ultrasound. Nat Commun. 2022; 13: 7604.
113. Zhu L, Cao H, Ma J, Wang L. Optical ultrasound sensors for photoacoustic imaging: A review. J Biomed Opt. 2024; 29: S11523.
114. Cho S, Kim M, Ahn J, Kim Y, Lim J, Park J, et al. An ultrasensitive and broadband transparent ultrasound transducer for ultrasound and photoacoustic imaging *in-vivo*. Nat Commun. 2024; 15: 1444.
115. Guo P, Gao W, Lin R, Wang X, Lan J, Zhang J, et al. Advancement in PMN-PT transparent piezoelectric ceramic for photoacoustic/ultrasound dual-mode imaging. J Materiomics. 2025; 11: 100932.
116. Zhu X, Huang Q, DiSpirito A, Vu T, Rong Q, Peng X, et al. Real-time whole-brain imaging of hemodynamics and oxygenation at micro-vessel resolution with ultrafast wide-field photoacoustic microscopy. Light Sci Appl. 2022; 11: 138.
117. Luke GP, Emelianov SY. Label-free detection of lymph node metastases with US-guided functional photoacoustic imaging. Radiology. 2015; 277: 435–42.
118. Lv J, Lan H, Qin A, Sun T, Shao D, Gao F, et al. Dynamic synthetic-scanning photoacoustic tracking monitors hepatic and renal clearance pathway of exogeneous probes *in vivo*. Light Sci Appl. 2024; 13: 304.
119. Zhang Y, Wang Y, Lai P, Wang L. Video-rate dual-modal wide-beam harmonic ultrasound and photoacoustic computed tomography. IEEE Trans Med Imag. 2022; 41: 727–36.
120. Lin L, Wang LV. The emerging role of photoacoustic imaging in clinical oncology. Nat Rev Clin Oncol. 2022; 19: 365–84.
121. Park J, Choi S, Knieling F, Clingman B, Bohndiek S, Wang LV, et al. Clinical translation of photoacoustic imaging. Nat Rev Bioeng. 2025; 3: 193–212.
122. Na S, Russin JJ, Lin L, Yuan X, Hu P, Jann KB, et al. Massively parallel

functional photoacoustic computed tomography of the human brain. Nat Biomed Eng. 2022; 6: 584–92.
123. Zhang F, Zhang J, Shen Y, Gao Z, Yang C, Liang M, et al. Photoacoustic digital brain and deep-learning-assisted image reconstruction. Photoacoustics. 2023; 31: 100517.
124. Sastry K, Aborahama Y, Luo Y, Zhang Y, Cui M, Cao R, et al. Transcranial photoacoustic tomography de-aberrated using boundary elements. IEEE Trans Med Imaging. 2025; 44: 2068–78.
125. Ji N. Adaptive optical fluorescence microscopy. Nat Methods. 2017; 14: 374–80.
126. Zhang Q, Hu Q, Berlage C, Kner P, Judkewitz B, Booth M, et al. Adaptive optics for optical microscopy. Biomed Opt Express. 2023; 14: 1732–56.
127. Hampson KM, Turcotte R, Miller DT, Kurokawa K, Males JR, Ji N, et al. Adaptive optics for high-resolution imaging. Nat Rev Meth Primers. 2021; 1: 68.
128. Babcock HW. The possibility of compensating astronomical seeing. Publ Astron Soc Pac. 1953; 65: 229.
129. Panagopoulou SI, Neal DP. Zonal matrix iterative method for wavefront reconstruction from gradient measurements. J Refract Surg. 2005; 21: S563–9.
130. Wang K, Milkie DE, Saxena A, Engerer P, Misgeld T, Bronner ME, et al. Rapid adaptive optical recovery of optimal resolution over large volumes. Nat Methods. 2014; 11: 625–8.
131. Liu TL, Upadhyayula S, Milkie DE, Singh V, Wang K, Swinburne IA, et al. Observing the cell in its native state: Imaging subcellular dynamics in multicellular organisms. Science. 2018; 360: eaaq1392.
132. Wang K, Sun W, Richie CT, Harvey BK, Betzig E, Ji N. Direct wavefront sensing for high-resolution *in vivo* imaging in scattering tissue. Nat Commun. 2015; 6: 7276.
133. Liu R, Li Z, Marvin JS, Kleinfeld D. Direct wavefront sensing enables functional imaging of infragranular axons and spines. Nat Methods. 2019; 16: 615–8.
134. Ji N, Milkie DE, Betzig E. Adaptive optics via pupil segmentation for high-resolution imaging in biological tissues. Nat Methods. 2010; 7: 141–7.
135. Milkie DE, Betzig E, Ji N. Pupil-segmentation-based adaptive optical microscopy with full-pupil illumination. Opt Lett. 2011; 36: 4206–8.
136. Wang C, Liu R, Milkie DE, Sun W, Tan Z, Kerlin A, et al. Multiplexed aberration measurement for deep tissue imaging *in vivo*. Nat Methods. 2014; 11: 1037–40.
137. Rodríguez C, Chen A, Rivera JA, Mohr MA, Liang Y, Natan RG, et al. An adaptive optics module for deep tissue multiphoton imaging *in vivo*. Nat Methods. 2021; 18: 1259–64.
138. Ji N, Sato TR, Betzig E. Characterization and adaptive optical correction of aberrations during *in vivo* imaging in the mouse cortex. Proc Natl Acad Sci USA. 2012; 109: 22–7.
139. Chen W, Natan RG, Yang Y, Chou SW, Zhang Q, Isacoff EY, et al. *In vivo* volumetric imaging of calcium and glutamate activity at synapses with high spatiotemporal resolution. Nat Commun. 2021; 12: 6630.
140. Streich L, Boffi JC, Wang L, Alhalaseh K, Barbieri M, Rehm R, et al. High-resolution structural and functional deep brain imaging using adaptive optics three-photon microscopy. Nat Methods. 2021; 18: 1253–8.
141. Booth MJ, Neil MAA, Juškaitis R, Wilson T. Adaptive aberration correction in a confocal microscope. Proc Natl Acad Sci USA. 2002; 99: 5788–92.
142. Jesacher A, Thayil A, Grieve K, Débarre D, Watanabe T, Wilson T, et al. Adaptive harmonic generation microscopy of mammalian embryos. Opt Lett. 2009; 34: 3154–6.
143. Débarre D, Botcherby EJ, Watanabe T, Srinivas S, Booth MJ, Wilson T. Image-based adaptive optics for two-photon microscopy. Opt Lett. 2009; 34: 2495–7.
144. Burke D, Patton B, Huang F, Bewersdorf J, Booth MJ. Adaptive optics correction of specimen-induced aberrations in single-molecule switching microscopy. Optica. 2015; 2: 177.
145. Qin Z, She Z, Chen C, Wu W, Lau JKY, Ip NY, et al. Deep tissue multi-photon imaging using adaptive optics with direct focus sensing and shaping. Nat Biotechnol. 2022; 40: 1663–71.
146. Papadopoulos IN, Jouhanneau JS, Poulet JFA, Judkewitz B. Scattering compensation by focus scanning holographic aberration probing (F-SHARP). Nature Photon. 2017; 11: 116–23.
147. May MA, Barré N, Kummer KK, Kress M, Ritsch-Marte M, Jesacher A. Fast holographic scattering compensation for deep tissue biological imaging. Nat Commun. 2021; 12: 4340.
148. Berlage C, Tantirigama MLS, Babot M, Di Battista D, Whitmire C, Papadopoulos IN, et al. Deep tissue scattering compensation with three-photon F-SHARP. Optica. 2021; 8: 1613–9.
149. Gonsalves RA. Phase retrieval and diversity in adaptive optics. Opt Eng. 1982; 21: 829–32.
150. Kner P, Winoto L, Agard DA, Sedat JW. Closed loop adaptive optics for microscopy without a wavefront sensor. Proc SPIE Int SOC Opt Eng. 2010; 7570: 757006.
151. Kner P. Phase diversity for three-dimensional imaging. J Opt Soc Am A. 2013; 30: 1980–7.
152. Wu J, Lu Z, Jiang D, Guo Y, Qiao H, Zhang Y, et al. Iterative tomography with digital adaptive optics permits hour-long intravital observation of 3D subcellular dynamics at millisecond scale. Cell. 2021; 184: 3318–32.e17.
153. Guo M, Wu Y, Hobson CM, Su Y, Qian S, Krueger E, et al. Deep learning-based aberration compensation improves contrast and resolution in fluorescence microscopy. Nat Commun. 2025; 16: 313.
154. Hu Q, Hailstone M, Wang J, Wincott M, Stoychev D, Atilgan H, et al. Universal adaptive optics for microscopy through embedded neural network control. Light Sci Appl. 2023; 12: 270.
155. Kang I, Zhang Q, Yu SX, Ji N. Coordinate-based neural representations for computational adaptive optics in widefield microscopy. Nat Mach Intell. 2024; 6: 714–25.
156. Kang, I., Kim H, Natan R, Zhang QR, Yu SX, Ji N. Adaptive optical correction for *in vivo* two-photon fluorescence microscopy with neural fields. BioRxiv, 2024; doi: 10.1101/2024.10.20.619284.
157. Yu Z, Li H, Zhong T, Park JH, Cheng S, Woo CM, et al. Wavefront shaping: A versatile tool to conquer multiple scattering in multidisciplinary fields. Innovation. 2022; 3: 100292.
158. Li H, Yu Z, Zhong T, Lai P. Performance enhancement in wavefront shaping of multiply scattered light: A review. J Biomed Opt. 2024; 29: S11512.
159. Shen Y, Liu Y, Ma C, Wang LV. Focusing light through biological tissue and tissue-mimicking phantoms up to 9.6 cm in thickness with digital optical phase conjugation. J Biomed Opt. 2016; 21: 085001.
160. Yaqoob Z, Psaltis D, Feld MS, Yang C. Optical phase conjugation for turbidity suppression in biological samples. Nature Photon. 2008; 2: 110–5.
161. Liu Y, Lai P, Ma C, Xu X, Grabar AA, Wang LV. Optical focusing deep inside dynamic scattering media with near-infrared time-reversed ultrasonically encoded (TRUE) light. Nat Commun. 2015; 6: 5904.
162. Liu H, Xu X, Lai P, Wang LV. Time-reversed ultrasonically encoded optical focusing into tissue-mimicking media with thickness up to 70 mean free paths. J Biomed Opt. 2011; 16: 086009.
163. Suzuki Y, Lai P, Xu X, Wang L. High-sensitivity ultrasound-modulated optical tomography with a photorefractive polymer. Opt Lett. 2013; 38: 899–901.
164. Cui M, Yang C. Implementation of a digital optical phase conjugation system and its application to study the robustness of turbidity suppression by phase conjugation. Opt Express. 2010; 18: 3444–55.
165. Li H, Yu Z, Zhong T, Cheng S, Lai P. Towards ideal focusing of diffused light via optical wavefront shaping. Adv Photon. 2023; 5: 020502.
166. Ma C, Zhou F, Liu Y, Wang LV. Single-exposure optical focusing inside scattering media using binarized time-reversed adapted perturbation. Optica. 2015; 2: 869–76.
167. Wang D, Zhou EH, Brake J, Ruan H, Jang M, Yang C. Focusing through dynamic tissue with millisecond digital optical phase conjugation. Optica. 2015; 2: 728–35.
168. Hemphill AS, Shen Y, Liu Y, Wang LV. High-speed single-shot optical focusing through dynamic scattering media with full-phase wavefront shaping. Appl Phys Lett. 2017; 111: 221109.
169. Liu Y, Ma C, Shen Y, Shi J, Wang LV. Focusing light inside dynamic scattering media with millisecond digital optical phase conjugation. Optica. 2017; 4: 280–8.
170. Luo J, Liu Y, Wu D, Xu X, Shao L, Feng Y, et al. High-speed single-exposure time-reversed ultrasonically encoded optical focusing against dynamic scattering. Sci Adv. 2022; 8: eadd9158.
171. Horstmeyer R, Ruan H, Yang C. Guidestar-assisted wavefront-shaping methods for focusing light into biological tissue. Nature Photon. 2015; 9: 563–71.
172. Park JH, Yu Z, Lee K, Lai P, Park Y. Perspective: Wavefront shaping techniques for controlling multiple light scattering in biological tissues: Toward *in vivo* applications. APL Photonics. 2018; 3: 100901.
173. Vellekoop IM, Mosk AP. Focusing coherent light through opaque strongly scattering media. Opt Lett. 2007; 32: 2309–11.
174. Yang J, He Q, Liu L, Qu Y, Shao R, Song B, et al. Anti-scattering light focusing by fast wavefront shaping based on multi-pixel encoded digital-micromirror device. Light Sci Appl. 2021; 10: 149.
175. Nam K, Park JH. Increasing the enhancement factor for DMD-based wavefront shaping. Opt Lett. 2020; 45: 3381–4.
176. Woo CM, Zhao Q, Zhong T, Li H, Yu Z, Lai P. Optimal efficiency of focusing diffused light through scattering media with iterative wavefront shaping. APL Photonics. 2022; 7: 046109.
177. Haim O, Boger-Lombard J, Katz O. Image-guided computational holographic wavefront shaping. Nat Photon. 2025; 19: 44–53.
178. Li H, Woo CM, Zhong T, Yu Z, Luo Y, Zheng Y, et al. Adaptive optical focusing through perturbed scattering media with a dynamic mutation algorithm. Photon Res. 2021; 9: 202–12.
179. Luo Y, Yan S, Li H, Lai P, Zheng Y. Focusing light through scattering media by reinforced hybrid algorithms. APL Photonics. 2020; 5: 016109.
180. Yeminy T, Katz O. Guidestar-free image-guided wavefront shaping. Sci Adv. 2021; 7: eabf5364.
181. Thendiyammal A, Osnabrugge G, Knop T, Vellekoop IM. Model-based wavefront shaping microscopy. Opt Lett. 2020; 45: 5101–4.
182. Liu L, Ding C, Qu Y, He Q, Shao R, Yang J. Anti-scattering light focusing by

full-polarization wavefront shaping based on digital micromirror devices. Appl Phys Express. 2022; 15: 092001.
183. Feng BY, Guo H, Xie M, Boominathan V, Sharma MK, Veeraraghavan A, et al. NeuWS: Neural wavefront shaping for guidestar-free imaging through static and dynamic scattering media. Sci Adv. 2023; 9: eadg4671.
184. Cao H, Čižmár T, Turtaev S, Tyc T, Rotter S. Controlling light propagation in multimode fibers for imaging, spectroscopy, and beyond. Adv Opt Photon. 2023; 15: 524–612.
185. Park J, Lee K, Park Y. Ultrathin wide-angle large-area digital 3D holographic display using a non-periodic photon sieve. Nat Commun. 2019; 10: 1304.
186. Bertolotti J, Katz O. Imaging in complex media. Nat Phys. 2022; 18: 1008–17.
187. Tripathi S, Paxman R, Bifano T, Toussaint KC. Vector transmission matrix for the polarization behavior of light propagation in highly scattering media. Opt Express. 2012; 20: 16067–76.
188. Popoff SM, Lerosey G, Carminati R, Fink M, Boccara AC, Gigan S. Measuring the transmission matrix in optics: An approach to the study and control of light propagation in disordered media. Phys Rev Lett. 2010; 104: 100601.
189. Yu H, Hillman TR, Choi W, Lee JO, Feld MS, Dasari RR, et al. Measuring large optical transmission matrices of disordered media. Phys Rev Lett. 2013; 111: 153902.
190. Yoon J, Lee K, Park J, Park Y. Measuring optical transmission matrices by wavefront shaping. Opt Express. 2015; 23: 10158–67.
191. Chaigne T, Katz O, Boccara AC, Fink M, Bossy E, Gigan S. Controlling light in scattering media non-invasively using the photoacoustic transmission matrix. Nature Photon. 2014; 8: 58–64.
192. Boniface A, Dong J, Gigan S. Non-invasive focusing and imaging in scattering media with a fluorescence-based transmission matrix. Nat Commun. 2020; 11: 6154.
193. Liu YF, Yu PY, Wu YJ, Wang ZQ, Li YM, Liang JY, et al. Single-shot wide-field imaging in reflection by using a single multimode fiber. Appl Phys Lett. 2023; 122: 063701.
194. Gobé B, Saucourt J, Shpakovych M, Helbert D, Desfarges-Berthelemot A, Kermene V. Retrieving the complex transmission matrix of a multimode fiber by machine learning for 3D beam shaping. J Lightwave Technol. 2024; 42: 4681–8.
195. Yu P, Liu Y, Wu Y, Zhuang J, Wang Z, Li Y, et al. Large-FOV scattering-assisted holographic projection by enhanced sampling of transmission matrix. Appl Phys Lett. 2023; 122: 061104.
196. Cheng S, Zhang X, Zhong T, Li H, Li H, Gong L, et al. Nonconvex optimization for optimum retrieval of the transmission matrix of a multimode fiber. Adv Photon Nexus. 2023; 2: 066005.
197. Yu P, Liu Y, Wang Z, Liang J, Liu X, Li Y, et al. Ultrahigh-density 3D holographic projection by scattering-assisted dynamic holography. Optica. 2023; 10: 481.
198. Zhuang JH, Yu PP, Liu YF, Wu YJ, Wang ZQ, Li YM, et al. Dynamic 3D holographic projection of vectorial images with a multimode fiber. Photon Res. 2024; 12: 1344.
199. Popoff S, Lerosey G, Fink M, Boccara AC, Gigan S. Image transmission through an opaque material. Nat Commun. 2010; 1: 81.
200. Yu Z, Li H, Zhong T, Lai P. Enhancing spatiotemporal focusing of light deep inside scattering media with Time-Gated Reflection Matrix. Light Sci Appl. 2022; 11: 167.
201. Choi Y, Yoon C, Kim M, Yang TD, Fang-Yen C, Dasari RR, et al. Scanner-free and wide-field endoscopic imaging by using a single multimode optical fiber. Phys Rev Lett. 2012; 109: 203901.
202. Wen Z, Dong Z, Deng Q, Pang C, Kaminski CF, Xu X, et al. Single multimode fibre for *in vivo* light-field-encoded endoscopic imaging. Nat Photon. 2023; 17: 679–87.
203. Cheng S, Zhong T, Chi MW, Li H, Lai P. Lensless fiber-optic imaging via coherent light modulation and its applications. Laser Optoelectron Prog. 2024; 61: 0618002.
204. Čižmár T, Dholakia K. Shaping the light transmission through a multimode optical fibre: Complex transformation analysis and applications in biophotonics. Opt Express. 2011; 19: 18871–84.
205. Andreoli D, Volpe G, Popoff S, Katz O, Grésillon S, Gigan S. Deterministic control of broadband light through a multiply scattering medium via the multispectral transmission matrix. Sci Rep. 2015; 5: 10347.
206. Morales-Delgado EE, Farahi S, Papadopoulos IN, Psaltis D, Moser C. Delivery of focused short pulses through a multimode fiber. Opt Express. 2015; 23: 9109–20.
207. Loterie DCM. Microscopy and digital light shaping through optical fibers. Lausanne: École Polytechnique Fédérale de Lausanne. 2017.
208. Wen Z, Wang L, Zhang X, Ma Y, Liu X, Kaminski CF, et al. Fast volumetric fluorescence imaging with multimode fibers. Opt Lett. 2020; 45: 4931–4.
209. Loterie D, Farahi S, Papadopoulos I, Goy A, Psaltis D, Moser C. Digital confocal microscopy through a multimode fiber. Opt Express. 2015; 23: 23845–58.
210. Lee SY, Parot VJ, Bouma BE, Villiger M. Confocal 3D reflectance imaging through multimode fiber without wavefront shaping. Optica. 2022; 9: 112–20.
211. Liu Z, Wang L, Meng Y, He T, He S, Yang Y, et al. All-fiber high-speed image detection enabled by deep learning. Nat Commun. 2022; 13: 1433.
212. Farahi S, Ziegler D, Papadopoulos IN, Psaltis D, Moser C. Dynamic bending compensation while focusing through a multimode fiber. Opt Express. 2013; 21: 22504–14.
213. Li S, Horsley SAR, Tyc T, Čižmár T, Phillips DB. Memory effect assisted imaging through multimode optical fibres. Nat Commun. 2021; 12: 3751.
214. Gordon GSD, Gataric M, Ramos AGCP, Mouthaan R, Williams C, Yoon J, et al. Characterizing optical fiber transmission matrices using metasurface reflector stacks for lensless imaging without distal access. Phys Rev X. 2019; 9: 041050.
215. Leite IT, Turtaev S, Boonzajer Flaes DE, Čižmár T. Observing distant objects with a multimode fiber-based holographic endoscope. APL Photonics. 2021; 6: 036112.
216. Stellinga D, Phillips DB, Mekhail SP, Selyem A, Turtaev S, Čižmár T, et al. Time-of-flight 3D imaging through multimode optical fibers. Science. 2021; 374: 1395–9.
217. Gusachenko I, Chen M, Dholakia K. Raman imaging through a single multimode fibre. Opt Express. 2017; 25: 13782–98.
218. Trägårdh J, Pikálek T, Šerý M, Meyer T, Popp J, Čižmár T. Label-free CARS microscopy through a multimode fiber endoscope. Opt Express. 2019; 27: 30055–66.
219. Turcotte R, Schmidt CC, Booth MJ, Emptage NJ. Volumetric two-photon fluorescence imaging of live neurons using a multimode optical fiber. Opt Lett. 2020; 45: 6599–602.
220. Cifuentes A, Pikálek T, Ondráčková P, Amezcua-Correa R, Antonio-Lopez JE, Čižmár T, et al. Polarization-resolved second-harmonic generation imaging through a multimode fiber. Optica. 2021; 8: 1065–74.
221. Stibůrek M, Ondráčková P, Tučková T, Turtaev S, Šiler M, Pikálek T, et al. 110 µm thin endo-microscope for deep-brain *in vivo* observations of neuronal connectivity, activity and blood flow dynamics. Nat Commun. 2023; 14: 1897.
222. Vasquez-Lopez SA, Turcotte R, Koren V, Plöschner M, Padamsey Z, Booth MJ, et al. Subcellular spatial resolution achieved for deep-brain imaging *in vivo* using a minimally invasive multimode fiber. Light Sci Appl. 2018; 7: 110.
223. Dong Z, Wen Z, Pang C, Wang L, Wu L, Liu X, et al. A modulated sparse random matrix for high-resolution and high-speed 3D compressive imaging through a multimode fiber. Sci Bull. 2022; 67: 1224–8.
224. Caravaca-Aguirre AM, Singh S, Labouesse S, Baratta MV, Piestun R, Bossy E. Hybrid photoacoustic-fluorescence microendoscopy through a multimode fiber using speckle illumination. APL Photonics. 2019; 4: 096103.
225. Li Q, Wen Z, Deng Q, Huang L, Hu Z, Liu X, et al. Phase imaging through a single multimode fiber. Opt Lett. 2024; 49: 5823–6.
226. Indebetouw G, Klysubun P. Imaging through scattering media with depth resolution by use of low-coherence gating in spatiotemporal digital holography. Opt Lett. 2000; 25: 212–4.
227. Takeda M, Osten W, Watanabe E. Holographic 3D imaging through random media: Methodologies and challenges. Light: Adv Manuf. 2022; 3: 301–13.
228. Chen H, Wu X, Liu G, Chen Z, Pu J. Single-shot complex field imaging through a diffuser by in-line holography with polarization multiplexing. Results Phys. 2023; 44: 106134.
229. Ushenko A, Zheng J, Gorsky M, Dubolazov A, Ushenko Y, Soltys I, et al. 3D digital holographic polarimetry of diffuse optically anisotropic biological tissue object fields. Front Phys. 2023; 11: 1288935.
230. Li R, Peng T, Bai C, Zhou M, Yu X, Min J, et al. Single shot depth-resolved imaging through dynamic turbid media. Appl Phys Lett. 2024; 124: 201109.
231. Zhang H, Liu S, Cao L, Brady DJ. Noise suppression for ballistic-photons based on compressive in-line holographic imaging through an inhomogeneous medium. Opt Express. 2020; 28: 10337–49.
232. Wang YM, Judkewitz B, DiMarzio CA, Yang C. Deep-tissue focal fluorescence imaging with digitally time-reversed ultrasound-encoded light. Nat Commun. 2012; 3: 928.
233. Lu J, Zeng Y, Chang X, Hong Y, Hu X. Quantitative phase imaging of cells through turbid media based on infrared digital holographic microscopy. Appl Phys Express. 2021; 14: 035004.
234. Takeda M, Singh AK, Naik DN, Pedrini G, Osten W. Holographic correloscopy-unconventional holographic techniques for imaging a three-dimensional object through an opaque diffuser or via a scattering wall: A review. IEEE Trans Ind Inform. 2016; 12: 1631–40.
235. Vinu VR, Kim K, Somkuwar AS, Park Y, Singh RK. Imaging through scattering media using digital holography. Opt Commun. 2019; 439: 218–23.
236. Ohta M, Kodama S, Miyamoto Y, Osten W, Takeda M, Watanabe E. 3D imaging through a highly heterogeneous double-composite random medium by common-path phase-shift digital holography. Opt Lett. 2022; 47: 1170–3.
237. Liao M, Feng Y, Lu D, Li X, Pedrini G, Frenner K, et al. Scattering imaging as a noise removal in digital holography by using deep learning. New J Phys. 2022; 24: 083014.
238. Heeman W, Steenbergen W, van Dam GM, Boerma EC. Clinical applications of laser speckle contrast imaging: A review. J Biomed Opt. 2019; 24: 1.
239. Konovalov A, Gadzhiagaev V, Grebenev F, Stavtsev D, Piavchenko G, Gerasimenko A, et al. Laser speckle contrast imaging in neurosurgery: A systematic

review. World Neurosurg. 2023; 171: 35–40.
240. Linkous C, Pagan AD, Shope C, Andrews L, Snyder A, Ye T, et al. Applications of laser speckle contrast imaging technology in dermatology. JID Innov. 2023; 3: 100187.
241. Brinca A, Pinho A, Vieira R. Laser speckle contrast imaging for assessment of human skin graft microcirculation. Acad Dermatol Venereol. 2020; 34: e491–3.
242. Feng X, Yu Y, Zou D, Jin Z, Zhou C, Liu G, et al. Functional imaging of human retina using integrated multispectral and laser speckle contrast imaging. J Biophotonics. 2022; 15: e202100285.
243. Souza EG, De Lorenzo A, Huguenin G, Oliveira GMM, Tibiriçá E. Impairment of systemic microvascular endothelial and smooth muscle function in individuals with early-onset coronary artery disease: Studies with laser speckle contrast imaging. Coron Artery Dis. 2014; 25: 23–8.
244. Fercher AF, Briers JD. Flow visualization by means of single-exposure speckle photography. Opt Commun. 1981; 37: 326–30.
245. Lemieux PA, Durian DJ. Investigating non-Gaussian scattering processes by using nth-order intensity correlation functions. J Opt Soc Am A. 1999; 16: 1651–64.
246. Sdobnov A, Piavchenko G, Bykov A, Meglinski I. Advances in dynamic light scattering imaging of blood flow. Laser Photonics Rev. 2024; 18: 2300494.
247. Wang Y, Wen D, Chen X, Huang Q, Chen M, Lu J, et al. Improving the estimation of flow speed for laser speckle imaging with single exposure time. Opt Lett. 2017; 42: 57–60.
248. Parthasarathy AB, Tom WJ, Gopal A, Zhang X, Dunn AK. Robust flow measurement with multi-exposure speckle imaging. Opt Express. 2008; 16: 1975–89.
249. Zakharov P, Völker AC, Wyss MT, Haiss F, Calcinaghi N, Zunzunegui C, et al. Dynamic laser speckle imaging of cerebral blood flow. Opt Express. 2009; 17: 13904–17.
250. Wang Y, Lv W, Chen X, Lu J, Li P. Improving the sensitivity of velocity measurements in laser speckle contrast imaging using a noise correction method. Opt Lett. 2017; 42: 4655–8.
251. Yuan S. Sensitivity, noise and quantitative model of laser speckle contrast imaging. Medford: Tufts University. 2008.
252. Hong J, Wang Y, Chen X, Lu J, Li P. Fluctuations of temporal contrast in laser speckle imaging of blood flow. Opt Lett. 2018; 43: 5214–17.
253. Skipetrov SE, Peuser J, Cerbino R, Zakharov P, Weber B, Scheffold F. Noise in laser speckle correlation and imaging techniques. Opt Express. 2010; 18: 14519–34.
254. Hong J, Shi L, Zhu X, Lu J, Li P. Laser speckle auto-inverse covariance imaging for mean-invariant estimation of blood flow. Opt Lett. 2019; 44: 5812–5.
255. Cheng W, Lu J, Zhu X, Hong J, Liu X, Li M, et al. Dilated residual learning with skip connections for real-time denoising of laser speckle imaging of blood flow in a log-transformed domain. IEEE Trans Med Imag. 2020; 39: 1582–93.
256. Cheng W, Zhu X, Chen X, Li M, Lu J, Li P. Manhattan distance-based adaptive 3D transform-domain collaborative filtering for laser speckle imaging of blood flow. IEEE Trans Med Imag. 2019; 38: 1726–35.
257. Rege A, Senarathna J, Li N, Thakor NV. Anisotropic processing of laser speckle images improves spatiotemporal resolution. IEEE Trans Biomed Eng. 2012; 59: 1272–80.
258. Liu X, Wei J, Meng L, Cheng W, Zhu X, Lu J, et al. Motion correction of laser speckle imaging of blood flow by simultaneous imaging of tissue structure and non-rigid registration. Opt Lasers Eng. 2021; 140: 106526.
259. Miao P, Rege A, Li N, Thakor NV, Tong S. High resolution cerebral blood flow imaging by registered laser speckle contrast analysis. IEEE Trans Biomed Eng. 2010; 57: 1152–7.
260. Liu X, Meng L, Hong J, Fu C, Lu J, Li P. Correcting non-rigid intra-frame motion of laser speckle contrast imaging by heterogeneous regression analysis. Opt Lasers Eng. 2023; 170: 107759.
261. Guilbert J, Desjardins M. Movement correction method for laser speckle contrast imaging of cerebral blood flow in cranial windows in rodents. J Biophotonics. 2022; 15: e202100218.
262. Hong J, Zhu X, Lu J, Li P. Quantitative laser speckle auto-inverse covariance imaging for robust estimation of blood flow. Opt Lett. 2021; 46: 2505–8.
263. Qureshi MM, Allam N, Im J, Kwon HS, Chung E, Vitkin IA. Advances in laser speckle imaging: From qualitative to quantitative hemodynamic assessment. J Biophotonics. 2024; 17: e202300126.
264. Wang C, Cao Z, Jin X, Lin W, Zheng Y, Zeng B, et al. Robust quantitative single-exposure laser speckle imaging with true flow speckle contrast in the temporal and spatial domains. Biomed Opt Express. 2019; 10: 4097–114.
265. Liu B, Postnov D, Boas DA, Cheng X. Dynamic light scattering and laser speckle contrast imaging of the brain: Theory of the spatial and temporal statistics of speckle pattern evolution. Biomed Opt Express. 2024; 15: 579–93.
266. Postnov DD, Tang J, Erdener SE, Kılıç K, Boas DA. Dynamic light scattering imaging. Sci Adv. 2020; 6: eabc4628.
267. Yi C, Jung J, Im J, Lee KC, Chung E, Lee SA. Single-shot temporal speckle correlation imaging using rolling shutter image sensors. Optica. 2022; 9: 1227–37.
268. Fang Q, Tomar A, Dunn AK. Wide-field intensity fluctuation imaging. Biomed Opt Express. 2024; 15: 1004–20.
269. Li DY, Xia Q, Yu TT, Zhu JT, Zhu D. Transmissive-detected laser speckle contrast imaging for blood flow monitoring in thick tissue: From Monte Carlo simulation to experimental demonstration. Light Sci Appl. 2021; 10: 241.
270. Li R, Ma M, Wang C, Hong J, Zhang Z, Lu J, et al. Dual-exposure temporal laser speckle imaging for simultaneously accessing microvascular blood perfusion and angiography. Opt Express. 2024; 32: 6887–902.
271. Hong J, Zhu W, He K, Chen X, Lu J, Li P, et al. Ergodic speckle contrast optical coherence tomography velocimetry of rapid blood flow. Opt Lett. 2024; 49: 3600–3.
272. Cheishvili K, Rieger B, Kalkman J. Precision and bias in dynamic light scattering optical coherence tomography measurements of diffusion and flow. Biomed Opt Express. 2024; 15: 1288–310.
273. Tang J, Erdener SE, Li B, Fu B, Sakadzic S, Carp SA, et al. Shear-induced diffusion of red blood cells measured with dynamic light scattering-optical coherence tomography. J Biophotonics. 2018; 11: e201700070.
274. Bi R, Du Y, Singh G, Ho JH, Zhang S, Ebrahim Attia AB, et al. Fast pulsatile blood flow measurement in deep tissue through a multimode detection fiber. J Biomed Opt. 2020; 25: 1.
275. Kim B, Zilpelwar S, Sie EJ, Marsili F, Zimmermann B, Boas DA, et al. Measuring human cerebral blood flow and brain function with fiber-based speckle contrast optical spectroscopy system. Commun Biol. 2023; 6: 844.
276. Varma HM, Valdes CP, Kristoffersen AK, Culver JP, Durduran T. Speckle contrast optical tomography: A new method for deep tissue three-dimensional tomography of blood flow. Biomed Opt Express. 2014; 5: 1275–89.
277. Huang C, Irwin D, Lin Y, Shang Y, He L, Kong W, et al. Speckle contrast diffuse correlation tomography of complex turbid medium flow. Med Phys. 2015; 42: 4000–6.
278. Zhou W, Kholiqov O, Zhu J, Zhao M, Zimmermann LL, Martin RM, et al. Functional interferometric diffusing wave spectroscopy of the human brain. Sci Adv. 2021; 7: eabe0150.
279. Xu J, Jahromi AK, Brake J, Robinson JE, Yang C. Interferometric speckle visibility spectroscopy (ISVS) for human cerebral blood flow monitoring. APL Photonics. 2020; 5: 126102.
280. Bashkatov AN, Berezin KV, Dvoretskiy KN, Chernavina ML, Genina EA, Genin VD, et al. Measurement of tissue optical properties in the context of tissue optical clearing. J Biomed Opt. 2018; 23: 091416.
281. Yu T, Zhong X, Li D, Zhu J, Tuchin VV, Zhu D. Delivery and kinetics of immersion optical clearing agents in tissues: optical imaging from *ex vivo* to *in vivo*. Adv Drug Deliv Rev. 2024; 215: 115470.
282. Tuchin VV, Zhu D, Genina EA. Handbook of tissue optical clearing: New prospects in optical imaging. Boca Raton: CRC Press; 2022.
283. Zhu D, Tuchin V. Tissue Optical Clearing Imaging from *ex vivo* toward *in vivo*. BME Front. 2024; 5: 58.
284. Richardson DS, Guan W, Matsumoto K, Pan C, Chung K, Ertürk A, et al. Tissue clearing. Nat Rev Meth Primers. 2021; 1: 84.
285. Zhu J, Liu X, Liu Z, Deng Y, Xu J, Liu K, et al. SOLID: Minimizing tissue distortion for brain-wide profiling of diverse architectures. Nat Commun. 2024; 15: 8303.
286. Ou Z, Duh YS, Rommelfanger NJ, Keck CHC, Jiang S, Brinson K Jr, et al. Achieving optical transparency in live animals with absorbing molecules. Science. 2024; 385: eadm6869.
287. Zheng S, Li W, Pang W, Zhong T, Lai P. Optical transparency in live animals: a leap toward deep-tissue applications. Adv Photon. 2024; 6: 060504.
288. Li D, Hu Z, Zhang H, Yang Q, Zhu L, Liu Y, et al. A Through-Intact-Skull (TIS) chronic window technique for cortical structure and function observation in mice. eLight. 2022; 2: 15.
289. Zhang Y, Wang M, Zhu Q, Guo Y, Liu B, Li J, et al. Long-term mesoscale imaging of 3D intercellular dynamics across a mammalian organ. Cell. 2024; 187: 6104–22.e25.
290. Wu W, He S, Wu J, Chen C, Li X, Liu K, et al. Long-term *in vivo* imaging of mouse spinal cord through an optically cleared intervertebral window. Nat Commun. 2022; 13: 1959.
291. Kazachkina NI, Zherdeva VV, Meerovich IG, Saydasheva AN, Solovyev ID, Tuchina DK, et al. MR and fluorescence imaging of gadobutrol-induced optical clearing of red fluorescent protein signal in an *in vivo* cancer model. NMR Biomed. 2022; 35: e4708.
292. Yu T, Zhu D. Strongly absorbing molecules make tissue transparent: a new insight for understanding tissue optical clearing. Light Sci Appl. 2025; 14: 10.
293. Carneiro I, Carvalho S, Henrique R, Oliveira L, Tuchin V. Moving tissue spectral window to the deep-ultraviolet via optical clearing. J Biophotonics. 2019; 12: e201900181.
294. Park J, Wang J, Guan W, Gjesteby LA, Pollack D, Kamentsky L, et al. Integrated platform for multiscale molecular imaging and phenotyping of the human brain. Science. 2024; 384: eadh9979.
295. Zhong X, Gao C, Li H, He Y, Fei P, Chen Z, et al. MACS-W: A modified optical clearing agent for imaging 3D cell cultures. J Innov Opt Health Sci. 2024; 17: 2350018.
296. Tuchin VV, Genina EA, Tuchina ES, Svetlakova AV, Svenskaya YI. Optical

clearing of tissues: Issues of antimicrobial phototherapy and drug delivery. Adv Drug Deliv Rev. 2022; 180: 114037.
297. Liu JTC, Glaser AK, Bera K, True LD, Reder NP, Eliceiri KW, et al. Harnessing non-destructive 3D pathology. Nat Biomed Eng. 2021; 5: 203–18.
298. Carr JA, Franke D, Caram JR, Perkinson CF, Saif M, Askoxylakis V, et al. Shortwave infrared fluorescence imaging with the clinically approved near-infrared dye indocyanine green. Proc Natl Acad Sci USA. 2018; 115: 4465–70.
299. Zhang Z, Fang C, Zhang Y, Su S, Li B, Liu G, et al. NIR-II nano fluorescence image guided hepatic carcinoma resection on cirrhotic patient. Photodiagn Photodyn Ther. 2022; 40: 103098.
300. Mi J, Liu G, Lu L, Yang F, Zhao H, Li Y, et al. Case report: The second near-infrared window indocyanine green angiography in giant mediastinal tumor resection. Front Surg. 2022; 9: 852372.
301. Wu Y, Suo Y, Wang Z, Yu Y, Duan S, Liu H, et al. First clinical applications for the NIR-II imaging with ICG in microsurgery. Front Bioeng Biotechnol. 2022; 10: 1042546.
302. Guo X, Luo S, Wang X, Cui Y, Li M, Zhang Z, et al. CD24-targeted NIR-II fluorescence imaging enables early detection of colorectal neoplasia. Cancer Res. 2024; 84: 4099–113.
303. Guo X, Li C, Jia X, Qu Y, Li M, Cao C, et al. NIR-II fluorescence imaging-guided colorectal cancer surgery targeting CEACAM5 by a nanobody. EBioMedicine. 2023; 89: 104476.
304. Tian Y, Shen H, Li L, Jia X, Liu J, Hu Z, et al. Enhancing surgical outcomes: Accurate identification and removal of prostate cancer with B7-H3-targeted NIR-II molecular imaging. Eur J Nucl Med Mol Imag. 2024; 51: 2569–82.
305. Zeng F, Li C, Wang H, Wang Y, Ren T, He F, et al. Intraoperative resection guidance and rapid pathological diagnosis of osteosarcoma using B7H3 targeted probe under NIR-II fluorescence imaging. Adv Sci. 2024; 11: 2310167.
306. Shen B, Zhang Z, Shi X, Cao C, Zhang Z, Hu Z, et al. Real-time intraoperative glioma diagnosis using fluorescence imaging and deep convolutional neural networks. Eur J Nucl Med Mol Imaging. 2021; 48: 3482–92.
307. Xiao A, Shen B, Shi X, Zhang Z, Zhang Z, Tian J, et al. Intraoperative glioma grading using neural architecture search and multi-modal imaging. IEEE Trans Med Imaging. 2022; 41: 2570–81.
308. Xiao A, Han K, Shi X, Tian J, Hu Z. Data augmentation with multi-armed bandit on image deformations improves fluorescence glioma boundary recognition. In: Medical image computing and computer assisted intervention–MICCAI 2024. Cham: Springer Nature Switzerland. 2024; 130–40.
309. Zhao H, Li C, Shi X, Zhang J, Jia X, Hu Z, et al. Near-infrared II fluorescence-guided glioblastoma surgery targeting monocarboxylate transporter 4 combined with photothermal therapy. EBioMedicine. 2024; 106: 105243.
310. Li C, Mi J, Wang Y, Zhang Z, Guo X, Zhou J, et al. New and effective EGFR-targeted fluorescence imaging technology for intraoperative rapid determination of lung cancer in freshly isolated tissue. Eur J Nucl Med Mol Imag. 2023; 50: 494–507.
311. Keizers B, Nijboer TS, van der Fels CAM, van den Heuvel MC, van Dam GM, Kruijff S, et al. Systematic comparison of fluorescence imaging in the near-infrared and shortwave-infrared spectral range using clinical tumor samples containing cetuximab-IRDye800CW. J Biomed Opt. 2025; 30: S13708.
312. Wood CA, Han S, Kim CS, Wen Y, Sampaio DRT, Harris JT, et al. Clinically translatable quantitative molecular photoacoustic imaging with liposome-encapsulated ICG J-aggregates. Nat Commun. 2021; 12: 5410.
313. Kim C, Erpelding TN, Jankovic L, Pashley MD, Wang LV. Deeply penetrating *in vivo* photoacoustic imaging using a clinical ultrasound array system. Biomed Opt Express. 2010; 1: 278–84.
314. Chen Q, Liu X, Chen J, Zeng J, Cheng Z, Liu Z. A self-assembled albumin-based nanoprobe for *in vivo* ratiometric photoacoustic pH imaging. Adv Mater. 2015; 27: 6820–7.
315. Ma J, Chen D, Li Y, Chen Y, Liu Q, Zhou X, et al. Zinc phthalocyanine-soybean phospholipid complex based drug carrier for switchable photoacoustic/fluorescence image, multiphase photothermal/photodynamic treatment and synergetic therapy. J Control Release. 2018; 284: 1–14.
316. Tsang VTC, Li X, Wong TTW. A review of endogenous and exogenous contrast agents used in photoacoustic tomography with different sensing configurations. Sensors. 2020; 20: 5595.
317. Ntziachristos V. Going deeper than microscopy: The optical imaging frontier in biology. Nat Methods. 2010; 7: 603–14.
318. Yoon S, Kim M, Jang M, Choi Y, Choi W, Kang S, et al. Deep optical imaging within complex scattering media. Nat Rev Phys. 2020; 2: 141–58.
319. Wetzstein G, Ozcan A, Gigan S, Fan S, Englund D, Soljačić M, et al. Inference in artificial intelligence with deep optics and photonics. Nature. 2020; 588: 39–47.
320. Zuo C, Qian J, Feng S, Yin W, Li Y, Fan P, et al. Deep learning in optical metrology: A review. Light Sci Appl. 2022; 11: 1–54.
321. Aggarwal A, Mittal M, Battineni G. Generative adversarial network: An overview of theory and applications. Int J Inf Manag Data Insights. 2021; 1: 100004.
322. Lee C, Song G, Kim H, Ye JC, Jang M. Deep learning based on parameterized physical forward model for adaptive holographic imaging with unpaired data. Nat Mach Intell. 2023; 5: 35–45.
323. Shi L, Li B, Kim C, Kellnhofer P, Matusik W. Towards real-time photorealistic 3D holography with deep neural networks. Nature. 2021; 591: 234–9.
324. Abdar M, Pourpanah F, Hussain S, Rezazadegan D, Liu L, Ghavamzadeh M, et al. A review of uncertainty quantification in deep learning: Techniques, applications and challenges. Inf Fusion. 2021; 76: 243–97.
325. Sapoval N, Aghazadeh A, Nute MG, Antunes DA, Balaji A, Baraniuk R, et al. Current progress and open challenges for applying deep learning across the biosciences. Nat Commun. 2022; 13: 1728.
326. Wei X, Feng T, Huang Q, Chen Q, Zuo C, Ma H. Deep learning-powered biomedical photoacoustic imaging. Neurocomputing. 2024; 573: 127207.
327. Zhu J, Freitas HR, Maezawa I, Jin LW, Srinivasan VJ. 1700 nm optical coherence microscopy enables minimally invasive, label-free, *in vivo* optical biopsy deep in the mouse brain. Light Sci Appl. 2021; 10: 145.
328. Wan B, Ganier C, Du-Harpur X, Harun N, Watt FM, Patalay R, et al. Applications and future directions for optical coherence tomography in dermatology. Br J Dermatol. 2021; 184: 1014–22.
329. Wang T, Ouzounov DG, Wu C, Horton NG, Zhang B, Wu CH, et al. Three-photon imaging of mouse brain structure and function through the intact skull. Nat Methods. 2018; 15: 789–92.
330. Li R, Yang D, Fang F, Hong KS, Reiss AL, Zhang Y. Concurrent fNIRS and EEG for brain function investigation: A systematic, methodology-focused review. Sensors. 2022; 22: 5865.
331. Horton NG, Wang K, Kobat D, Clark CG, Wise FW, Schaffer CB, et al. *In vivo* three-photon microscopy of subcortical structures within an intact mouse brain. Nature Photon. 2013; 7: 205–9.
332. Koch M, Symvoulidis P, Ntziachristos V. Tackling standardization in fluorescence molecular imaging. Nature Photon. 2018; 12: 505–15.
333. Feng Z, Tang T, Wu T, Yu X, Zhang Y, Wang M, et al. Perfecting and extending the near-infrared imaging window. Light Sci Appl. 2021; 10: 197.
334. Schmidt EL, Ou Z, Ximendes E, Cui H, Keck CHC, Jaque D, et al. Near-infrared II fluorescence imaging. Nat Rev Meth Primers. 2024; 4: 23.
335. Moon JA, Mahon R, Duncan MD, Reintjes J. Resolution limits for imaging through turbid media with diffuse light. Opt Lett. 1993; 18: 1591–3.
336. Humbert J, Will O, Peñate-Medina T, Peñate-Medina O, Jansen O, Both M, et al. Comparison of photoacoustic and fluorescence tomography for the *in vivo* imaging of ICG-labelled liposomes in the medullary cavity in mice. Photoacoustics. 2020; 20: 100210.
337. Miller DT, Kurokawa K. Cellular-scale imaging of transparent retinal structures and processes using adaptive optics optical coherence tomography. Annu Rev Vis Sci. 2020; 6: 115–48.
338. Liu Y, Crowell JA, Kurokawa K, Bernucci MT, Ji Q, Lassoued A, et al. Ultrafast adaptive optics for imaging the living human eye. Nat Commun. 2024; 15: 10409.
339. Commère J, Glanc M, Bourdieu L, Galicher R, Gendron É, Rousset G. Experimental characterization of an isoplanatic patch in mouse cortex using adaptive optics. Biomed Opt Express. 2024; 15: 5645–59.
340. Qureshi MM, Brake J, Jeon HJ, Ruan H, Liu Y, Safi AM, et al. *In vivo* study of optical speckle decorrelation time across depths in the mouse brain. Biomed Opt Express. 2017; 8: 4855–64.
341. Forouhesh Tehrani K, Koukourakis N, Czarske J, Mortensen LJ. *In situ* measurement of the isoplanatic patch for imaging through intact bone. J Biophotonics. 2021; 14: e202000160.
342. Ma C, Xu X, Wang LV. Analog time-reversed ultrasonically encoded light focusing inside scattering media with a 33,000× optical power gain. Sci Rep. 2015; 5: 8896.
343. Cheng Z, Wang LV. Focusing light into scattering media with ultrasound-induced field perturbation. Light Sci Appl. 2021; 10: 159.
344. Horstmeyer R, Ruan H, Yang C. Guidestar-assisted wavefront-shaping methods for focusing light into biological tissue. Nature Photon. 2015; 9: 563–71.
345. Xu X, Liu H, Wang LV. Time-reversed ultrasonically encoded optical focusing into scattering media. Nature Photon. 2011; 5: 154–7.
346. Blochet B, Akemann W, Gigan S, Bourdieu L. Fast wavefront shaping for two-photon brain imaging with multipatch correction. Proc Natl Acad Sci USA. 2023; 120: e2305593120.
347. Costantini I, Cicchi R, Silvestri L, Vanzi F, Pavone FS. *In-vivo* and *ex-vivo* optical clearing methods for biological tissues: review. Biomed Opt Express. 2019; 10: 5251–67.
348. Wu Q, Huang B, Peng X, He S, Zhan Q. Non-bleaching fluorescence emission difference microscopy using single 808-nm laser excited red upconversion emission. Opt Express. 2017; 25: 30885–94.
349. Wang K, Wang Q, Luo Q, Yang X. Fluorescence molecular tomography in the second near-infrared window. Opt Express. 2015; 23: 12669–79.
350. Park S, Lee C, Kim J, Kim C. Acoustic resolution photoacoustic microscopy. Biomed Eng Lett. 2014; 4: 213–22.